

**CHEMICAL STRUCTURE - NONLINEAR OPTICAL PROPERTY  
RELATIONSHIPS  
FOR A SERIES OF TWO-PHOTON ABSORBING  
FLUORENE MOLECULES**

by

JOEL MCCAIAH HALES  
B.S. Georgia Institute of Technology, 1998  
M.S. University of Central Florida, 2000

A dissertation submitted in partial fulfillment of the requirements  
for the degree of Doctor of Philosophy  
in the School of Optics  
at the University of Central Florida  
Orlando, Florida

Spring Term  
2004

Major Professors: Eric W. Van Stryland and David J. Hagan

© 2004 Joel M. Hales

## ABSTRACT

This dissertation reports on the investigation of two-photon absorption (2PA) in a series of fluorenyl molecules. Several current and emerging technologies exploit this optical nonlinearity including two-photon fluorescence imaging, three-dimensional microfabrication, site-specific photodynamic cancer therapy and biological caging studies. The two key features of this nonlinearity which make it an ideal candidate for the above applications are its quadratic dependence on the incident irradiance and the improved penetration into absorbing media that it affords. As a consequence of the burgeoning field which exploits 2PA, it is a goal to find materials that exhibit strong two-photon absorbing capabilities. Organic materials are promising candidates for 2PA applications because their material properties can be tailored through molecular engineering thereby facilitating optimization of their nonlinear optical properties. Fluorene derivatives are particularly interesting since they possess high photochemical stability for organic molecules and are generally strongly fluorescent.

By systematically altering the structural properties in a series of fluorenyl molecules, we have determined how these changes affect their two-photon absorbing capabilities. This was accomplished through characterization of both the strength and location of their 2PA spectra. In order to ensure the validity of these results, three separate nonlinear characterization techniques were employed: two-photon fluorescence spectroscopy, white-light continuum pump-probe spectroscopy, and the Z-scan technique. In addition, full linear spectroscopic characterization

was performed on these molecules along with supplementary quantum chemical calculations to obtain certain molecular properties that might impact the nonlinearity.

Different designs in chemical architecture allowed investigation of the effects of symmetry, solvism, donor-acceptor strengths, conjugation length, and multi-branched geometries on the two-photon absorbing properties of these molecules. In addition, the means to enhance 2PA via intermediate state resonances was investigated. To provide plausible explanations for the experimentally observed trends, a conceptually simple three level model was employed. The subsequent correlations found between chemical structure and the linear and nonlinear optical properties of these molecules provided definitive conclusions on how to properly optimize their two-photon absorbing capabilities. The resulting large nonlinearities found in these molecules have already shown promise in a variety of the aforementioned applications.

This dissertation is dedicated to my parents, my family, and my fiancée Katherine, who have given me unending love and support throughout the years.

## ACKNOWLEDGEMENTS

I would truly like to thank my advisors, Dr. David J. Hagan and Dr. Eric Van Stryland, for providing a great environment in which to complete my graduate research. Despite their incredibly hectic schedules, they both made every effort possible to provide me with any guidance I may have needed.

The whole of the work presented in this dissertation was the result of a truly collaborative effort. I want to sincerely thank Mihaela Balu for her experimental work involving Z-scan measurements, the members of Dr. Jean-Luc Bredas' group, Tommy Kwon, Peter Pacher, and Egbert Zojer for their contributions in the quantum-chemical analysis of the molecules, and finally, the members of Dr. Kevin Belfield's group, Alma Morales, Sheng Yao, Mike Bondar, and Katherine Schafer for the synthesis and linear characterization efforts involving the fluorene derivatives. Without their support, the comprehensive work detailed here would have never come to fruition.

I also wish to express my appreciation towards the graduate students I have had the pleasure of working with throughout my years here. In particular, Raluca Negres became a great friend as she suffered through my incessant curiosity and taught me much of what I now know about laboratory research. Also, Richard Lepkowicz has been a wonderful friend from the days we attended undergraduate school together until our final days at CREOL.

Finally, I want to thank all of my friends and acquaintances I've made here while in graduate school. This is particularly true for all the members of the Delta Force, both original

and honorary. Mike, Will, Tolga, Steve, Corey, Vinay and Javier (JG), you all made this one of the best times of my life. Thank you to everyone.

## TABLE OF CONTENTS

LIST OF FIGURES .....	xi
LIST OF TABLES .....	xv
LIST OF NOMENCLATURE .....	xvii
CHAPTER 1: INTRODUCTION .....	1
1.1 Background and Motivation .....	1
1.2 Dissertation Statement .....	7
1.3 Dissertation Outline .....	8
CHAPTER 2: TWO-PHOTON ABSORPTION THEORY .....	10
2.1 Microscopic Polarizabilities.....	11
2.2 Perturbation Theory – Sum-Over-States Approach.....	17
2.3 Simplified Essential States Model .....	21
2.4 Governing Elements of Two-Photon Absorption .....	24
2.4.1 Transition and State Dipole Moments .....	25
2.4.2 Detuning Energy .....	29
2.4.3 Transition Dipole Moment Orientation .....	32
CHAPTER 3: METHODOLOGY .....	33
3.1 Linear Spectroscopic Techniques .....	34
3.2 Two-Photon Fluorescence Spectroscopy .....	35
3.2.1 Experimental Apparatus.....	37



3.2.2 Inner Filter Effect.....	40
3.2.3 Determination of the Two-Photon Absorption Cross-Section.....	42
3.3 White-Light Continuum Pump-Probe Spectroscopy .....	45
3.3.1 Experimental Technique .....	46
3.3.2 Experimental Apparatus.....	49
3.3.3 Cross-Phase Modulation .....	59
3.4 Z-Scan.....	64
3.5 Quantum-Chemical Methodology .....	66
CHAPTER 4: FLUORENE MOLECULES .....	69
4.1 Fluorene Chromophore .....	69
4.2 Fluorene Derivatives.....	72
4.3 Linear Spectroscopy.....	77
CHAPTER 5: STRUCTURE-PROPERTY RELATIONSHIPS .....	85
5.1 Symmetry.....	88
5.2 Dipolar Molecules.....	95
5.2.1 Acceptor Strength .....	98
5.2.2 Solvism .....	104
5.3 Symmetric Molecules .....	111
5.3.1 Donor Versus Acceptor End-Groups.....	112
5.3.2 Acceptor Strength .....	120
5.4 Conjugation Length .....	122
5.4.1 Styryl Extension.....	126
5.4.2 Vinyl-Fluorene Extension.....	135

5.4.3 Amino-Fluorene Extension.....	139
5.5 Multi-branched Molecules.....	143
5.6 Resonance Enhancement .....	147
CHAPTER 6: INTERMEDIATE STATE RESONANCE ENHANCEMENT.....	154
6.1 Two-Photon Absorption Spectra.....	156
6.1.1 Experimentally Determined Spectra .....	156
6.1.2 Theoretically Determined Spectra .....	162
6.2 Essential States Model for Nondegenerate Two-Photon Absorption .....	163
CHAPTER 7: CONCLUSION .....	169
7.1 Synopsis .....	169
7.2 Future Work .....	172
APPENDIX A: DERIVATION OF THE NONDEGENERATE TWO-PHOTON ABSORPTION CROSS-SECTION.....	174
APPENDIX B: DERIVATION OF THE INTENSITY OF THE COLLECTED TWO-PHOTON FLUORESCENCE SIGNAL .....	178
APPENDIX C: CHEMICAL NOMENCLATURE FOR FLUORENE DERIVATIVES .....	181
LIST OF REFERENCES.....	184

## LIST OF FIGURES

Figure 1.1: (a) Schematic illustration of the high degree of spatial selectivity afforded by 2PA.	
(b) Photograph detailing the greater spatial resolution of two-photon versus one-photon excitation (taken from [6]).	4
Figure 1.2: Spectral transmission window in highly absorbing, scattering media detailing the benefit of using infrared radiation for improved penetration depth (taken from [7]).	5
Figure 1.3: 2PA process followed by subsequent photophysical process (S0, S1, S2 singlet states, T1 triplet State).	6
Figure 2.1: Simulated atomic transition densities for a polyene chain.	28
Figure 2.2: Resonance enhancement of 2PA.	31
Figure 3.1: Schematic for the two-photon induced fluorescence experiment.	38
Figure 3.2: Illustration of the inner filter effect for a solution of Fluorescein in water (pH=11).	41
Figure 3.3: Two-photon absorption spectra of the reference standards used in the 2PF technique.	45
Figure 3.4: Schematic for the white-light continuum pump-probe spectroscopy experiment.	51
Figure 3.5: Off-axis geometry for achromatic focusing of the WLC onto the sample plane.	57
Figure 3.6: Typical pump-probe time delay scans acquired using our WLC spectroscopy set-up.	62

Figure 3.7: Pump-probe time delay scans exhibiting XPM signals acquired for various sample configurations. ....	64
Figure 3.8: Typical Z-scan curve acquired from a two-photon absorbing medium. ....	65
Figure 4.1: The base fluorene chromophore. ....	70
Figure 4.2: General architecture for the fluorene derivatives. ....	72
Figure 4.3: Chemical structures of fluorene derivatives. ....	75
Figure 4.4: Absorption (a) and steady-state fluorescence (b) spectra for molecules <b>1-4</b> in hexane. ....	78
Figure 4.5: Absorption (a) and steady-state fluorescence (b) spectra for molecules <b>5-8</b> in hexane. ....	78
Figure 4.6: Absorption (a) and steady-state fluorescence (b) spectra for molecules <b>9-12</b> . ....	79
Figure 4.7: Absorption (a) and steady-state fluorescence (b) spectra for molecules <b>13-15</b> in hexane. ....	79
Figure 4.8: Absorption (a) and steady-state fluorescence (b) spectra for molecules <b>16</b> and <b>17</b> in hexane. ....	79
Figure 4.9: Absorption (a) and steady-state fluorescence (b) spectra for molecules <b>18</b> and <b>19</b> in cyclohexane.....	80
Figure 4.10: Linear absorption and steady-state excitation anisotropy spectra for molecules <b>3</b> (a), <b>5</b> (b), <b>6</b> (c), <b>10</b> (d), <b>12</b> (e), and <b>16</b> (f) in silicon oil.....	84
Figure 5.1: 2PA spectra for molecule <b>3</b> in hexane as acquired from the three different nonlinear characterization methods used in this study.....	88
Figure 5.2: 2PA and 1PA spectra for molecules <b>6</b> (a), <b>3</b> (b), and <b>5</b> (c) in hexane. ....	92

Figure 5.3: Evolution of the second hyperpolarizability $\gamma$ versus BOA for a donor-acceptor polyene. ....	97
Figure 5.4: Experimentally determined 2PA spectra for dipolar molecules <b>1-4</b> in hexane.....	99
Figure 5.5: Quantum-chemically determined 2PA spectra for dipolar molecules <b>1-4</b> according to the methodology detailed in Section 3.5.....	102
Figure 5.6: Absorption (a) and steady-state fluorescence (b) spectra for molecule <b>3</b> in various solvents. ....	106
Figure 5.7: Experimentally determined 2PA spectra for dipolar molecule <b>3</b> in various solvents. ....	108
Figure 5.8: Experimentally determined 2PA spectra for dipolar molecule <b>9</b> in hexane and methylene chloride.....	111
Figure 5.9: Experimentally determined 2PA spectra for symmetric molecules <b>5</b> and <b>6</b> in hexane. ....	114
Figure 5.10: Quantum-chemically determined 2PA spectra for symmetric molecules <b>5</b> and <b>6</b> according to the methodology detailed in Section 3.5.....	115
Figure 5.11: Quantum-chemically calculated atomic transition densities for upper level transitions in molecules <b>5</b> and <b>6</b> .....	119
Figure 5.12: Experimentally determined 2PA spectra for symmetric molecules <b>6</b> and <b>8</b> in hexane. ....	121
Figure 5.13: Dependence of chain length on the value of $\gamma$ for a series of (a) saturated molecules – alkanes and cycloalkanes and (b) unsaturated molecules – polyenes (taken from [97]).	123
Figure 5.14: Experimentally determined 2PA spectra for molecules <b>3</b> , <b>9</b> and <b>10</b> in hexane.....	127

Figure 5.15: Experimentally determined 2PA spectra for (a) molecules <b>5</b> and <b>11</b> in hexane and (b) molecule <b>6</b> in hexane and <b>12</b> in methylene chloride. ....	130
Figure 5.16: Quantum-chemically determined 2PA spectra for molecules <b>5</b> , <b>6</b> , <b>11</b> and <b>12</b> according to the methodology detailed in Section 3.5.....	132
Figure 5.17: Experimentally determined 2PA spectra for molecules <b>13</b> , <b>14</b> and <b>15</b> in hexane..	136
Figure 5.18: Experimentally determined 2PA spectra for molecules <b>5</b> , <b>16</b> and <b>17</b> in hexane. ..	141
Figure 5.19: Experimentally determined 2PA spectra for molecules <b>11</b> , <b>18</b> and <b>19</b> in cyclohexane while <b>5</b> is in hexane. ....	144
Figure 5.20: Linear absorption spectra for molecules <b>3</b> and <b>20</b> . ....	149
Figure 5.21: Experimentally determined 2PA spectra for molecule <b>3</b> in hexane and <b>20</b> in THF. . .....	150
Figure 6.1: Schematic representation of experiments performed for 2PA into the first excited state of molecule <b>3</b> . ....	157
Figure 6.2: Schematic representation of experiments performed for 2PA into the first excited state of molecule <b>5</b> . ....	157
Figure 6.3: D-2PA and ND-2PA spectra of molecule <b>3</b> in hexane. ....	160
Figure 6.4: D-2PA and ND-2PA spectra of molecule <b>5</b> in hexane. ....	160

## LIST OF TABLES

Table 3.1: Beam sizes in the sample plane for various wavelengths of the WLC probe beam using the on-axis geometry. ....	55
Table 3.2: Beam sizes of the WLC probe beam for the off-axis geometry. ....	59
Table 4.1: Linear optical properties for the fluorene derivatives in hexane. ....	82
Table 5.1: Select quantum-chemically calculated transition energies and dipole moments for molecule <b>5</b> . ....	94
Table 5.2: Location and magnitude of the peaks of the 2PA spectra for molecules <b>1-4</b> as determined experimentally (Figure 5.4) and quantum-chemically (Figure 5.5). ....	100
Table 5.3: Select quantum-chemically calculated dipole moments (in Debye) for molecules <b>1-4</b> . These terms are used in the calculations for $\delta_{ESM}^{\max}$ which are given in Table 5.2. ....	103
Table 5.4: The dielectric constant $\epsilon$ , refractive index $n$ , and polarity $\Delta f$ of the solvents used in the solvisism investigation. ....	105
Table 5.5: Linear optical properties for the molecule <b>3</b> in various solvents. ....	107
Table 5.6: Location and magnitude of the peaks of the 2PA spectra for molecules <b>5</b> and <b>6</b> as determined experimentally (Figure 5.9) and quantum-chemically (Figure 5.10). ....	116
Table 5.7: Select quantum-chemically calculated transition energies and dipole moments for molecules <b>5</b> and <b>6</b> . ....	117
Table 5.8: Location and magnitude of the peaks of the 2PA spectra into the first two excited states for molecules <b>3</b> , <b>9</b> and <b>10</b> as determined experimentally (Figure 5.14). ....	128

Table 5.9: Location and magnitude of the peaks of the 2PA spectra for molecules <b>5</b> , <b>6</b> , <b>11</b> and <b>12</b> as determined experimentally (Figure 5.15) and quantum-chemically (Figure 5.16). .....	131
Table 5.10: Select quantum-chemically calculated transition energies and dipole moments for molecules <b>11</b> and <b>12</b> . .....	135
Table 5.11: Location and magnitude of the peaks of the 2PA spectra into the $S_1$ state for molecules <b>13</b> , <b>14</b> and <b>15</b> as determined experimentally (Figure 5.17). .....	137
Table 5.12: Location and magnitude of the peaks of the 2PA spectra into the $S_1$ state for molecules <b>16</b> and <b>17</b> as determined experimentally (Figure 5.18). .....	143
Table 5.13: Location and magnitude of the peaks of the 2PA spectra into the $S_2$ and $S_1$ states for molecules <b>11</b> , <b>18</b> and <b>19</b> as determined experimentally (Figure 5.19). .....	146
Table 5.14: Location and magnitude of the peaks of the 2PA spectra into the first two excited states for molecules <b>3</b> and <b>20</b> as determined experimentally (Figure 5.21). .....	151
Table 5.15: The appropriate terms for Equation 5.4 for molecules <b>3</b> and <b>20</b> as determined from their linear absorption spectra in Figure 5.20. ....	153
Table 6.1: D-2PA and ND-2PA spectral data for molecule <b>3</b> . ....	158
Table 6.2: D-2PA and ND-2PA spectral data for molecule <b>5</b> . ....	159
Table 6.3: Select quantum-chemically calculated transition energies (in eV) and dipole moments (in debye) for molecules <b>3</b> and <b>5</b> . ....	166



## LIST OF NOMENCLATURE

<u>Acronym/Unit</u>	<u>Description</u>
2PA	Two-Photon Absorption
2PF	Two-Photon Fluorescence
BLA	Bond-Length Alternation
BLO	Bond-Order Alternation
CaF	Calcium Fluoride
cm	Centimeter ( $10^{-2}$ m)
D-2PA	Degenerate Two-Photon Absorption
ESA	Excited-State Absorption
eV	Electron Volt unit of energy
fs	Femtosecond ( $10^{-15}$ s)
GM	Goppert-Mayer unit for the 2PA cross-section ( $1 \times 10^{-50}$ cm <sup>4</sup> sec photon <sup>-1</sup> molecule <sup>-1</sup> )
GVD	Group-Velocity Dispersion
GVM	Group-Velocity Mismatch
GW	Gigawatt ( $10^9$ W)
IFE	Inner-Filter Effect
ISC	Intersystem Crossing
kHz	Kilohertz ( $10^3$ Hz)

$\mu\text{J}$	Microjoule ( $10^{-6}$ J)
$\mu\text{m}$	Micrometer ( $10^{-6}$ m)
M	Molarity unit of concentration (Moles/Liter)
mm	Millimeter ( $10^{-3}$ m)
MW	Megawatt ( $10^6$ W)
ND-2PA	Nondegenerate Two-Photon Absorption
nJ	Nanojoule ( $10^{-9}$ J)
NLO	Nonlinear Optical
nm	Nanometer ( $10^{-9}$ m)
ns	Nanosecond ( $10^{-15}$ s)
OD	Optical Density
OKE	Optical Kerr Effect
OPA	Optical Parametric Amplifier
ps	Picosecond ( $10^{-15}$ s)
SOS	Sum-Over-States
SRS	Stimulated Raman Scattering
WLC	White Light Continuum
XPM	Cross-Phase Modulation
ZDO	Zero Differential Overlap

## CHAPTER 1: INTRODUCTION

This Chapter introduces the phenomenon known as two-photon absorption, the main nonlinearity studied in this dissertation, and explains the possible motivations for investigating this nonlinear behavior. Section 1.1 begins with an historical account of the theoretical and experimental underpinnings of this field followed by a detailed description of the unique and advantageous features associated with this process. A brief survey of the emerging applications which employ two-photon absorption is then given. Conjugated organics molecules are offered as promising choices for these applications and the possibilities of optimizing their nonlinear properties are put forth. Section 1.2 gives the dissertation statement and the concluding Section provides an outline for this work.

### 1.1 Background and Motivation

In the seminal paper written by Maria Göppert-Mayer in 1931 [1], a study concerned with the working together of two light quanta in one elementary action, the author firmly establishes the theoretical framework for two-photon absorption (2PA). This process involves the near simultaneous absorption of two photons, not necessarily at the same frequency, in a real transition within a medium. The sum of the photon energies involved is equivalent to the energy difference between the initial and final states of the transition. The following intuitive argument can be made to rationalize this phenomenon. Although neither photon has the requisite energy to

complete the transition on its own, the energy mismatch between an input photon and the nearest one-photon allowed state provides a finite time (permitted by the Uncertainty Principle) for the second photon to arrive and complete the absorption sequence to the final state [2]. The brief duration of this action ( $\sim 10^{-15}$  seconds for 2PA in the visible) elucidates the reason 2PA is classified as a “short-lived” or instantaneous nonlinear process. Furthermore, given the fleeting instant of time the second photon is afforded to complete the event, it stands to reason that a large photon flux would be necessary to produce any appreciable probability of transition. In fact, experimental observation of 2PA would await the invention of the laser and its considerable radiation flux for some thirty years following the initial theoretical work in the field. Experimental observation of this process was confirmed by Kaiser and Garrett in 1961 [3] when they observed degenerate (identical photon energies) two-photon absorption induced fluorescence in a calcium fluoride doped crystal (interestingly, this was the same issue of Physical Review Letters in which Franken *et al.* observed the first experimental evidence of Second Harmonic Generation [4]). Shortly thereafter, in 1963, Hopfield, Worlock, and Park monitored nondegenerate 2PA in the spectral transmittance of a flashlamp probe source through potassium iodide excited with a ruby laser [5].

With the advent and subsequent commercial availability of high peak-power, tunable laser sources, applications exploiting 2PA have become quite ubiquitous. Two features of this process, in particular, are responsible for its popularity. As mentioned above, the probability of 2PA is greatly enhanced with the use of high intensity radiation. Therefore, given that one-photon absorption depends linearly on the excitation irradiance  $I$ , it is not surprising that the rate of 2PA is quadratically dependent upon  $I$ . This superlinear dependence guarantees that the process will benefit from high spatial selectivity when employing a focused laser beam. This is

illustrated schematically in Figure 1.1a where an intense laser beam is focused into a two-photon absorbing medium. As a consequence of the quadratic dependence of this process on the incident irradiance, only in the focal volume (shown in green) does 2PA occur. In addition to the transverse confinement of the process (x and y directions), the affected volume is confined axially as well. This is due to the fact that the irradiance in the vicinity of the focus falls off as  $I \propto z^{-2}$  (where  $z$  is the axial propagation distance) which implies that 2PA decreases as  $z^{-4}$ . In this manner, three-dimensional high spatial resolution is achieved. This can be noted practically in Figure 1.1b where a solution of fluorescent chromophores is excited by both one (lower beam path) and two-photon absorption (upper beam path). In the case of two-photon excitation, the subsequent fluorescence is localized in the focal volume whereas the one-photon induced fluorescence extends all along the path of the focused beam.

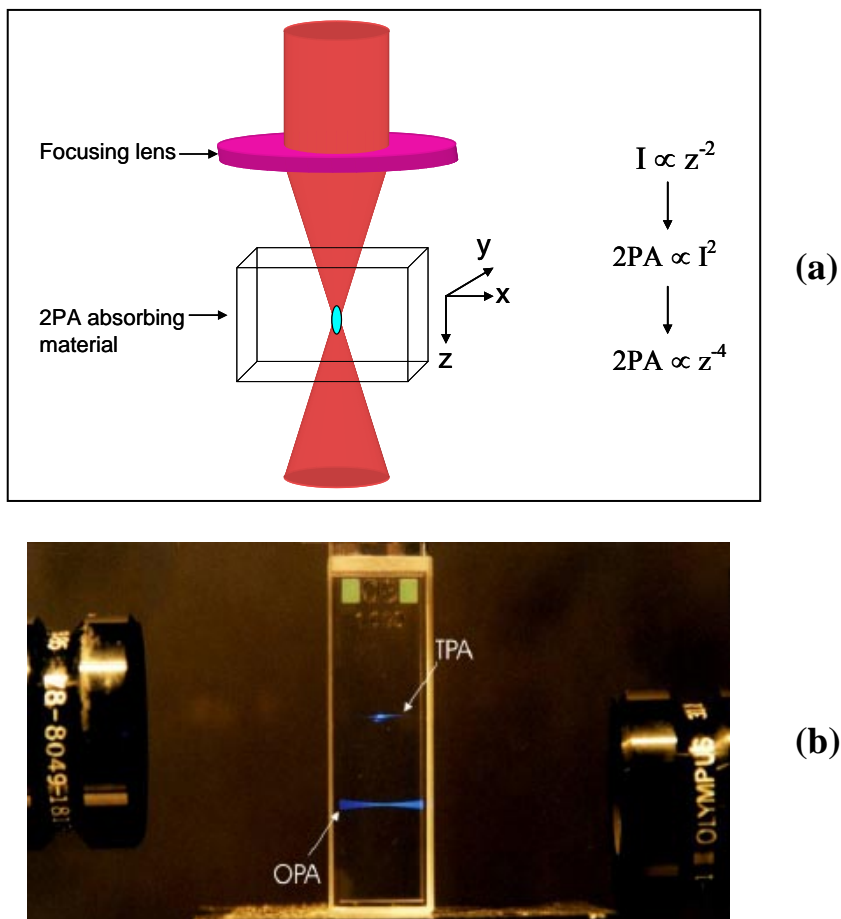


Figure 1.1: (a) Schematic illustration of the high degree of spatial selectivity afforded by 2PA. (b) Photograph detailing the greater spatial resolution of two-photon versus one-photon excitation (taken from [6]).

The second beneficial feature of 2PA states that since neither photon may access a real excited state on its own (provided the photon energies lie below the linear absorption edge of the sample), no one-photon processes will occur. Therefore, the light can penetrate further into a highly absorbing medium before inducing excitation. Moreover, when considering radiation in the visible and near infrared, longer wavelength excitation guarantees diminished light scattering. Each of these issues is crucial when two-photon induced fluorescence is used for three-dimensional imaging of biological tissues. Figure 1.2 illustrates this fact. In the red to

near-infrared region both absorption and scattering is minimal, making it an ideal spectral window for deep penetration into typical, highly absorbing, turbid biological media.

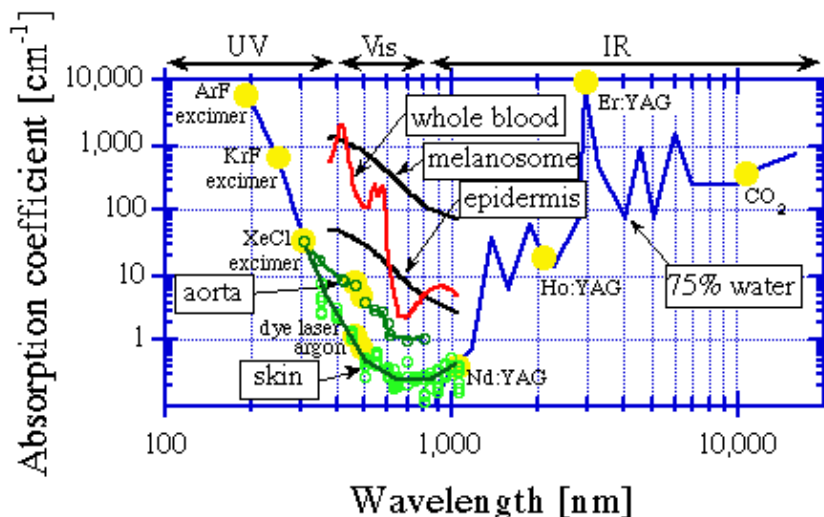


Figure 1.2: Spectral transmission window in highly absorbing, scattering media detailing the benefit of using infrared radiation for improved penetration depth (taken from [7]).

In addition to spatial localization of this process, any subsequent physical or chemical mechanism activated by 2PA will be localized as well. A number of photophysical phenomena that can be triggered by 2PA are illustrated in Figure 1.3. The energy level diagram shows promotion from the ground state  $S_0$  to a two-photon allowed state  $S_2$  which can be followed by either internal conversion to the first singlet state  $S_1$  or an intersystem crossing (ISC) to the triplet manifold  $T_1$ . Fluorescence can occur as the system radiatively relaxes from  $S_1$  to the ground state. Furthermore, excited-state absorption (i.e., photoinduced absorption from an excited state or ESA) can occur from any of the excited states  $S_1$ ,  $S_2$ , or  $T_1$ . It is precisely these phenomena which have attracted such appreciable interest in 2PA from fields as varied as

photonics, chemistry and biology. Two of the numerous technologies that utilize 2PA are three-dimensional (3-D) fluorescence imaging [8] and optical power limiting [9]. These applications employ all of the two-photon activated photophysical phenomena: imaging exploits two-photon induced fluorescence whereas optical limiting makes use of ISC and ESA. In addition to physical mechanisms, 2PA can produce highly localized photo-induced chemical reactions as well. 3-D microfabrication and optical data storage [10], as well as site-specific photodynamic cancer therapy [11] and biological caging studies [12] are among the emerging technologies which take advantage of this effect.

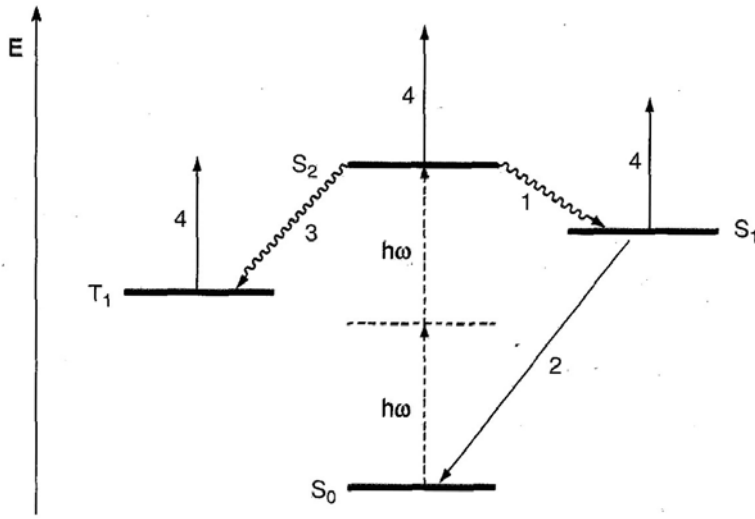


Figure 1.3: 2PA process followed by subsequent photophysical process ( $S_0$ ,  $S_1$ ,  $S_2$  singlet states,  $T_1$  triplet State). (1) Internal conversion to  $S_1$ , (2) fluorescence from  $S_1$ , (3) intersystem crossing to the triplet manifold  $T_1$ , and (4) excited-state absorption from  $S_1$ ,  $S_2$ , or  $T_1$  (taken from [13]).

As a consequence of the burgeoning field which exploits 2PA, it is a goal to find materials that possess enhanced nonlinearities. Although nonlinear loss is viewed as a



detrimental effect in some applications [14], designing materials which exhibit large two-photon absorptivities can reduce the tolerances on devices employing 2PA by increasing their sensitivity. This essentially allows one to reduce the intensity of the excitation source thereby ameliorating the possibility of optical damage. Organic molecules are promising candidates for efficient two-photon absorbers because their chemical structures can be tailored through molecular engineering. This allows for potential optimization of a material's optical properties.  $\pi$ -conjugated organic systems have been of particular interest ever since the pioneering work of Sauteret *et al.* [15] during the 1970's when the authors demonstrated that these molecules possess large third-order nonlinearities (2PA is an example of a third-order nonlinearity, a fact which will be discussed further in Section 2.1). The delocalization of the  $\pi$ -electrons in these systems gives rise to a strong polarizability which is known to accentuate a molecule's linear and nonlinear optical (NLO) responses.

With an understanding of the 2PA phenomenon and the factors that govern it, guidelines for specific structure-property relationships can be made to optimize an organic molecule's nonlinearity. Unfortunately, criteria for the design of efficient two-photon absorbing molecules are not well understood [16]. Nonetheless, guidelines for such structure-property relations are becoming much more viable as studies combining quantum-chemical analysis and experimental data become more prevalent.

## **1.2 Dissertation Statement**

The purpose of this dissertation is to investigate a set of  $\pi$ -conjugated fluorenyl molecules whose structural properties have been systemically altered to determine how these

changes affect their two-photon absorbing capabilities. By employing a conceptually simple model that describes the elements which control the 2PA phenomenon, one discovers that the NLO response of a system is intimately related to its linear optical properties. Therefore, full linear spectroscopic characterization is performed on these compounds to determine the strength, location and spectral contour of their absorption and emission spectra. Furthermore, quantum-chemical methods are employed to determine state dipole moments as well as transition moments between higher level excited states of these molecules. Finally, three separate nonlinear characterization methods are used to determine both the strength and location of the 2PA spectra. Structural motifs (i.e., designs in architecture), as varied as symmetry, solvism, donor-acceptor strengths, conjugation length, and multi-branched geometries are investigated. In addition, the means to enhance this nonlinearity via intermediate state resonances is investigated using nondegenerate 2PA. It is the correlation between chemical structure and the linear and NLO properties of these molecules which should provide definitive conclusions on how to properly optimize their two-photon absorbing capabilities.

### **1.3 Dissertation Outline**

This work is structured according to the following: The first Chapter introduces the concept of two-photon absorption and provides the impetus for investigating this nonlinear behavior. Chapter 2 describes this process in terms of its light-matter interaction and presents the perturbative Sum-Over-States (SOS) formulation for the third-order polarizability,  $\gamma$ . The subsequent unveiling of a conceptually simple version of this complicated expression illuminates the key elements which control 2PA. The linear and nonlinear spectroscopic techniques

involved in this study are detailed in Chapter 3 along with the quantum-chemical methodology that is employed. The following Chapter concentrates on the structures of the fluorene chromophore base and its associated organic derivatives. The linear spectroscopic data for these molecules are also presented. Chapter 5 addresses the relationships between chemical structures and the two-photon absorbing properties of these molecules for a variety of different structural motifs. Using the simplified expression for  $\gamma$  given in Chapter 2, plausible explanations for the identified trends are offered. In Chapter 6, a unique method for investigating the effect of intermediate state resonance enhancement of 2PA is covered. Finally, Chapter 7 concludes the dissertation and suggests some future directions which might be taken.

## CHAPTER 2: TWO-PHOTON ABSORPTION THEORY

The response of a material following its interaction with light can vary greatly depending on the strength of the incident optical field. For certain materials, application of intense electric fields may very well alter their intrinsic optical properties. Two-photon absorption is one such consequence of this nonlinear behavior between light and matter. When viewed at a microscopic level, certain factors controlling the efficacy of this mechanism can be identified.

Since 2PA, along with all other NLO responses, is a direct manifestation of the nonlinear polarization of a material, we begin the Chapter by giving a brief description of the concepts of linear and nonlinear polarizability. Section 2.1 also introduces another molecular parameter, the 2PA cross-section  $\delta$ , and relates it to the third-order molecular polarizability  $\gamma$ . In addition, we comment on the consequences of relating a microscopic parameter, such as  $\gamma$  or  $\delta$ , to a macroscopic quantity. The second Section discusses the quantum-mechanical approaches to calculating molecular polarizabilities. Particular attention is paid to the perturbative Sum-Over-States (SOS) approach which is used throughout this study. The SOS technique implies that the calculation involves a summation over all of the excited states of the system which, although at times can be quite accurate, is far too unwieldy for conceptual use. Therefore, approximations can be made which allow for truncation of this expression. This essential states model is the subject of Section 2.3. Finally, specific linear properties derived from the essential states terms and their influence on the efficacy of 2PA will be examined in Section 2.4. The objective of this

conceptually simplified model is to help determine the relationships between the chemical structure and the NLO response of our compounds.

## 2.1 Microscopic Polarizabilities

The concepts of microscopic polarization have been well catalogued in the literature and descriptions similar to the one following can be found in References 17 and 18.

A material can polarize when in the presence of an oscillating electric field. This can be better understood when viewing this phenomenon at the molecular level of the system. At this level, the material consists of a distribution of charged particles, namely positively charged nuclei and negatively charged electrons. In general, the electron is “elastically” coupled to the nucleus and therefore an oscillating electric field would interact with the material such that the electron distribution and the ion core would perform an oscillatory motion with respect to one another. Therefore an applied optical field  $\mathbf{E}$  will displace the electron density from the nuclear core and create an induced dipole  $\boldsymbol{\mu}$ . It is this induced polarization which accounts for an abundance of optical properties of materials.

Provided the incident optical field is small in magnitude, the displacement of the electron charge cloud will remain small as well, and will oscillate harmonically with the frequency of the incident field. In this regime, the induced dipole can be considered to be linearly proportional to the strength of the applied optical field and an expression can be written relating the two terms:

$$\boldsymbol{\mu}_i(\omega) = \alpha_{ij}(\omega)\mathbf{E}_j(\omega) \quad 2.1$$

Here,  $\boldsymbol{\mu}$  and  $\mathbf{E}$  are given as vector quantities and  $\alpha_{ij}(\omega)$  is the linear polarizability of the molecule. In addition, it should be noted that  $\alpha$  is a second rank tensor for general anisotropic

media and is a complex parameter. This term is the source for linear optical effects such as absorption (associated with the imaginary part of  $\alpha$ ), refraction, and birefringence (each related to the real part of  $\alpha$ ).

Nonetheless, many problems of interest in optics involve nonlinear interactions that occur when the electromagnetic interaction becomes too large for the medium to continue to respond linearly. This causes the electron to oscillate anharmonically in response to the applied field. Therefore, when a molecule experiences a high intensity optical field, its induced polarization responds in a manner which is nonlinear with respect to the field strength. An exact solution for the functional form of  $\mu$  is no longer valid and it is therefore quite common to express the total dipole as a Taylor series expansion in  $\mathbf{E}$  [19]:

$$\mu_i = \mu_i^0 + \left( \frac{\partial \mu_i}{\partial \mathbf{E}_j} \right) \mathbf{E}_j + \frac{1}{2} \left( \frac{\partial^2 \mu_i}{\partial \mathbf{E}_j \partial \mathbf{E}_k} \right) \mathbf{E}_j \mathbf{E}_k + \frac{1}{3!} \left( \frac{\partial^3 \mu_i}{\partial \mathbf{E}_j \partial \mathbf{E}_k \partial \mathbf{E}_l} \right) \mathbf{E}_j \mathbf{E}_k \mathbf{E}_l + \dots \quad 2.2$$

or

$$\begin{aligned} \mu_i = & \mu_i^0 + \alpha_{ij}(-\omega; \omega) \mathbf{E}_j(\omega) + \frac{1}{2} \beta_{ijk}(-\omega_3; \omega_1, \omega_2) \mathbf{E}_j(\omega_1) \mathbf{E}_k(\omega_2) + \\ & \frac{1}{6} \gamma_{ijkl}(-\omega_4; \omega_1, \omega_2, \omega_3) \mathbf{E}_j(\omega_1) \mathbf{E}_k(\omega_2) \mathbf{E}_l(\omega_3) + \dots \end{aligned} \quad 2.3$$

where the frequency dependence expressed in the second equation is implied in the first. In Equation 2.3,  $\mu_i^0$  represents the permanent dipole,  $\alpha_{ij}$  is the first-order polarizability,  $\beta_{ijk}$  the second-order polarizability (also known as the first hyperpolarizability), and  $\gamma_{ijkl}$  is the third-order polarizability (or the second hyperpolarizability).  $\beta$  and  $\gamma$  are tensors of third and fourth rank, respectively. The polarization terms which are dependent on higher powers of the field, namely  $\beta E^2$ ,  $\gamma E^3$  and higher, are the terms responsible for nonlinear optical effects. It is their superlinear dependence on the field strength that accounts for the necessity of an intense source

such as a laser to witness these NLO responses. The field strengths required to observe this anharmonic electron motion and the resulting nonlinear optical effects should be non-negligible in comparison to the fields that bind the electron to the nucleus. These fields are on the order of  $10^{10} \text{ V m}^{-1}$  which correspond to intensities of  $\sim 10^{14} \text{ W cm}^{-2}$ . Certainly, intensities which are considered “non-negligible” vary dramatically depending on the material used or the type of nonlinearity investigated. For instance, in highly  $\pi$ -electron delocalized systems the typical intensity values employed can be severely reduced compared to the values quoted above for atomic outer shell electrons. These values tend to be in the range from 10’s of  $\text{MW/cm}^2$  to several hundreds of  $\text{GW/cm}^2$ .

These resulting nonlinear responses are known to alter the optical properties of a material as well as having the potential to modify the properties of the incident optical signal. Second-order processes (i.e., those governed by  $\beta$ ) are prime examples of the latter. Given that an oscillating dipole will radiate, linear polarization will emit light at the same frequency as the incident optical field (see above). In contrast, the quadratic polarization can give rise to mixing processes where new frequencies, disparate from those of the applied optical field, are generated. These processes include second-harmonic generation, sum- and difference-frequency generation, as well as optical parametric generation. In addition, this second-order term can induce changes in material properties as well. As an example, the Pockels effect (or linear electrooptic effect) involves a change in the refractive index at the frequency of the incident optical field that is proportional to the magnitude of an applied d.c. field. It should be noted that second-order NLO interactions occur exclusively in non-centrosymmetric materials, that is, those materials which do not display inversion symmetry.

Conversely, third-order processes (i.e., terms dictated by  $\gamma$ ) can occur in any material, independent of its symmetry. The cubic polarization, like its predecessor, can produce mixing phenomenon such as third-harmonic generation as well as more generalized four-wave mixing processes. And, perhaps more to the point, it can dramatically modify the properties of a material. For instance, in direct analogy to the Pockels effect, the d.c. Kerr effect (or quadratic electrooptic effect) manifests itself as an index change proportional to the square of an applied d.c. field. However, more interesting are the modifications applied to linear polarization observables by the induced cubic polarization. Unlike in first-order polarization where refraction and absorption are independent of the field strength, third-order polarization imparts a change to the effective value of  $\alpha$  by an amount which is proportional to the second power of the optical field or the intensity (i.e.,  $\alpha_{\text{eff}} = \alpha + \gamma E^2$ ). The intensity-dependent refractive index is therefore related to the real part of  $\gamma$  and is responsible for effects as varied as self- and cross-phase modulation, self-focusing, and phase-conjugation. In the same manner, nonlinear absorption is related to the imaginary component of  $\gamma$ . As stated in Section 1.1, two-photon absorption involves the simultaneous absorption of two photons where the sum of their frequencies ( $\omega_1 + \omega_2$ ) is equivalent to the frequency of a real electronic transition of the medium ( $\Omega$ ). In addition, an effect known as Stimulated Raman Scattering (SRS) can occur if a transition frequency of the medium, normally a vibrational resonance, is equal to the difference in photon frequencies, i.e.  $\omega_1 - \omega_2 = \Omega$ . In each of these two beam interactions, a more intense pump (or excitation) beam (denoted by  $\omega_2$ ) is seen to modify the amplitude of a weaker probe (or signal) beam (denoted by  $\omega_1$ ) by an amount proportional to the pump intensity. Note, the probe beam is usually made weak for ease of interpretation. Since 2PA is more germane to this study, we will henceforth deal with this process exclusively.



A typical way to quantify absorption is to introduce a cross-section which has units of area (cm<sup>2</sup>) and acts as a phenomenological obscuration to the incident radiation. In the regime of linear polarization, this absorption cross-section  $\sigma$  is a constant. However, for 2PA, which arises from the term in the cubic polarization,  $\sigma$  will be linearly proportional to the pump intensity,  $I_2$ . Therefore, one can write:

$$\sigma = \delta F_2 \quad 2.4$$

where  $F_2$  is the photon flux of the pump beam and is equal to  $I_2 / \hbar \omega_2$ .  $\delta$  is defined as the 2PA cross-section [20,21] and is typically given in units of  $1 \times 10^{-50} \text{ cm}^4 \text{ sec photon}^{-1} \text{ molecule}^{-1}$ . This unit is commonly referred to as a Göppert-Mayer or GM unit in honor of the work accomplished by the author in this field. Following the energy exchange between a light beam and a molecular ensemble given by Reference 20, a relationship between  $\delta$  and the imaginary part of the third-order molecular polarizability  $\gamma$  can be established (see Appendix A):

$$\delta(-\omega_1; \omega_1, -\omega_2, \omega_2) = L_1^2 L_2^2 \frac{3\hbar \omega_1^2 \omega_2 \text{Im}(\gamma(-\omega_1; \omega_1, -\omega_2, \omega_2))}{(\omega_1 + \omega_2) \varepsilon_0 c^2 n_1 n_2} \quad 2.5$$

where, once again, index 1 refers to the probe beam and index 2 to the pump beam.  $L$  is the local field factor,  $n$  the refractive index of the medium,  $\varepsilon_0$  the permittivity of free space, and  $c$  the speed of light in a vacuum. Note that the frequency dependence of  $\gamma$ , alluded to in Equation 2.3, clearly indicates that it is the pump beam ( $\omega_2$ ) which will cause loss in the amplitude of the probe beam ( $\omega_1$ ). Equation 2.5 reduces to the well-known expression for degenerate 2PA (see for example References 22 and 23) when  $L_1 = L_2$ ,  $n_1 = n_2$ , and  $\omega_1 = \omega_2$ . Recalling that  $\gamma$  is a fourth rank tensor, it is important to note that it is the orientational average of  $\gamma$  which is used in Equation 2.5. This averaging is calculated according to References 24 and 25 assuming an isotropic medium and linearly polarized input light. Following this averaging,  $\gamma$  becomes a

simple scalar number. This assumption is certainly valid considering that the materials being investigated in this study will be in solution form only.

Microscopic parameters such as  $\delta$  and  $\gamma$  permit direct analysis of the nonlinearities associated with molecular systems. Unfortunately, most NLO characterization techniques (see for example Sections 3.3 and 3.4) extract information about the macroscopic nonlinearity of the material, such as  $\beta$ , the two-photon absorption coefficient. Therefore, it is crucial to be able to find a relationship between microscopic and macroscopic formulae. This is accomplished by first noting that the fields represented in Equations 2.1-2.3 are actually the local or effective electric fields. These fields can include contributions from neighboring molecules in addition to the applied macroscopic field. In order to account for this, the macroscopic fields can be corrected for via Lorentz local field factors (see, for instance, Reference 26). Finally, in order to find the macroscopic polarization, it is merely an issue of summing over all of the induced dipoles per unit volume, i.e.  $\mathbf{P} = \sum_i \boldsymbol{\mu}_i$ . This leads to a relationship between  $\gamma$  and its macroscopic counterpart,  $\chi^{(3)}$ , the third-order susceptibility (Equation A.9):

$$\chi^{(3)}(-\omega_1; \omega_1, -\omega_2, \omega_2) = L_1^2 L_2^2 N \gamma(-\omega_1; \omega_1, -\omega_2, \omega_2) \quad 2.6$$

where  $L_1$  and  $L_2$  are again the local field factors and  $N$  is the density of molecules. Given that the 2PA coefficient  $\beta$  is proportional to the  $\text{Im}(\chi^{(3)})$ , one can easily convert to the molecular parameter  $\delta$  (Appendix A) if necessary. In fact, the definition for  $\delta$  given in Equation 2.5 is derived from the interaction between the *macroscopic* polarization term and an incident optical field (see Appendix A) followed by application of Equation 2.6.

Although high nonlinear susceptibilities are a necessary condition in the development of superior NLO compounds, it should be noted that other macroscopic properties can play crucial

roles in the viability of these materials as well. Among these factors are thermal and photochemical stability, transparency region, as well as the duration or lifetime of the nonlinear mechanism. However, since the main focus of this investigation is to determine how to optimize the molecular nonlinearity, the reader is referred to References 17 and 27 for more information on these issues.

## **2.2 Perturbation Theory – Sum-Over-States Approach**

According to Equation 2.5, in order to theoretically determine the two-photon absorption cross-section the third-order molecular polarizability must be known. A variety of quantum-mechanical approaches can be used to calculate  $\gamma$  and they have been reviewed extensively in the literature [17,28,29]. There are essentially three approaches which are conceptually different: the derivatives technique, the anharmonic or coupled oscillator approach, and the Sum-Over-States (SOS) method. The first technique consists of relating different derivatives of the energy and dipole moment to various terms in their series expansions, as evidenced by Equations 2.2 and 2.3 [19]. Therefore, after obtaining the total energy or dipole moment via quantum-chemical calculations, the polarizabilities can be deduced through subsequent determination of the derivatives of these terms. In this technique, only the wavefunction of the ground-electronic state in the presence of an external electric field must be known to complete the calculation. In the anharmonic oscillator approach, the electrons are considered to be harmonically bound to their nuclei (see Section 2.1) and are coupled to one another [30]. The resonant frequencies of these oscillators become the electronic transition frequencies of the molecule. This approach can give insight into the nature of the nonlinear process without the necessity of evaluating any

molecular orbitals (electronic wavefunctions). Finally, the SOS method involves the calculation of the electronic transition energies and wavefunctions via a quantum-chemical approach. These contributions from the excited states can then be summed based on time-dependent perturbation theory and the molecular polarizabilities may be determined [31,32]. Considering that an accurate determination of the excited state wavefunction is difficult, the first two methods (derivatives technique and anharmonic oscillator approach) are far less computationally significant than the SOS method. This permits the calculation of the NLO responses of large molecular systems by these methods. However, the SOS technique holds two distinct advantages. First, it allows investigation of the frequency dependence of the molecular polarizability, whereas the derivative technique does not. Secondly, often times there are only a few excited states which contribute significantly to the polarizability. The SOS technique can clearly identify these excited states that play essential roles in the NLO response of a molecule. The other methods do not possess this advantage. Given that the main purpose of this study is to identify the essential factors which impact 2PA, the SOS technique will be employed.

We chose to use the SOS expression for  $\gamma$  derived by Orr and Ward [32] since it expressly includes resonance cases (this is elaborated on in Chapter 6). For a general third-order nonlinear process, the formula for the third-order molecular polarizability is:

$$\gamma_{hijk}(-\omega_\sigma; \omega_1, \omega_2, \omega_3) =$$

$$\begin{aligned} & \mathcal{O} \left[ \sum_{lmn} \left\{ \frac{\mu_{gl}^k \bar{\mu}_{lm}^j \bar{\mu}_{mn}^i \mu_{ng}^h}{(\Omega_{lg} - \hbar\omega_\sigma)(\Omega_{mg} - \hbar\omega_1 - \hbar\omega_2)(\Omega_{ng} - \hbar\omega_1)} \right. \right. \\ & + \frac{\mu_{gl}^j \bar{\mu}_{lm}^k \bar{\mu}_{mn}^i \mu_{ng}^h}{(\Omega_{lg}^* + \hbar\omega_3)(\Omega_{mg} - \hbar\omega_1 - \hbar\omega_2)(\Omega_{ng} - \hbar\omega_1)} \\ & + \frac{\mu_{gl}^h \bar{\mu}_{lm}^i \bar{\mu}_{mn}^k \mu_{ng}^j}{(\Omega_{lg}^* + \hbar\omega_1)(\Omega_{mg}^* + \hbar\omega_1 + \hbar\omega_2)(\Omega_{ng} - \hbar\omega_3)} \\ & \left. + \frac{\mu_{gl}^h \bar{\mu}_{lm}^i \bar{\mu}_{mn}^j \mu_{ng}^k}{(\Omega_{lg}^* + \hbar\omega_1)(\Omega_{mg}^* + \hbar\omega_1 + \hbar\omega_2)(\Omega_{ng}^* + \hbar\omega_\sigma)} \right\} \\ & - \sum_{mn} \left\{ \frac{\mu_{gm}^k \mu_{mg}^j \mu_{gn}^i \mu_{ng}^h}{(\Omega_{mg} - \hbar\omega_\sigma)(\Omega_{mg} - \hbar\omega_3)(\Omega_{ng} - \hbar\omega_1)} \right. \\ & + \frac{\mu_{gm}^j \mu_{mg}^k \mu_{gn}^i \mu_{ng}^h}{(\Omega_{mg} - \hbar\omega_3)(\Omega_{ng}^* + \hbar\omega_2)(\Omega_{ng} - \hbar\omega_1)} \\ & + \frac{\mu_{gm}^h \mu_{mg}^i \mu_{gn}^k \mu_{ng}^j}{(\Omega_{mg}^* + \hbar\omega_\sigma)(\Omega_{mg}^* + \hbar\omega_3)(\Omega_{ng}^* + \hbar\omega_1)} \\ & \left. + \frac{\mu_{gm}^h \mu_{mg}^i \mu_{gn}^j \mu_{ng}^k}{(\Omega_{mg}^* + \hbar\omega_3)(\Omega_{ng} - \hbar\omega_2)(\Omega_{ng}^* + \hbar\omega_1)} \right\} \right] \quad 2.7 \end{aligned}$$

This expression is slightly modified [25] from the one appearing in Reference 31 which refers to the macroscopic polarization and not the microscopic polarizability. In the above equations,  $h, i, j, k = x, y, z$  and represent the cartesian coordinates which are used when performing the orientational average of  $\gamma_{hijk}$  referred to in the preceding Section.  $l, m, n$  denote the excited electronic states of the system whereas  $g$  denotes the ground electronic state. The term  $\mu_{lm}^h$  is the  $h$ -th component of the transition dipole moment between states  $l$  and  $m$ . Should the indices  $l$  and

$m$  be the same, the bar over  $\bar{\mu}_{lm}^h$  signifies a change in that state dipole moment with respect to the ground state. Therefore, the compact representation can be written as  $\bar{\mu}_{lm}^h = \mu_{lm}^h - \delta_{lm} \mu_{gg}^h$ . Incidentally, the dipole moment includes those electronic wavefunctions which must be determined quantum-mechanically. This will be elaborated on in Section 2.4.  $\Omega_{lm}$  is defined as  $E_{lm} - i\Gamma_{lm}$ , where  $E_{lm}$  is the electronic transition energy between states  $l$  and  $m$  and  $\Gamma_{lm}$  is the damping constant associated with that transition.  $\Gamma_{lm}$  is a phenomenological damping factor introduced to represent a spectral linewidth for this transition (see Reference 18, Chapter 5.2).  $\omega_1, \omega_2, \omega_3$  denote the frequencies of the incident optical fields with  $\omega_\sigma = \omega_1 + \omega_2 + \omega_3$ . The permutation operator  $\wp$  is used to satisfy the permutation symmetry of the tensor. The summation is carried out over all the permutations of  $\omega_1, \omega_2, \omega_3$ , while simultaneously applying the same permutation to the tensor coordinates  $i, j, k$ . Finally, the primed  $\Sigma$  implies that the summation is taken over all the electronic states except for the ground state. It should be noted that a more truncated version of Equation 2.7 can be written provided damping can be neglected (i.e.,  $\Omega = \Omega^*$ ). Nonetheless, we chose to use the more generalized expression for reasons explained in Chapter 6.

There is an alternative approach to calculating the 2PA cross-section using electronic transition energies and dipole moments. This is known as the 2PA tensor method [24,33] which describes 2PA into a specific electronic state. In order to calculate the entire spectrum, the cross-sections for all 2PA active states are convolved with a normalized lineshape function. This tensorial method only significantly deviates from the SOS method when one approaches a double-resonance situation [38], that is, when the energy of one of the incident photons

approaches the energy of an electronic transition. In order to avoid this discrepancy, the SOS method will be used throughout this paper.

### **2.3 Simplified Essential States Model**

Given that the full SOS treatment requires summation over the entire excited-state manifold, Equation 2.7 can become quite unmanageable for any type of conceptual usage. Therefore, finding approximations which allow one to truncate this complicated expression would reveal a conceptually simplified model for 2PA. As mentioned previously, the SOS method lends itself quite nicely to identifying the few excited states which contribute significantly to  $\gamma$ . In this context, Mazumdar [34] investigated the roles of essential states in the third-order nonlinearity while Dirk [35] and Birge [36] have developed a simplified three-level model for  $\gamma$ . In such approximate expressions, the full SOS formula is truncated by assuming that there is a single excited state  $|e\rangle$  that is strongly one-photon allowed and that there are several two-photon allowed states  $|e'\rangle$  that are strongly coupled to  $|e\rangle$ . This simple three-state model for degenerate 2PA has been successfully applied in numerous studies to date (see, for example, References 22, 23, or 37). In accordance with the literature as well as for ease of use, we will use the essential states model for degenerate 2PA (D-2PA) as well. This is justified considering that the experimentally determined 2PA spectra in this study will be degenerate (or at least quasi-degenerate, see Section 3.3.1) in nature. Chapter 6 will detail the essential states formulation for nondegenerate 2PA (which, as expected, is equivalent to the D-2PA case when the frequencies are the same). When considering only resonant terms in D-2PA and looking

solely at the  $xxxx$  component of  $\gamma$ , the full SOS expression (Equation 2.7) reduces to six terms:

two dipolar terms (D), two two-photon terms (T), and two negative terms (N):

$$\gamma_{xxxx}(-\omega, \omega, -\omega, \omega) = 2 \left\{ \begin{array}{l} \frac{\mu_{ge}^x \bar{\mu}_{ee}^x \bar{\mu}_{ee}^x \mu_{eg}^x}{(\Omega_{eg} - \hbar\omega)(\Omega_{eg} - 2\hbar\omega)(\Omega_{eg} - \hbar\omega)} \quad D \\ + \frac{\mu_{ge}^x \bar{\mu}_{ee}^x \bar{\mu}_{ee}^x \mu_{eg}^x}{(\Omega_{eg}^* - \hbar\omega)(\Omega_{eg} - 2\hbar\omega)(\Omega_{eg} - \hbar\omega)} \quad D \\ - \frac{\mu_{ge}^x \mu_{eg}^x \mu_{ge}^x \mu_{eg}^x}{(\Omega_{eg} - \hbar\omega)(\Omega_{eg} - \hbar\omega)(\Omega_{eg} - \hbar\omega)} \quad N \\ - \frac{\mu_{ge}^x \mu_{eg}^x \mu_{ge}^x \mu_{eg}^x}{(\Omega_{eg}^* - \hbar\omega)(\Omega_{eg} - \hbar\omega)(\Omega_{eg} - \hbar\omega)} \quad N \\ + \sum_{e'} \frac{\mu_{ge}^x \mu_{ee'}^x \mu_{e'e}^x \mu_{eg}^x}{(\Omega_{eg} - \hbar\omega)(\Omega_{e'g} - 2\hbar\omega)(\Omega_{eg} - \hbar\omega)} \quad T \\ + \sum_{e'} \frac{\mu_{ge}^x \mu_{ee'}^x \mu_{e'e}^x \mu_{eg}^x}{(\Omega_{eg}^* - \hbar\omega)(\Omega_{e'g} - 2\hbar\omega)(\Omega_{eg} - \hbar\omega)} \quad T \end{array} \right\} \quad 2.8$$

The D and T terms contain two-photon resonances with the one-photon allowed state  $|e\rangle$  and the two-photon allowed states  $|e'\rangle$ , respectively. The N terms are related to one-photon resonances and therefore will not be discussed here. In Equation 2.8, the factor of 2 is a consequence of the fact that the permutation operator  $\wp$  (see Equation 2.7) gives two equivalent possibilities for the order of the positive  $\omega$ 's.

Certainly, one would be most interested in the peak value of the 2PA spectrum. Therefore, we will concentrate on the terms in Equation 2.8 at their resonances. In considering the D terms, the two-photon resonance into the one-photon allowed state  $|e\rangle$  is given by



$\hbar\omega \approx \hbar\omega_{eg}/2$ . Recalling that  $\Omega_{eg} = \hbar\omega_{eg} - i\Gamma_{eg}$ , one can rewrite the imaginary parts of the D terms as [25]:

$$\text{Im}[\gamma_{D-term}] = \frac{\mu_{ge}^2 \Delta\mu_{ge}^2}{\Gamma_{eg}} \frac{(\hbar\omega_{eg})^2}{((\hbar\omega_{eg}/2)^2 + \Gamma_{eg}^2)^2}. \quad 2.9$$

Here,  $\Delta\mu_{ge} = \bar{\mu}_{ee} = \mu_{ee} - \mu_{gg}$  is the change of the state dipole moment between the ground state  $|g\rangle$  and the excited state  $|e\rangle$ . This underscores the fact that the D term will vanish except in non-centrosymmetric systems. This will be discussed in more detail in Section 5.1. Expanding the second part of Equation 2.9 via a Taylor series and neglecting terms higher than first order with  $\Gamma_{eg} \ll \frac{\hbar\omega_{eg}}{4}$  gives the following:

$$\text{Im}[\gamma_{D-term}] \approx \frac{\mu_{ge}^2 \Delta\mu_{ge}^2}{\Gamma_{eg}} \frac{16}{(\hbar\omega_{eg})^2}. \quad 2.10$$

Plugging this expression into Equation 2.5 and taking into account the averaging factor of 1/5 based on the fact that the  $xxxx$  component of  $\gamma$  is being studied [24], we have

$$\delta_D \approx \frac{6L^4}{5n^2 c^2 \epsilon_0 \hbar} \frac{\mu_{ge}^2 \Delta\mu_{ge}^2}{\Gamma_{eg}}. \quad 2.11$$

The same calculation can be made for the T terms, where the two-photon resonance is into the two-photon allowed state  $|e'\rangle$ . This implies that  $\hbar\omega \approx \hbar\omega_{e'g}/2$ . In this case, the terms in Equation 2.8 can be simplified as follows:

$$\text{Im}[\gamma_{T-term}] = 4 \frac{\mu_{ge}^2 \mu_{ee'}^2}{\Gamma_{e'g}} \frac{(\hbar\omega_{eg} - \hbar\omega_{e'g}/2)^2}{((\hbar\omega_{eg} - \hbar\omega_{e'g}/2)^2 + \Gamma_{eg}^2)^2}. \quad 2.12$$

From this point the Taylor series expansion is truncated according to  $\Gamma_{eg} \ll \frac{\hbar\omega_{eg} - \hbar\omega_{e'g}/2}{2}$  leaving the following simplified formula:

$$\text{Im}[\gamma_{T\text{-term}}] \approx 4 \frac{\mu_{ge}^2 \mu_{ee'}^2}{\Gamma_{e'g}} \frac{1}{(\hbar\omega_{eg} - \hbar\omega_{e'g}/2)^2}. \quad 2.13$$

Using the equation for  $\delta$  as well as the appropriate averaging factor, the final expression becomes

$$\delta_T \approx \frac{6L^4 (\hbar\omega_{e'g}/2)^2}{5n^2 c^2 \epsilon_0 \hbar} \frac{\mu_{ge}^2 \mu_{ee'}^2}{\Gamma_{e'g} (\hbar\omega_{eg} - \hbar\omega_{e'g}/2)^2}. \quad 2.14$$

Unlike the D term, the two-photon term is dominant in centrosymmetric systems where 2PA into the one-photon allowed state is strictly forbidden (see Section 5.1).

Therefore, in order to obtain reasonably accurate 2PA cross-sections from the equations put forth by the simplified essential states model, the molecule under investigation must satisfy the approximations set forth during the derivation. These include: (1) the main contributions to the molecule's nonlinearity must arise from the three states  $|g\rangle$ ,  $|e\rangle$ , and  $|e'\rangle$ ; (2) the dominant terms following the permutation operation should be those resonant terms identified in Equation 2.8; (3) the main contribution to the tensorial term  $\gamma$  will be the component  $\gamma_{xxxx}$ ; (4) the damping term  $\Gamma$  is sufficiently small to justify the Taylor series' truncations. Relaxing any one of these constraints will limit the viability of this model.

## **2.4 Governing Elements of Two-Photon Absorption**

Although the restrictions placed on the essential states model limit its scope in terms of accuracy, the resulting equations for  $\delta$  can still play a powerful role in identifying the key elements which govern the 2PA process. The dominating quantities which appear in the expressions for  $\delta_D$  and  $\delta_T$  (Equations 2.11 and 2.14, respectively) are: (1) the transition dipole

moment between  $|g\rangle$  and  $|e\rangle$ ,  $\mu_{ge}$ ; (2) the transition dipole between  $|e\rangle$  and  $|e'\rangle$ ,  $\mu_{ee'}$ ; (3) the change in state dipole moments between  $|g\rangle$  and  $|e\rangle$ ,  $\Delta\mu_{ge}$ ; and (4) the detuning energy between the one-photon and two-photon allowed states,  $\hbar\omega_{eg} - \hbar\omega_{e'g}/2$ . Understanding how these factors impact 2PA and determining their relative magnitudes in different molecules will give insight into the relationships between chemical structure and NLO response.

#### 2.4.1 Transition and State Dipole Moments

Section 2.2 stresses the fact that the SOS approach (as well as its simplified version) requires quantum-chemical methodology to deduce the ground and excited-state electronic wavefunctions. These wavefunctions are embedded in the definitions for the state and transition dipole moments. The transition dipole moment can be written as [18,26,38]:

$$\vec{\mu}_{if} = e \int \rho_{i \rightarrow f}(\vec{r}) \vec{r} d^3r \quad 2.15$$

where

$$\rho_{i \rightarrow f}(\vec{r}) = \Psi_i^*(\vec{r}) \Psi_f(\vec{r}). \quad 2.16$$

Here,  $\rho_{i \rightarrow f}(\vec{r})$  is given as the transition density between the initial state  $i$  and the final state  $f$  at the spatial coordinate  $\vec{r}$ . Given that the  $\Psi$ 's are the electronic wavefunctions of the appropriate states, the transition densities are the products of (or overlap between) the initial and final state wavefunctions. Therefore, the transition moment is defined as the product of this density and the radial coordinate  $\vec{r}$  integrated over all space, subsequently multiplied by the charge of an electron,  $e$ . In order to determine how to properly optimize the transition dipole moment (and

consequently the 2PA cross-section), an approximation known as the Zero Differential Overlap (ZDO) approximation is often made [25,29]. This states that the overlap between neighboring atomic orbitals is completely neglected such that the complete expression for  $\rho_{i \rightarrow f}(\vec{r})$  can be replaced by the transition densities associated with the individual atoms. Given this conceptually simple picture, factors which allow for optimization of  $\vec{\mu}_{if}$  can be identified [38]: (1) the overlap between the wavefunctions of the initial and final states,  $\Psi_i$  and  $\Psi_f$ , must be maximized; (2) transition densities far from the center of the molecular system should be large (provided the center of the  $\vec{r}$  coordinate system is coincident with the molecular midpoint); and (3) atomic transition densities should have the same sign on the same side of the molecule.

The last two issues can be illustrated graphically. Figure 2.1 shows simulated atomic transition densities for a polyene chain (i.e. a carbon chain consisting of alternating single and double bonds). The diameters of the circles are meant to be proportional to the magnitude of the transition density whereas the shading denotes the sign of the associated electronic transition. These figures represent some arbitrary dipole transition which may occur in a polyene. Figure 2.1a shows the importance of possessing strong transition densities towards the ends of a molecule. The upper molecule exhibits large transition densities congregated at the extremities of the polyene chain whereas the lower molecule reveals densities almost equal in magnitude but positioned at the center of the system. Equation 2.15 clearly indicates that having large densities at the end of the molecule, where  $\vec{r}$  is largest, provides the largest dipole moment. Therefore, the upper molecule would have the optimum transition moment. Large changes in terminal charge density could be facilitated by molecular endgroups which are electron active, such as a strong donating or accepting species. Furthermore, significant  $\vec{r}$  distances could be realized through the use of large conjugated backbones over which charge could migrate. Figure 2.1b

addresses the issue of the relative signs of transition densities on neighboring atoms. The upper molecule possesses transition densities which are nearly all the same sign on one side of the molecule, positive on the left and negative on the right. The lower molecule, on the other hand, shows a pattern of alternating charge densities nearly equivalent in magnitude. One could certainly imagine that the transition densities on adjacent atoms in the lower molecule would essentially cancel one another, whereas the charge densities in the other molecule would only serve to reinforce the effects of neighboring atoms. Given this picture, the upper molecule would possess the greater transition moment. Once again, donor/acceptor substitution could certainly assist this reinforcement. It is important to note that nearly all of the molecules represented in Figure 2.1 have transition densities which reverse signs going from one side of the molecule to the other. This is a necessary condition for transitions to be dipole allowed in molecules possessing strong symmetry. This point will be elaborated upon fully in Section 5.1.

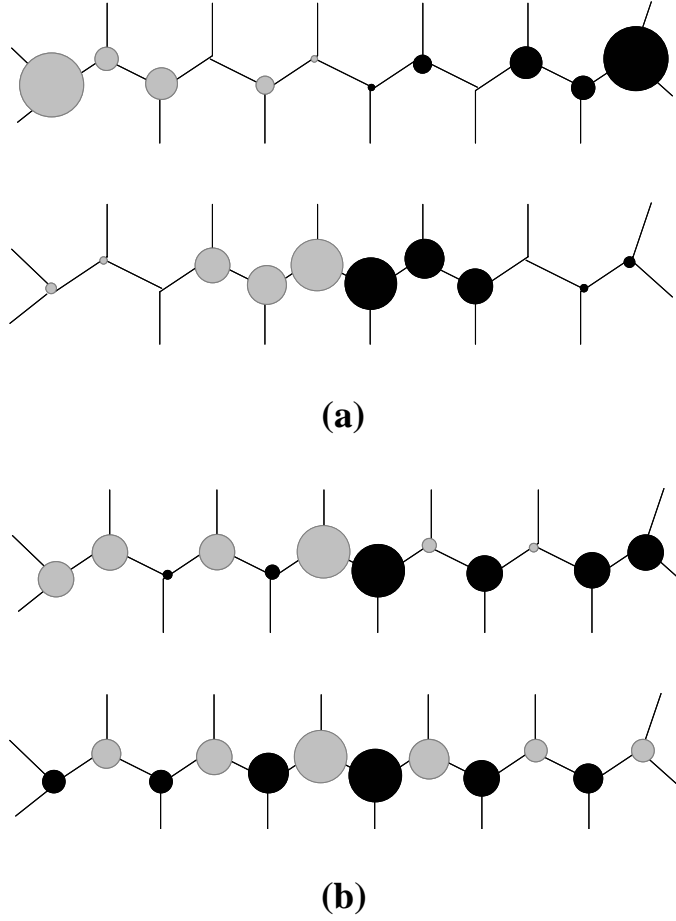


Figure 2.1: Simulated atomic transition densities for a polyene chain. (a) Illustration of the effect of the radial coordinate  $\vec{r}$  on  $\vec{\mu}_{if}$ . (b) Illustration of the effect of the transition density sign change on  $\vec{\mu}_{if}$ .

State dipole moments, which are crucial in the optimization of 2PA in non-centrosymmetric systems (see Equation 2.11), can be represented by the same expression used for the transition moments. State dipole moments are essentially defined by Equation 2.15 with the exception that the initial and final electronic state wavefunctions (given in Equation 2.16) are the same, that is,  $\Psi_i = \Psi_f$ . Although the arguments used above for the transition dipole moments cannot be applied when describing the state dipole moments (also known as permanent dipole moments), the salient term in Equation 2.11 is actually the change of the state dipole moment

between the ground and first excited state,  $\Delta\mu_{ge} = \mu_{ee} - \mu_{gg}$ . Therefore, any logic used when maximizing 2PA via changes in charge density following an electronic transition should be just as applicable when justifying optimization through changes in permanent dipole moments. One might therefore imagine that molecules which possess relatively large permanent dipole moments in the ground state may be prime candidates for efficient two-photon absorbers.

### 2.4.2 Detuning Energy

The second governing element put forth by the essential states model is the energy detuning between the one and two-photon allowed states:  $\hbar\omega_{eg} - \hbar\omega_{e'g}/2$ . This is evidenced in Equation 2.14. To gain a proper understanding of how this term affects the efficiency of 2PA, it is useful to return to the conceptual description of the 2PA process presented in Section 1.1. The physical origin of this enhancement can be interpreted as follows: In 2PA neither photon has the requisite energy to access a real excited state on its own; this can be achieved only through simultaneous absorption of both photons. However, it is intuitive to think of one photon making a virtual transition to the nearest one-photon allowed state and existing in that state for a time  $\Delta t$  determined by the uncertainty principle  $\Delta t > \hbar/\Delta E$ , where  $\Delta E$  is the energy difference between the photon energy and the energy of the nearest one-photon allowed state, the detuning energy. Consequently, this implies that if one reduces the detuning energy the photon can access the excited state for a longer period of time. Since the second photon must arrive during this time duration for simultaneous 2PA to occur, it stands to reason that if this period is lengthened (or equivalently if the detuning energy is decreased) the probability for 2PA must increase.

Therefore, when a photon approaches a resonance (small detuning energy) dramatic enhancement of the 2PA should be observed. This phenomenon of resonance enhancement is illustrated in Figure 2.2 where 2PA from the ground state ( $|g\rangle$ ) to the two-photon allowed state ( $|e'\rangle$ ) is mediated by the one-photon allowed excited state ( $|e\rangle$ ). Schematic (b) illustrates how the detuning energy decreases (in comparison to schematic (a)) as  $|e\rangle$  approaches resonance with the first photon energy thereby enhancing the two-photon absorptivity. However, it should be noted that the minimum detuning energies achievable are inevitably limited by the natural linewidth of the transition, given by  $\Gamma_{eg}$ <sup>1</sup>. Beyond this point, simultaneous 2PA, an instantaneous third-order nonlinear process, gives way to excited-state absorption (or two sequential one-photon absorption processes), an effective third-order nonlinearity. This would result in the loss of any potential benefits true 2PA affords (see Section 1.1). Excited-state absorption is illustrated in Figure 2.2c.

---

<sup>1</sup> The minimum detuning energies are further limited by any associated inhomogeneous broadening mechanisms which may serve to reduce the transparency region.



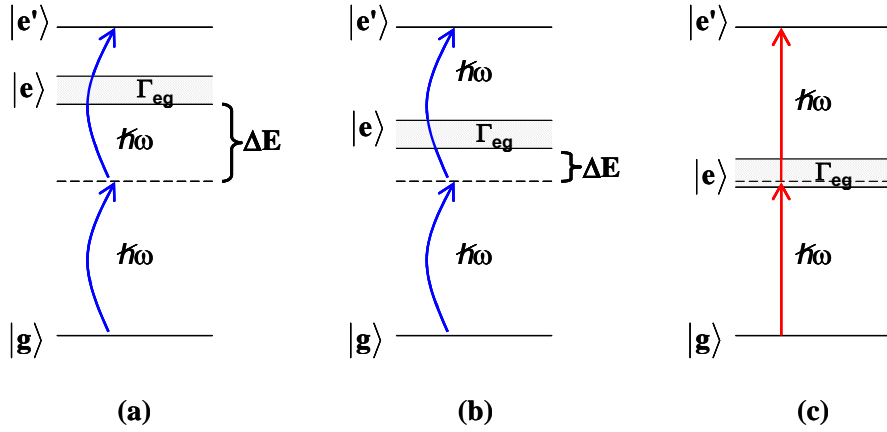


Figure 2.2: Resonance enhancement of 2PA. Schematics (a) and (b) illustrate the decrease in detuning energy ( $\Delta E$ ) as one approaches resonance. (c) Illustration of sequential 2PA, or excited-state absorption.

Since Equation 2.14 deals with degenerate 2PA into  $|e'\rangle$ , the photon energy can be rewritten as  $\hbar\omega \approx \hbar\omega_{e'g}/2$  and the detuning energy becomes  $\hbar\omega_{eg} - \hbar\omega_{e'g}/2$  as stated above. Although the above arguments assume a centrosymmetric system (i.e., dipole selection rules apply), resonance enhancement merely requires an intermediate state to exist. Therefore, 2PA into higher lying states for non-centrosymmetric systems should certainly benefit from this enhancement as well. The key to exploiting this enhancement lays in red-shifting the first excited state towards the incident photon energy. Methods to achieve this will be discussed in Section 5.6.

### 2.4.3 Transition Dipole Moment Orientation

The final element which influences the strength of 2PA is not immediately evident from the results generated by the essential states analysis. This aspect involves the orientation of the transition dipoles with respect to one another and the fact that they are not, in general, completely parallel. Certainly this is accounted for in the full SOS treatment (Equation 2.7) by the tensorial nature of  $\gamma_{hijk}$  and the orientational average performed on it (see Section 2.1). On the other hand, the essential states model neglects the vector nature of the transition moments and makes the assumption that the moments are parallel (this is verified by the scalar values for  $\mu_{ge}$  and  $\mu_{ee'}$  given in Equation 2.14). In truth, the angles between the two transition moments have been found to be greater than  $40^\circ$  [38] in some molecules. In these cases, Cronstand *et al.* [39] recommend that  $\mu_{ee'}$  be treated as an effective transition dipole moment. Essentially this effective dipole is a projection of the magnitude of the transition dipole vector  $|\mu_{ee'}|$  modified according to the angle between the two transition dipole vectors:

$$\mu_{ee'}^{eff} = |\mu_{ee'}| \sqrt{\frac{2 \cos^2(\theta) + 1}{3}} \quad 2.17$$

where  $\theta$  is the angle between  $\mu_{ge}$  and  $\mu_{ee'}$ . For large angles, this deviation can become quite important and therefore, for optimal efficiency, the dipole moments should be co-aligned. It should be noted here that, in this study, whenever the essential states model is invoked and calculations are accordingly made, the value for  $\mu_{ee'}^{eff}$  will be used in place of  $\mu_{ee'}$ . However, for all of the molecules studied in this paper, the discrepancies between  $\mu_{ee'}^{eff}$  and  $\mu_{ee'}$  were found to be quite small, thus implying that  $\theta$  is negligible.

## CHAPTER 3: METHODOLOGY

The previous Chapter analyzed how the nonlinear optical properties of a system (specifically two-photon absorption) are fundamentally linked to the interactions between a molecule and an applied optical field. Prudent manipulation of the molecular structure can thereby facilitate construction of an efficient two-photon absorber. This Chapter details the experimental methodology necessary to extract these optical properties from the group of fluorene derivatives under investigation. Given the experimentally determined 2PA spectra and the relationships described above, we can put forth plausible explanations for identifiable trends between the two. These will be the subject of Chapter 5.

This Chapter is organized as follows: The first Section covers the techniques we use for determining the linear optical properties of our molecules, i.e., strength, location and spectral contour of the absorption and emission spectra. Multiple techniques are employed to obtain the 2PA spectra with the expressed intention of providing mutual support for the experimental results. The first technique, namely two-photon fluorescence spectroscopy, is described in Section 3.2. In addition to the description of the photophysical phenomenon itself, the experimental apparatus is characterized, the method for extracting the 2PA cross-section is detailed, and correction measures for the spurious inner-filter effect are laid out. Section 3.3 provides a write-up for the technique of white-light continuum pump-probe spectroscopy, the apparatus that it uses, and the effects of cross-phase modulation artifacts on the transient absorption data acquired. A brief explanation of the Z-Scan technique follows in Section 3.4.

Finally, the methodology for the quantum-chemical analysis of the molecules is expounded upon in Section 3.5. This analysis is meant to supplement the experimental data in that it can provide valuable information about certain optical properties which might otherwise be unattainable (i.e., state dipole moments, transition moments between higher level excited states, etc.). Furthermore, this information, when applied to the Sum-Over-States perturbation theory expression for  $\gamma$  (either fully-converged or simplified), can generate the theoretical values for the 2PA cross-sections.

### 3.1 Linear Spectroscopic Techniques

The linear properties we have chosen to investigate for our group of fluorene molecules are: the absorption spectra, steady-state excitation anisotropy spectra, fluorescence spectra and fluorescence quantum yields. Most of the experimental methodology is catalogued in References 40 and 41. Absorption spectra are obtained using a Cary-3 UV-visible spectrophotometer. These spectra identify the locations of the absorption maxima and give their strengths in terms of molar absorptivities,  $\epsilon$ . In turn, these values can be used to determine the magnitude of the transition dipole moment between the ground and first excited state,  $\mu_{ge}$ , for these molecules. As mentioned in Section 2.4.1, this dipole moment is one of the controlling factors for 2PA.  $\mu_{ge}$  can be calculated from the integrated strength of the first electronic transition band ( $|g\rangle$  to  $|e\rangle$ ) in the linear absorption spectrum according to the following [37,42]:

$$\mu_{ge} = \left[ \frac{1500(\hbar c)^2 \ln 10}{\pi N_A E_{ge}} \int \epsilon_{ge}(\nu) d\nu \right] \quad 3.1$$

Here,  $N_A$  is Avogadro's number,  $E_{ge}$  is the transition energy in eV, and  $\epsilon_{ge}(\nu)$  is the extinction coefficient in  $M^{-1} \text{ cm}^{-1}$  at the wavenumber  $\nu$  which is given in  $\text{cm}^{-1}$ . It is important to note that the integral is performed over the first electronic transition band in wavenumber space. All constants are given in cgs units.

The excitation anisotropy spectra are measured with a PTI Quantamaster spectrofluorimeter under 90 degree excitation in a T-format method [43]. In order to prevent fast rotation of the molecules during their excited state lifetime (and subsequent destruction of anisotropy), the solutions are made in viscous silicon oil. These spectra help to determine the nature of the absorption bands (i.e. location of electronic transitions as well as relative transition dipole moment orientations). The fluorescence spectra and quantum yields ( $\eta$ ) are recorded using the same spectrofluorimeter described above. The fluorescence quantum yields are measured using a standard method [43], relative to Rhodamine 6G in ethanol ( $\eta=0.94$ ) [44]. When determining quantum yields (as well as molar absorptivities), solution concentrations are chosen to be  $\sim 10^{-6}$  M in order to reduce possible error induced by reabsorption of the excitation beam. Further spectroscopic analyses, including excitation spectra, fluorescence lifetimes and time-resolved emission spectra, were also carried out on a number of the compounds. The details of these experiments are beyond the scope of this study, however they can be found in Reference 41.

### **3.2 Two-Photon Fluorescence Spectroscopy**

Within this work, multiple techniques for nonlinear spectroscopy are used to characterize the NLO properties of the organic compounds. Each method has its own unique benefits and to a

certain extent they complement one another. However, the most crucial reason multiple techniques are employed is due to the nature of nonlinear spectroscopy itself. Unlike linear absorption spectroscopy where the absorption coefficient  $\alpha(\lambda)$  is dependent solely upon the incident wavelength, nonlinear absorption is dependent on the incident irradiance as well,  $\alpha(\lambda, I)$ . This added requirement over linear spectroscopy makes measurement much more difficult. The laser energy and the temporal and spatial modes (and any possible changes with propagation through the sample), must be accurately monitored at each excitation wavelength to determine  $I(\lambda_e) = \text{energy}(\lambda_e)/\text{area}(\lambda_e)/\text{time}(\lambda_e)$ . For this very reason, utilizing several techniques can provide further confidence in the end results.

The sources used for these spectroscopic techniques are as follows: a fiber ring oscillator, Ti:sapphire based regenerative amplifier laser system (CPA-2001, CLARK-MXR) which operates at 775 nm, a 1 kHz repetition rate, and provides laser pulses with 840  $\mu\text{J}$  of energy with a temporal duration of 150 fs. This laser, in turn, pumps two identical optical parametric amplifier (OPA) systems (TOPAS, Light Conversion Limited) which can produce 100-150 fs pulses with up to 60  $\mu\text{J}$  of energy per pulse and tunability over a broad spectral range through the visible up through the near infrared (i.e., 570-2100 nm or 2.2-0.6 eV).

The first nonlinear characterization method we will describe employs the process of two-photon induced fluorescence. In this process, a strong pump beam excites a material via 2PA and subsequently, provided the material is fluorescent, the material radiatively relaxes to its ground state. By monitoring the strength of the two-photon induced fluorescence one can determine the value of the 2PA cross-section,  $\delta$ , for that particular pump wavelength. Since induced fluorescence is the monitored behavior, the light is being sensed against a zero-background. In other words, in the absence of two-photon excitation there is no signal. This fact

coupled with the use of highly sensitive detection devices (e.g. photomultiplier tubes) promises a highly responsive technique. Finally, varying the wavelength of the pump beam while monitoring the induced fluorescence allows reconstruction of the entire degenerate 2PA spectrum of the material. Here “degenerate” merely implies that the two photons involved in the excitation process are of the same energy. This method of two-photon fluorescence (2PF) spectroscopy was initially implemented by Xu and Webb in 1996 [16].

### 3.2.1 Experimental Apparatus

Our experimental apparatus for measuring 2PF is diagrammed in Figure 3.1. The labels for the different components in the system are as follows: M – silver mirror,  $\lambda/2$  WP – broadband half waveplate, P – calcite GLAN polarizer, A – adjustable iris diaphragm, CXL – convex lens, CCL – concave lens, FL – focusing lens ( $f = 250\text{mm}$ ), CL – fluorescence collection lens, PMT – photomultiplier tube, PC – personal computer for data acquisition. The sample holder compartment is housed within the same spectrofluorimeter apparatus (denoted by the dashed box) which is used for one-photon fluorescence spectroscopy (see above). The samples used in this study are solutions which are contained within 1 cm path length quartz cuvettes whose concentrations are typically  $10^{-4}$  M. The pump source for this characterization technique is one of the two OPA’s (TOPAS-1) described above. Its output energy can be attenuated using the polarization rotator and GLAN polarizer. The pump beam then passes through the first iris which is aligned such that the beam travels through the centers of CXL and CCL. This on-axis geometry assures that minimal off-axis aberrations are induced by the system. These two lenses act as a 4x beam expander such that only the central portion of the beam passes through the

second iris (D~3 mm) while the remainder is blocked. Truncating the beam in this manner assures that the spatial profile of the excitation beam is no longer Gaussian but very nearly flat-top prior to striking the focusing lens. In this manner, the spatial extent of the focused beam on the sample resembles a diffraction limited Airy pattern and is essentially independent of the initial beam profile exiting the OPA. The sample is then excited by a semi-collimated beam (~200  $\mu\text{m}$ ) over the full path length of the cell with incident energies ranging from 10-150 nJ. Since the geometry is a 90 degree excitation format, the pump beam is directed parallel and in close proximity to the left edge of the sample cuvette such as to minimize reabsorption of the emission (this will be discussed in detail below).

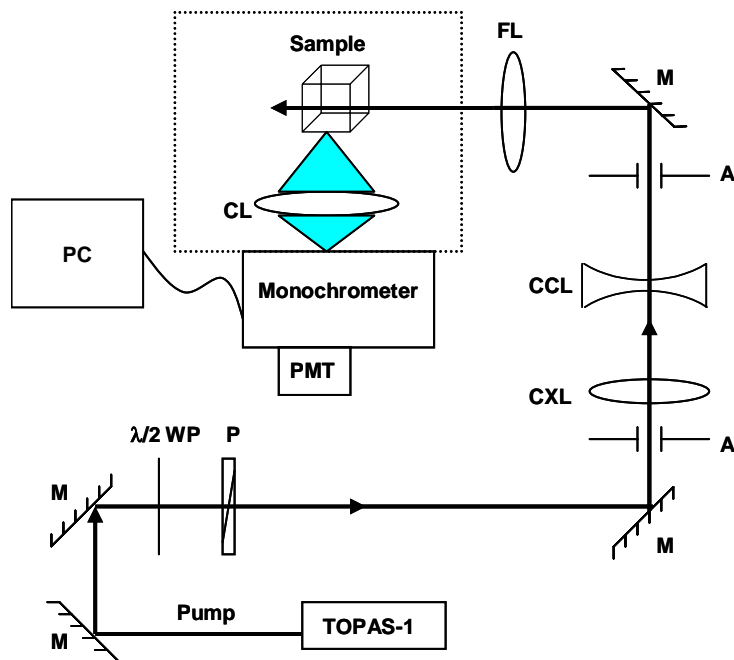


Figure 3.1: Schematic for the two-photon induced fluorescence experiment.



Following excitation of the sample, the two-photon induced fluorescence is collected and the fluorescence spectrum is recorded through the use of the computer actuated monochromator and sensitive PMT detector. The spectral sensitivity afforded by the detection system covers the 250-800 nm range (two separate PMTs are used to attain the full spectral range). The detectors are operated in the analog mode (dc voltage output) as opposed to the more common photon-counting mode since the PMTs were found to saturate in this latter regime most likely due to the large quanta of photons striking the dynodes in such a short temporal duration ( $\sim 100$ s of fs). The dynamic range of the PMTs in the analog mode is limited to 0.03-3.0 Volts in order to insure operation in the linear regime of the detector. The fluorescence spectrum is corrected for the spectral responsivity of the spectrofluorimeter (monochromator and PMT) and then integrated over the entire emission range to obtain the total integrated fluorescence for a particular pump wavelength. The entire spectrum is recorded (1) to obtain the total two-photon induced fluorescence in order to ascertain  $\delta$  and (2) to make certain that the contour of the up-converted fluorescence spectrum is independent of the pump frequency (which is not always the case for some materials [45]). Finally, by varying the pump wavelength we can reconstruct the full 2PA spectrum. It should be noted that the strength of the induced fluorescence should exhibit a quadratic dependence on the pump irradiance [16] provided that this photophysical phenomenon occurs as a result of two-photon absorption. Plotting the log of the fluorescence signal versus the log of the pump irradiance should reveal a linear curve with a slope of 2 for a 2PA induced process (slopes of  $<2$  imply additional contributions from linear absorption whereas slopes of  $>2$  imply that higher nonlinear processes such as three-photon absorption or two-photon assisted excited-state absorption may be occurring as well). In order to ensure that the fluorescence

exhibits the proper quadratic dependence, the fluorescence signal is acquired for a number of different pump irradiances for each sample under investigation.

### 3.2.2 Inner Filter Effect

The highly concentrated solutions ( $\sim 10^{-4}$  M) used in this experimental technique can produce adverse effects when dealing with absorption/emission processes. These consequences, known as inner-filter effects, involve significant attenuation of the excitation or emission beams. Specifically there are two such processes, the primary absorption effect and the secondary absorption effect [46]. The primary absorption effect is a process in which the excitation beam is attenuated before arriving at the region of the sample viewed by the collection optics as well as through the detected volume (assuming a 90 degree excitation format as described above). For this reason (as mentioned in Section 3.1), when determining quantum yields using one-photon fluorescence, the peak optical density (OD) of the solution is normally kept below 0.05, ensuring no more than 5% attenuation of the excitation beam. This OD corresponds to a concentration on the order of  $10^{-6}$  M. Although the concentrations are significantly higher in the 2PF experiments ( $\sim 10^{-4}$  M), the primary absorption effect is negligible because the excitation wavelengths are nominally twice as long as those used for linear excitation thus producing little to no attenuation. This, however, is not the case for the secondary absorption effect. In this process, the fluorescence emission may be reabsorbed before it passes beyond the cell window for detection. Although the geometry of the 2PF experiment is designed to minimize this effect (see above), the high concentrations involved do not allow for complete elimination of this deleterious effect. This process is illustrated in Figure 3.2. Clearly, there is significant overlap between the two

spectra. Therefore when the two-photon induced fluorescence spectrum is measured, shown by curve (b), there is nearly complete attenuation of the portion of the fluorescence spectrum which is overlapped with the absorption spectrum. This effect will be more pronounced in samples which possess a smaller Stokes shift, that is, a small shift between the peaks of the absorption and emission spectra.

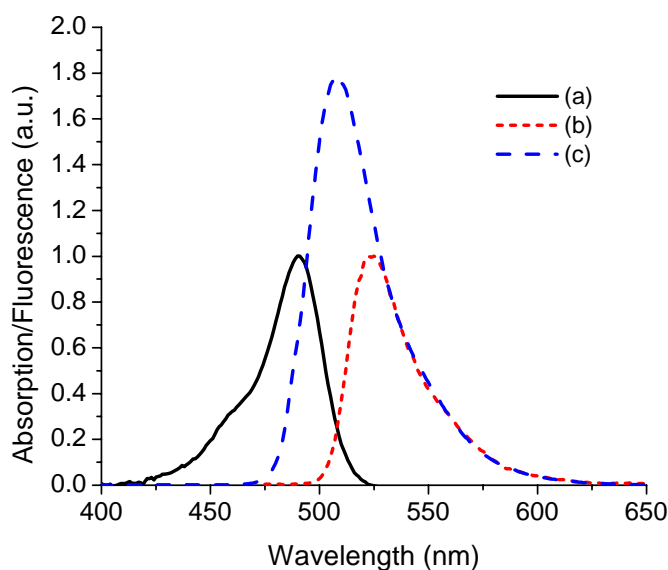


Figure 3.2: Illustration of the inner filter effect for a solution of Fluorescein in water (pH=11). (a) Normalized absorption spectrum. (b) Normalized 2PF spectrum. (c) One-photon fluorescence spectrum normalized to the unabsorbed portion of the 2PF spectrum.

Since the 2PA cross-section is proportional to the total induced fluorescence (see below), failure to detect the entire 2PF spectrum will surely underestimate the true nonlinearity of the sample. Given that we cannot completely eliminate this inner-filter effect (IFE), we must correct for it instead. This is accomplished by normalizing the one-photon fluorescence spectrum (in

which there is negligible reabsorption) to the portion of the 2PF spectrum that has not experienced the IFE. Curve (c) in Figure 3.2 illustrates this correction. By matching up the linear spectrum to the unaffected fraction of the 2PF spectrum, the reabsorption due to the IFE can be adjusted. This assures a much more accurate determination of the 2PA cross-section.

### 3.2.3 Determination of the Two-Photon Absorption Cross-Section

As stated in the previous two sections, the magnitude of the two-photon induced fluorescence is proportional to both the two-photon absorption cross-section,  $\delta$ , and to the square of the incident irradiance,  $I$ . In order to determine  $\delta$ , an exact relationship between the induced fluorescence and the excitation power must be determined. According to Reference 16 (see Appendix B), the intensity of the collected 2PF signal for the experiment described above is given by:

$$\langle F(t) \rangle = \frac{1}{2} g \Phi \eta C \delta \left( \frac{\pi (N.A.)^2}{\lambda^2} \right)^2 \langle P(t) \rangle^2 \int_V dV S^2(r, z) \quad 3.2$$

where  $\langle \rangle$  indicates time-averaging,  $g$  is a measure of the second-order temporal coherence of the excitation source,  $\Phi$  is the overall collection efficiency of the spectrofluorimeter,  $\eta$  is the fluorescence quantum yield of the sample,  $\delta$  is the two-photon absorption cross-section, N.A. is the numerical aperture of the focusing lens,  $\lambda$  is the wavelength of the excitation source,  $P(t)$  is the incident laser power, and  $S(r, z)$  describes the spatial distribution of the excitation light which is integrated over the entire excitation volume. The quadratic dependence of the 2PF signal on the incident irradiance implies a strong dependence on the spatial and temporal properties of the

incident light as evidenced by Equation 3.2. The spatio-temporal properties of the excitation light must therefore be well characterized which can become a tedious process often prone to error. Furthermore, since the fluorescence is emitted into  $4\pi$  steradians, the collection geometry of the system must also be accurately determined.

Therefore, as an alternative to this time-consuming endeavor, the fluorescence measurement made is a relative one. The 2PF results obtained for the sample under investigation are calibrated against reference standards with known two-photon absorptivities. By measuring the induced 2PF at a particular wavelength for the unknown sample as well as the reference standard, we can eliminate the dependencies of the method on the spatio-temporal properties of the excitation light as well as on the collection geometry. Taking the ratio between the sample and reference 2PF signal and solving for  $\delta$  we obtain:

$$\delta_s = \frac{\langle F \rangle_s \Phi_R \eta_R C_R \langle P \rangle_R^2}{\langle F \rangle_R \Phi_S \eta_S C_S \langle P \rangle_S^2} \delta_R \quad 3.3$$

where the subscripts S and R refer to the sample and the reference, respectively. The characterization method now merely involves determining the incident power and the fluorescence signal obtained for each wavelength. The quantum yield and the concentration are parameters that can be easily ascertained for each sample. Finally, although determination of the collection geometry is no longer necessary, the overall collection efficiency still includes certain factors which must be taken into account. The collection efficiency can be expressed as  $\Phi = \phi_{\text{spec}} \times \phi_{\text{sol}}$  [37], where

$$\phi_{\text{spec}} = \left[ \int f_{\text{fluor}}(\lambda) \times f_{\text{spec}}(\lambda) d\lambda \right] / \int f_{\text{fluor}}(\lambda) d\lambda \quad 3.4$$

is the correction factor due to the spectral responsivity of spectrofluorimeter (i.e. monochromator and PMT). In Equation 3.3,  $f_{\text{fluor}}(\lambda)$  is the fluorescence spectrum and  $f_{\text{spec}}(\lambda)$  is the normalized

spectrofluorimeter response.  $\phi_{\text{sol}}$  is proportional to  $n^{-2}$  (where  $n$  is the refractive index of the solution) and accounts for the differences in the solid angles subtended by the collection lens when using solutions of disparate solvents. However in our experimental design, the excitation beam is flush with the window of the cell and the emission passes through a negligible amount of solvent; therefore this factor is normally neglected.

The reference standards which we use are: Fluorescein in water (pH=11) [16], Rhodamine B in methanol [16], and 1,4-bis(2-methylstyryl)benzene in cyclohexane [47] with associated quantum yields of 0.9, 0.7 and 0.9, respectively. Their two-photon absorption spectra are shown in Figure 3.3 where the cross-sections (in GM units) are plotted versus their associated excitation wavelengths. The spectral overlap of the curves assures us that we can determine continuous 2PA spectra for our target samples over a range from 560-1030 nm. The absolute errors associated with this characterization technique are estimated to be  $\pm 20\%$  and are mainly attributed to the uncertainties in the two-photon absorptivities of the reference standards and the calculated values of the fluorescence quantum yields. However, it should be noted that relative errors from one measurement to the next can be as small as  $\pm 6\%$ .

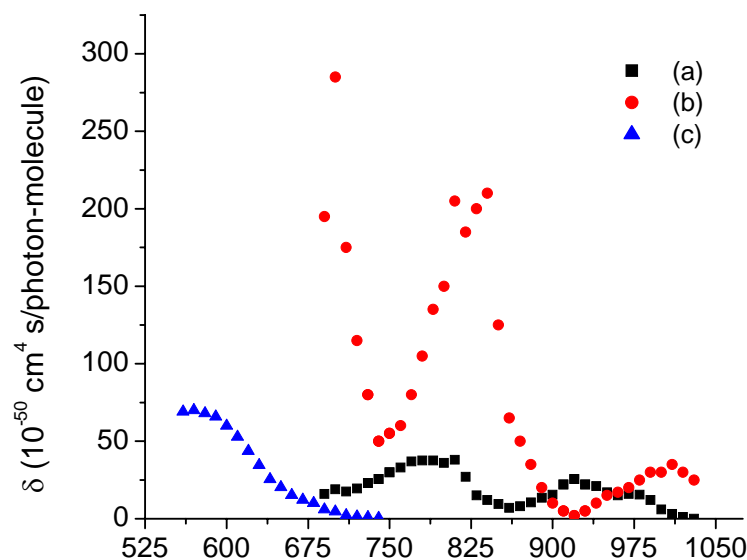


Figure 3.3: Two-photon absorption spectra of the reference standards used in the 2PF technique. (a) Fluorescein in water (pH=11), (b) Rhodamine B in methanol and (c) 1,4-bis(2-methylstyryl)benzene in cyclohexane.

### 3.3 White-Light Continuum Pump-Probe Spectroscopy

2PF is a highly sensitive spectroscopic technique, however its main shortcomings are two-fold: (1) it requires highly fluorescent samples which may not always be relevant and (2) it provides no information concerning the time evolution of the nonlinearity. The temporal dynamics of a nonlinear phenomenon can, often times, aid in distinguishing its mechanism. For example, in degenerate 2PF measurements, excited-state absorption can lead to upconversion fluorescence through subsequent absorption of another photon. This effect could artificially inflate the value of the measured nonlinearity. In order to differentiate between these two mechanisms, an additional energy dependent measurement must be performed as well (see Section 3.2.1). The pump-probe technique offers a temporally discriminative alternative. In this

technique, a strong excitation pulse (pump) induces a nonlinearity within the sample and a weak probe pulse monitors the dynamics of that nonlinearity. Again, the probe pulse is made weak purely for ease of interpretation of the experimental results. Varying the time delay between the two pulses while recording the temporal evolution of the probe beam allows temporal discrimination of the nonlinear processes. Provided the pump and probe pulses are ultrashort in duration ( $\sim$ fs), one can distinguish between essentially instantaneous processes ( $\sim$ fs), such as those due to bound electronic nonlinearities (i.e. 2PA), and “long-lived” processes (100’s ps to ns), such as excited-state absorption. In addition to this chronological information, the magnitude of the induced nonlinearity can be calculated provided the irradiance of the excitation pulse is known. Finally, since it is the transmission of the probe beam which is monitored, there are no restrictions regarding the fluorescence efficiency of the sample.

### 3.3.1 Experimental Technique

In order to characterize a sample’s 2PA spectrum, we employ a slight variation of the pump-probe technique where the single wavelength probe pulse is replaced with a white-light continuum (WLC, [48,49,50]) probe. The broadband nature of this WLC pulse supplies spectral information about the observed nonlinearity and provided the probe pulse retains its ultrashort characteristics, the temporal dynamics can be extracted as well [51]. In this method, the 2PA process requires simultaneous absorption of one photon from the pump beam and one photon from various spectral portions of the probe beam. The outcome is the nondegenerate 2PA spectrum of the sample. This method could, in principle, be a single shot technique since the large spectral extent of the probe beam could allow for full characterization of the sample with a



single laser pulse. However, in practice, the temporal delay between the pump and probe must be scanned since the WLC is strongly chirped (temporal dispersion of frequency) and the temporal coincidence between the pump and probe (i.e. "zero delay") for one wavelength is different than for another wavelength. This chirp is a result of the generation process itself where the continuum experiences group velocity dispersion (GVD) during propagation through the generation medium [48]. Nonetheless, the necessity to scan the temporal delay between pump and WLC probe is not seen as a disadvantage since it can provide the means to distinguish the physical mechanisms behind a nonlinearity.

Although the chirp of the WLC is not an imposition, experimentally determined raw data must be corrected for temporal walk-off due to group-velocity mismatch (GVM). The nondegenerate character of the experiment entails that pump and probe pulses travel through the sample at different group velocities and can physically walk-off from one another in time within the sample. This walk-off causes the effective interaction length to be significantly reduced compared to the degenerate case (where the pump and probe pulses at the same frequency travel with equal group velocities within the sample), and will artificially reduce the magnitude of the true nonlinear signal. However, as this is a purely linear phenomenon, these GVM-induced artifacts can be completely accounted for in the data analysis provided knowledge of the linear dispersion of the sample is known. Since many of the materials under investigation have dispersion properties which are not yet catalogued, linear characterization was performed using a technique known as the optical Kerr effect (OKE). The OKE method is a cross-correlation technique where some instantaneous nonlinear process, such as second-harmonic generation or the optical Kerr effect (which is preferable since no phase-matching is required), is used to obtain the cross-correlation signal [49,52,53]. This technique generates full characterization of

the chirp of the WLC (i.e., the relation between wavelength and time) and furthermore can measure the GVD of an unknown sample. From OKE measurements, with and without the sample in the probe path, the difference in arrival time for a fixed frequency component of the continuum gives the group index of the material. Given the broad bandwidth of the probe, the dispersion of the group index over the region of interest can be determined. Although the necessity of linear characterization implies that an additional measurement be carried out to determine the nonlinearity, the method is quite rapid as only minimal changes in the transient absorption set-up are required.

Armed with knowledge of the linear dispersion of the sample, we have found a single dynamical equation which takes into account linear propagation effects for this nondegenerate pump-probe interaction in a 2PA nonlinear medium [54]. This allows us to determine the full 2PA spectrum for the material under investigation.<sup>2</sup> The absolute errors associated with this WLC pump-probe method are determined to be  $\pm 15\%$ , where the largest source of uncertainty involves the calculation of the irradiance of the excitation beam. Like the 2PF technique described above, the relative errors can be much smaller (i.e.  $\pm 6\%$ ). A more detailed description of the aforementioned method can be found in References 55 and 56. Finally, it should be emphasized that the outcome of this method is the *nondegenerate* 2PA spectrum due to the disparate nature of the pump and probe photon energies involved. In general, we would like to keep the energy of the pump photon less than half the energy of the linear absorption edge of the sample. In doing this, we assure negligible degenerate 2PA (D-2PA) of the pump beam. This allows us to avoid absorption of the pump as well as subsequent excited state absorption of the

WLC probe beam which could interfere with our data analysis. However, the magnitude of the nondegenerate 2PA (ND-2PA) spectrum is highly dependent on both the choice of the pump photon energy as well as the band structure of the sample under investigation (this point will be discussed in detail in Chapter 6). Therefore, for consistency with the results of the other D-2PA techniques, when employing the WLC pump-probe method, the pump photon energy is chosen such that it coincides with the peak of the D-2PA spectrum. Although the resulting nonlinear spectrum is still, in principle, nondegenerate in nature, in practice, the discrepancies between the D-2PA and ND-2PA spectra will be minor. As a consequence of the pump photon energy chosen, great care is taken to assure that D-2PA of the pump beam itself does not adversely affect the final results.

### 3.3.2 Experimental Apparatus

#### 3.3.2.1 Pump-Probe Set-Up

The experimental apparatus for the WLC pump-probe technique is diagrammed in Figure 3.4. The optical components are labeled as follows: PD – photodiode,  $\lambda/2$  PR – polarization rotator, P – calcite Glan polarizer, A – adjustable iris, L – focusing lens, F – dielectric short wave pass filter, CaF – Calcium Fluoride window, M – silver mirror, BS – broadband beamsplitter, RR – silver retroreflector, BD – Beam Dump, SPEC – dual fiber input spectrometer, CCD – dual

---

<sup>2</sup> The WLC pump-probe method as described in References 54 and 55 actually extracts the nondegenerate 2PA coefficient,  $\beta_{ND}$ , from the experimental data. In order to convert to the nondegenerate 2PA cross-section,  $\delta_{ND}$ , one

Charge Couple Device array. The pump beam (upper optical path) is generated by one of the OPA systems (TOPAS-1) and sampled by a photodiode, via a beamsplitter, to monitor the fluctuations in the pump energy. The pump beam is subsequently sent through a half waveplate and polarizer. Various states of polarization are emitted from the OPA depending on the spectral range being used and in order to assure that the pump and probe beams have their polarizations oriented parallel to one another (in the vertical plane) this rotator/polarizer pair is used. This pair must also be broadband through the entire visible and near-IR regimes in order to fully accommodate the OPA tunability. The pump pulse then passes through the delay line which is equipped with a fine resolution translation stage. For an essentially instantaneous process such as 2PA, the optical nonlinearity only occurs during temporal overlap of the pump and probe pulses. In order to properly sample this transient absorption signal for pulse durations of 100-150 fs, we use steps with a temporal resolution of 26.6 fs which corresponds to a linear translational distance of 4  $\mu\text{m}$  (double pass). The pump beam passes through a focusing lens which can be translated along the optical beam path in order to control the magnitude of the pump irradiance striking the sample. The samples used in this study are solutions which are contained within 1 mm path length glass cuvettes whose concentrations are typically  $10^{-2}$  M. Finally, the pump beam passes through the sample at a shallow crossing angle with respect to the probe beam path ( $<5$  degrees) to prevent spatial walk-off within the sample; the pump beam is subsequently impeded by a beam dump in order to avoid collection by the detection system.

---

must use Equation A.12.

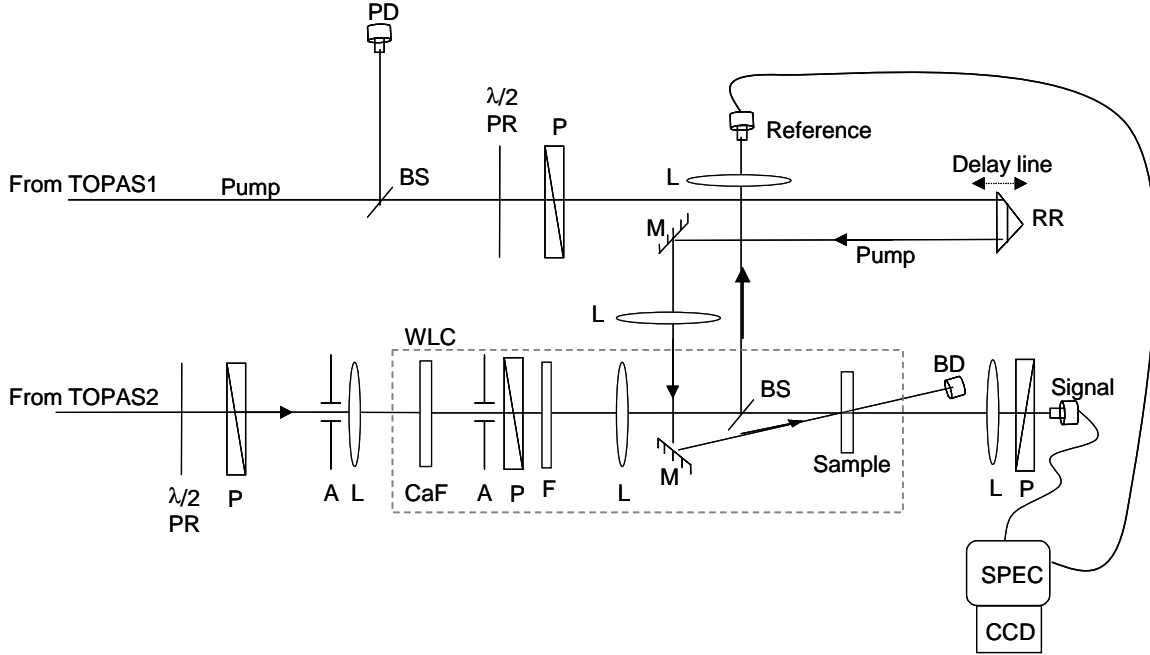


Figure 3.4: Schematic for the white-light continuum pump-probe spectroscopy experiment.

The probe beam originates from the second OPA system (TOPAS-2) and will serve to generate the WLC probe beam. The source wavelength was chosen to be 1300 nm for two reasons: (1) it is a signal wavelength of the OPA and therefore possesses good power stability (an important factor governing the stability of the WLC) and (2) the color lies outside the spectral band of the WLC which we normally utilize. The latter point assures that the excitation power which is not converted into WLC can be spectrally separated from our region of interest. The subsequent four components are crucial for the generation of a broad, stable and intense continuum beam and therefore all possess some functional flexibility. The rotator/polarizer pair acts as an energy attenuator, necessary in view of the fact that only 2-3  $\mu\text{J}$  of the 1300 nm radiation is necessary to generate stable continuum. The adjustable iris acts as an elementary spatial filter to provide a clean Gaussian beam for generation. Finally, the focusing lens ( $f = 10$  cm) is mounted on a translational stage in order to precisely position the focus for optimal

spectral broadening. White-light continuum generation is brought about by the onset of catastrophic self-focusing within a transparent, condensed medium [48,50]. Although any incident power above the critical power for self-focusing ( $P_{cr}$ ) will eventually induce supercontinuum generation [57], for shorter path length samples ( $\sim$  few mm's) a focusing geometry is necessary to induce the phenomena. The medium chosen for the generation of the WLC is a 2.5 mm thick calcium fluoride (CaF) window. Brodeur and Chin [58] concluded, following an extensive study of the mechanisms behind continuum generation, that the spectral broadening of the supercontinuum scaled as the bandgap of the generation medium. For this reason, we chose CaF which has one of the largest bandgaps ( $E_{gap} = 10.2$  eV) of any transparent medium. This fact, coupled with the observation that the anti-Stokes portion of the supercontinuum is considerably broader than the Stokes fraction [58], explains the how the continuum can span over two octaves, 350-1700 nm, following generation by the near IR radiation at 1300 nm. Unfortunately, CaF does not have a high damage threshold which can be detrimental when working with powers greater than  $P_{cr}$ . To avoid damage of the medium, the CaF plate is continuously rotated during excitation.

Following generation, the divergent continuum possesses a central portion, intense and white to the eye, surrounded by a faint, concentric rainbow pattern. An adjustable iris is used to select only the intense, central portion of the beam. This portion is passed through a dielectric short pass filter such that any remaining 1300 nm radiation is blocked. A focusing lens ( $f = 15$  cm) then images the continuum onto the sample (see following section) such that it is spatially overlapped with the pump beam. Prior to arriving at the sample, a fraction of the WLC probe beam is sampled by a broadband, 50/50 beamsplitter. This fraction of the WLC is exploited as a reference beam which is useful in monitoring the fluctuations of the probe beam. The portion

passing through the sample (i.e. the signal beam) is collected and focused onto the detecting element. Finally, the two polarizers (one after the CaF plate and the other following the final collecting lens) are not used in the transient absorption measurements but in the OKE experiments mentioned above. During the transient absorption measurements the polarizers remain parallel allowing light to go through, however during the OKE experiments they are crossed.

The detection geometry for the pump-probe apparatus has two arrangements. In the first arrangement, a dual fiber input spectrometer is used (SpectraPro 150, Acton Research) to collect and spectrally disperse the WLC probe. This system is coupled to a dual diode array (Princeton Instruments Silicon DPDA 2048 for visible 300-1100nm or Sensors Unlimited InGaAs DPDA 512 for infrared 800-1700 nm) which detects the dispersed probe signal. In the second arrangement, narrowband filters ( $\sim 10$  nm), centered at various wavelengths throughout the spectral range of interest, are inserted in the continuum path and the probe transmission is recorded versus time delay using photodiodes. This arrangement gives a better signal to noise ratio ( $S/N \sim 200$ ) than the diode array geometry because the photodiodes can account for the continuum fluctuations on a shot-to-shot basis unlike the diode array. However, since the nonlinear spectrum must be formed in a piecewise fashion, this geometry requires significantly more time to acquire data.

### *3.3.2.2 Off-Axis Focusing Geometry*

In our pump-probe geometry, there are two conditions which must be addressed: (1) the ratio between the pump and probe irradiances at the sample plane should be on the order of 100

to 1, and (2) the ratio between their respective beam sizes at the sample should be at least 3 to 1. The first condition is crucial to insure that the probe beam is indeed “weak” meaning that it does not induce any nonlinearities within the system itself. The second condition must be met so that the probe beam “sees” uniform illumination by the pump beam. If this condition is not met, it becomes necessary to spatially integrate over the pump beam in order to determine the excitation irradiance. This can greatly complicate the data analysis. Both of these conditions are predicated on a tight focusing geometry for the probe beam.

The box in Figure 3.4 denotes the focusing geometry we used for the WLC probe beam. An on-axis geometry is shown where the focusing is accomplished via a positive achromatic lens. This geometry is convenient and it avoids off-axis aberrations such as astigmatism (i.e. orthogonal planes focus at different positions along the optical axis) which can greatly distort the beam profile at focus. However, this layout still suffers from severe chromatic aberration (i.e. different colors focus at different longitudinal positions along the optical axis) despite the use of an achromat for focusing. Table 3.1 illustrates this effect. Here, the beam profiles of certain wavelengths of the WLC in the sample plane are quantified. This is accomplished by placing narrowband filters ( $\sim 10$  nm) centered at certain wavelengths directly after the WLC is generated in the CaF plate. The beam sizes, whose  $HW1/e$  values are given in microns, are shown for both the horizontal (x) and vertical (y) directions. The effect of chromatic aberration is quite evident as the beam size in the sample plane nearly triples when going from 600 to 900 nm. The only wavelength for which the focusing is optimized is 600 nm which has a beam size of 100  $\mu\text{m}$ . However, the sample plane is placed here as a compromise for the visible region of the WLC. In order to satisfy the condition of uniform illumination of the pump beam, its size could certainly be made quite large (e.g.  $\sim 800$   $\mu\text{m}$ ). However, this may not allow sufficient pump



intensity to induce a nonlinearity in the sample and moreover may not satisfy the condition for a “weak” probe beam. Furthermore, the condition is only worsened as one approaches the near IR.

Table 3.1: Beam sizes in the sample plane for various wavelengths of the WLC probe beam using the on-axis geometry.

$\lambda$	$w_x$ (HW <sup>1/e</sup> )	$w_y$ (HW <sup>1/e</sup> )
440nm	<200 $\mu$ m	<200 $\mu$ m
600nm	100 $\mu$ m	100 $\mu$ m
750nm	~ 200 $\mu$ m	~ 200 $\mu$ m
900nm	300 $\mu$ m	350 $\mu$ m
1200nm	~ 250 $\mu$ m	200 $\mu$ m

In order to rectify this situation, a true achromatic geometry must be constructed. This is accomplished through the use of reflective optics. Unfortunately, these optics must be used in an off-axis configuration which will assuredly induce a significant amount of astigmatism if not properly accounted for. The off-axis reflective arrangement which we use is shown in Figure 3.5. In this set-up, two concave mirrors, CM1 and CM2 ( $R_1 = R_2 = 300$  mm), are used off-axis in orthogonal planes in order to compensate for astigmatism [59]. This is illustrated by showing the geometry from the top (Figure 3.5a) as well as from the side (Figure 3.5b). The probe beam behaves as follows: the light diverges from the CaF plate and is collimated by CM1. CM1 is off-axis in the horizontal plane such that astigmatism is solely present in this plane. The collimated beam is reflected off of a flat mirror (M1) and sent to the left and upwards. It is sent left to avoid optics of the pump beam and sent upward to arrive at a second flat mirror (M2) such

that it reflects only in the vertical plane. Although it is not shown, the short pass dielectric filter found in the on-axis geometry is also present within this portion of the optical beam path. Next, the collimated beam is sent downward to CM2 which is off-axis in the vertical plane so that astigmatism is, again, solely present in this plane. CM2 then focuses the beam onto the sample. The initial beam size is kept relatively small with the use of the iris in order to minimize spherical aberration. The beams are then centered on all optical elements in this system to minimize off-axis aberrations. Moreover, the angles (shown in the insets) for which the concave mirrors reflect off-axis are small ( $\sim 10$  degrees) to further reduce these aberrations. And finally the two mirrors are used off-axis in orthogonal planes in order to minimize the total astigmatism present in the set-up.

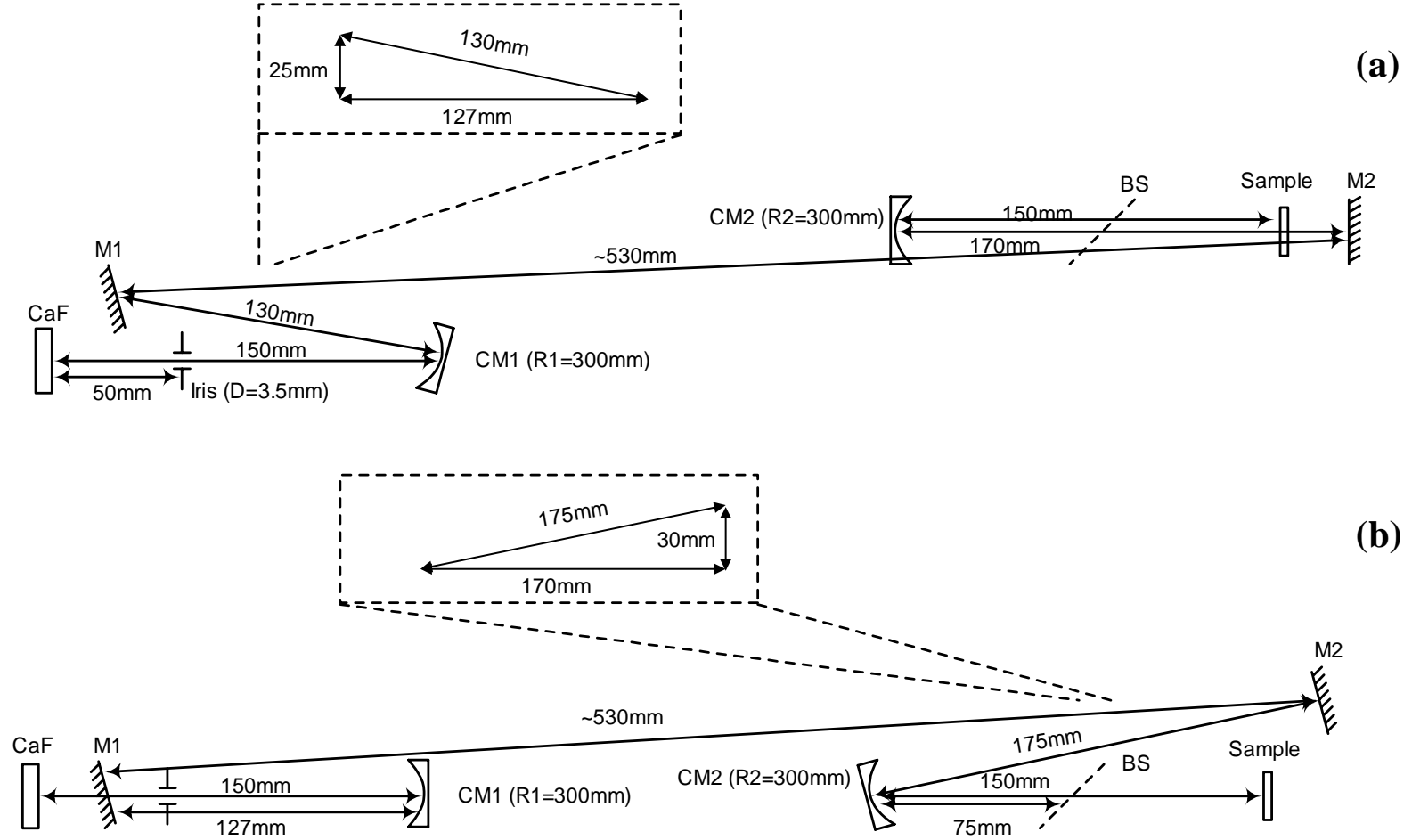


Figure 3.5: Off-axis geometry for achromatic focusing of the WLC onto the sample plane. (a) Top view. (b) Side view. The insets show the dimensions of the off-axis arrangements.

The results of the off-axis arrangement are summarized in Table 3.2. Table 3.2a shows that the beam sizes in the sample plane are very nearly constant for all wavelengths of the WLC verifying that the off-axis geometry is truly achromatic. Furthermore, the focused beam sizes are nearly four times smaller than for the on-axis geometry. This is most likely due to the minimization of the spherical aberration in the system. Table 3.2b gives the beam sizes for  $\lambda = 600$  nm as it passes through the sample plane (denoted by 0  $\mu\text{m}$ ). There is still a slight astigmatism within the optical set-up but it is, for the most part, negligible. The reduction of the probe beam allows us to achieve higher pump irradiances through tighter focusing without sacrificing the conditions necessary for the pump-probe geometry. However, one should take care, with such small dimensions, that the probe beam itself does not induce nonlinearities. For this reason, the sample plane is placed a few millimeters away from the actual focal plane such that the probe beam size is  $\sim 70$   $\mu\text{m}$ . Finally, in order to insure proper collection of the probe beam (e.g. when using the fiber-coupled spectrometer), reflective optics have also replaced the collection lenses shown in Figure 3.4. In this case, only one concave mirror is utilized since minimization of astigmatism is not as crucial for collection.

Table 3.2: Beam sizes of the WLC probe beam for the off-axis geometry. (a) Sizes in the sample plane for various wavelengths of the WLC. (b) Sizes for  $\lambda = 600$  nm for various positions along the optical axis.

(a)			(b)		
$\lambda$	$w_x$ (HW <sup>1/e</sup> )	$w_y$ (HW <sup>1/e</sup> )	Pos	$w_x$ (HW <sup>1/e</sup> )	$w_y$ (HW <sup>1/e</sup> )
440nm	~25 $\mu$ m	~25 $\mu$ m	+1000 $\mu$ m	40 $\mu$ m	10 $\mu$ m
600nm	~25 $\mu$ m	~25 $\mu$ m	0 $\mu$ m	30 $\mu$ m	20 $\mu$ m
750nm	~25 $\mu$ m	~25 $\mu$ m	-1000 $\mu$ m	20 $\mu$ m	30 $\mu$ m
900nm	~25 $\mu$ m	~25 $\mu$ m	-2000 $\mu$ m	10 $\mu$ m	40 $\mu$ m
1200nm	~25 $\mu$ m	~25 $\mu$ m			

### 3.3.3 Cross-Phase Modulation

Transient absorption spectroscopy using WLC can suffer from a number of unwanted artifacts which may obscure the desired absorption data. Some of the most problematic side effects originate from the solvent or the fused silica windows of the sample cell used to hold the solution. These are generally exacerbated by the use of high pump irradiances (e.g. 10-500 GW/cm<sup>2</sup>), spectrally broad probe pulses (e.g. WLC from 300-1100 nm), and a sensitive detection system [60]. The artifact which is most germane to the current spectroscopy experiment involves the spectral change induced in the weak WLC probe pulse by the strong pump pulse via cross-phase modulation (XPM) [61]. XPM involves a time-dependent modulation of the refractive index of the medium by the intense pump pulse. Provided the pump and probe pulses are overlapped in time and space, the probe beam will experience this modulation which can be rewritten as a time-dependent phase term:

$$\Delta\phi^{\text{XPM}}(z, t) = 2n_2 I(z, t) k_o z . \quad 3.5$$

Here,  $k_o$  is the wave vector of the probe beam,  $z$  is the propagation distance, and the time-dependent refractive index is given by the product of the pump pulse irradiance,  $I(z, t)$ , and the nonlinear refractive index,  $n_2$ . Since a time-dependent phase manifests itself as a frequency change, the probe pulse will experience a spectral change given by:

$$\delta\omega(t) = -\frac{\partial\Delta\phi^{\text{XPM}}}{\partial t} = -\frac{\partial}{\partial t} I(0, t) 2n_2 k_o z \quad 3.6$$

where the pump irradiance is assumed to be constant during propagation through the sample. Since the magnitude of the spectral change is proportional to the derivative of the pump pulse profile, if one assumes a Gaussian pulse shape, the probe will experience the greatest spectral shift when it is overlapped with either the leading or trailing edge of the pump pulse. This spectral change of the probe should be detectable provided the probe is spectrally dispersed after the sample. This is precisely the case for our WLC spectroscopy measurement using the fiber coupled spectrometer and dual diode array. Spectral resolution is critical because there is no net energy transfer either into or away from the probe but rather the total energy remains constant and is merely redistributed over different frequencies [61]. Therefore, if one were to monitor a specific frequency, one would observe a time-dependent change in probe transmittance due to this energy redistribution. This could certainly obscure the time-dependent probe transmittance changes which are caused by 2PA. Incidentally, although the second detection arrangement for our transient spectroscopy set-up involving narrowband filters and photodiodes does not use a dispersive element, the fact that only a narrow spectral range is being monitored insures that this XPM artifact will still be present.

To illustrate the effect of XPM in transient absorption measurements Figure 3.6a shows a plot of a typical transient absorption signal for a two-photon absorbing organic molecule dissolved in solution. This curve was acquired from our pump-probe WLC spectroscopy set-up (using the narrowband filter/diode arrangement). Here, the normalized transmittance of the probe beam, at a particular wavelength, is plotted versus the temporal delay between the pump and the probe. The curve shows nonlinear loss only during the time when the two pulses are overlapped, indicative of an instantaneous process such as 2PA. However, immediately before and after the transient absorption signal, there are slight increases in the probe transmittance, unexplainable assuming 2PA is the only mechanism present. In Figure 3.6b the same pump-probe delay curve was taken except the sample is now only the solvent and the fused silica cuvette which held the solution. Therefore, there is no nonlinear chromophore present. The positive changes in transmittance are still present and an additional artifact which mimics 2PA is present around the zero delay point. This XPM artifact can be explained as follows: Assume that the probe wavelength being monitored is  $\lambda_0$ . When the probe pulse overlaps with either the leading or trailing edge of the pump pulse, its spectrum experiences the largest shift (see Equation 3.5) and therefore energy is shifted away from  $\lambda_0$  resulting in a loss of transmittance at that wavelength.<sup>3</sup> Since we are dealing with a chirped (temporal dispersion of frequency) WLC, wavelengths both longer than and shorter than  $\lambda_0$  will have their spectra either blue-shifted or red-shifted, respectively. This will result in energy moving toward our central wavelength and produce positive changes in transmittance. This process is responsible for the structures seen

---

<sup>3</sup> This would imply that perfect overlap between the two pulses (i.e. zero delay) would induce no spectral change. However, this simple explanation ignores the finite bandwidth of the probe pulse centered at  $\lambda_0$  and more importantly the other pulses around this wavelength. They, too, will contribute to the apparent loss observed at zero delay.

both before and after zero delay in Figure 3.6. It should be noted that the group-velocity mismatch between the pump and the probe pulses results in a diminished interaction length and decreased signal strength for XPM similar to the effect described above for 2PA. This effect is discussed in detail in Reference 61.

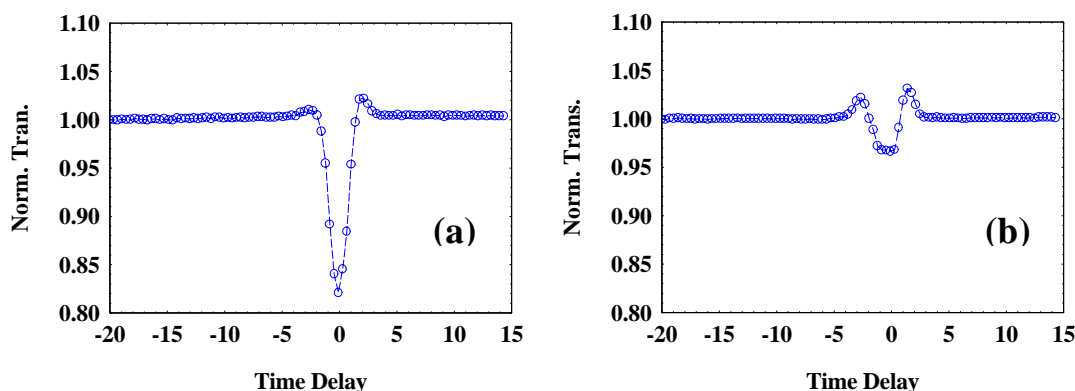


Figure 3.6: Typical pump-probe time delay scans acquired using our WLC spectroscopy set-up. (a) Shows a transient absorption signal caused by 2PA and XPM mechanisms. (b) Shows a signal generated by pure XPM.

Given that the artifact of the XPM signal at zero delay quite effectively mimics 2PA, we must eliminate the effect or it will artificially enhance the 2PA cross-section extracted from the experimental data and produce erroneous results. Although, the XPM artifact due to the solvent and the glass cuvette only shows a  $\sim 3\%$  signal, this can be quite substantial for samples with small nonlinearities. Lorenc *et al.* [60] present a simple correction procedure for calculating artifacts-free transient absorption signals. Based on the fact that the contribution from each signal, both 2PA and XPM, is linearly dependent on the pump irradiance, a simple subtraction of the two signals can be made assuming the same pump irradiance is used when measuring them both. In addition, the authors point out additional artifacts, such as



Stimulated Raman Scattering (see Section 2.1), which can be corrected in a similar manner. Although the correction is simple, it still requires two measurements to acquire proper 2PA data. Ideally, one would like to completely eliminate the XPM artifact. This is, of course, not possible for solution samples; however, the effect can be minimized. Figure 3.7 shows XPM signals for different sample configurations taken under identical conditions. The sample we used for curve (a) was water contained inside a typical 1 mm path length cuvette used for spectroscopy. The windows of these cuvettes are made of fused silica and are about 1.25 mm thick. The strength of the XPM signal at zero delay is ~6%. Subsequently, we used the empty cuvette for curve (b) and found that the windows of the sample holder contributed almost 4% to the total signal. Noting that the strength of the XPM signal is proportional to the sample thickness (see Equation 3.5), we constructed a homemade sample holder of 1 mm path length consisting of windows constructed from microscope cover slips. These disks are also made of fused silica but have thicknesses of only 0.17 mm. Once again, XPM signals were measured for the sample holder including the water, curve (c), and without it, curve (d). As expected, curve (d) shows no appreciable signal, indicating that the cover slips make no contribution to the XPM signal in (c). The artifact due to the water remained at 2%. Although, it is not possible to get rid of the solvent completely, one could certainly minimize its path length and virtually eliminate the XPM artifact for transient absorption spectroscopy. It should be noted that we have purposely ignored the contribution of the solute (i.e. organic compound) in the above argument with good reason. Even with highly concentrated solutions (i.e.  $10^{-2}$  M), the number of solvent molecules is orders of magnitude larger than the number of solute molecules making their contribution quite negligible.

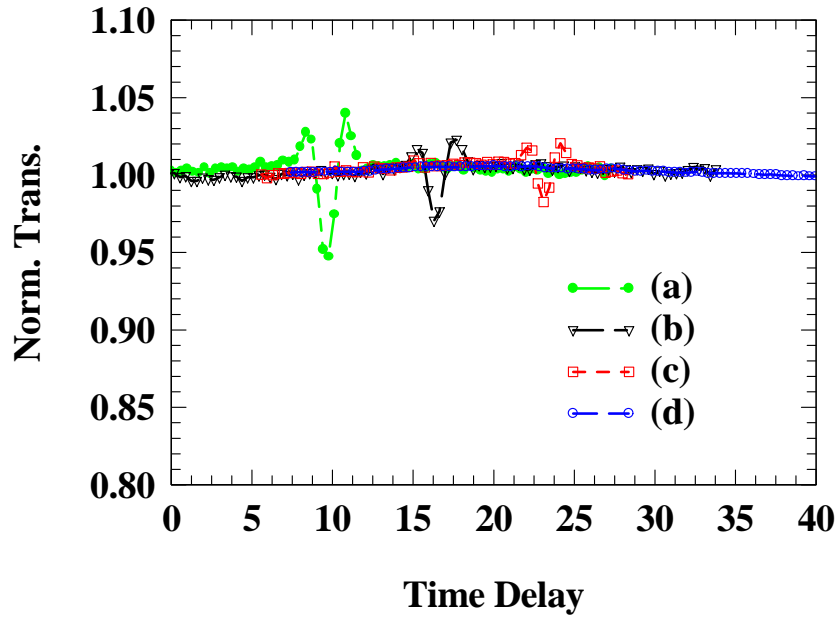


Figure 3.7: Pump-probe time delay scans exhibiting XPM signals acquired for various sample configurations. (a) Standard cuvette with water. (b) Standard cuvette. (c) Modified cuvette with water. (d) Modified cuvette.

### 3.4 Z-Scan

The final method of nonlinear characterization used in this study is the Z-scan technique [62,63]. This is a sensitive tool for measuring nonlinear changes in index and absorption. The method makes use of a single beam and therefore will help determine the degenerate 2PA cross-section ( $\delta$ ) of a sample, much like the 2PF technique described above. In this experiment, the transmittance of a focused Gaussian beam through a nonlinear medium is monitored as a function of the sample position  $z$  measured with respect to the beam's waist. As the sample is translated along the axis of the focused beam, it passes through its waist where the irradiance is maximized. Provided the sample exhibits nonlinear absorption, the transmittance of the beam at this point should be a minimum. This is verified in Figure 3.6 which shows a typical Z-scan for

two-photon absorption. The graph plots normalized transmission versus the sample position and shows a curve symmetric about the minimum in transmittance which occurs at  $z = 0$ , or the beam waist. Fitting this transmission curve using the formulae found in Reference 62 allows  $\delta$  to be extracted.<sup>4</sup> By repeating this experiment for various pump wavelengths, determination of the full degenerate 2PA spectrum can be made.

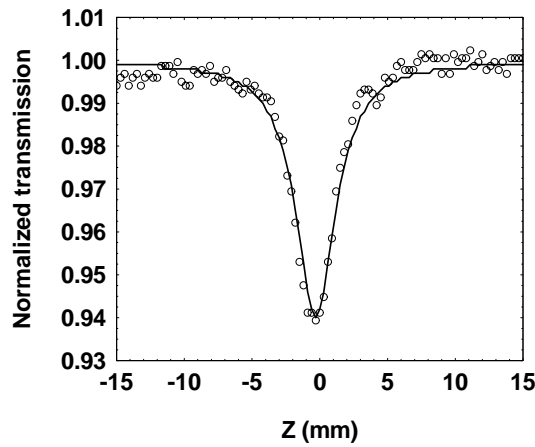


Figure 3.8: Typical Z-scan curve acquired from a two-photon absorbing medium.

It should be recognized that since this method is sensitive to all forms of nonlinear absorption, the underlying physical phenomena can not be unambiguously determined without the use of other experiments (e.g. time-resolved experiments). However, determining the relationship between input irradiance ( $I$ ) and the maximum change in the normalized transmittance ( $\Delta T$ ) can certainly give support as to the suspected process. Finally, although the simplicity of the technique and its interpretation makes Z-scan straightforward to implement, it is

---

<sup>4</sup> The Z-scan method as described in References 62 and 63 actually calculates the degenerate 2PA coefficient,  $\beta$ . In

quite time consuming when it comes to the task of characterizing an entire 2PA spectrum. First of all, the method is inherently single beam in nature and therefore, unlike the WLC method, each wavelength must be measured separately. Secondly, the technique is non-referential which requires precise determination of the pump irradiance for each wavelength; this is in contrast to the 2PF method which relies on reference standards. For these reasons, the Z-scan technique, in this study, is mainly used as a self-consistency check against the other spectroscopic methods. Once the shape of the nonlinear spectrum is known, a Z-scan is acquired at a particular wavelength (usually at the peak of the spectrum) as a reference. The samples used in this study are the same as those used in the WLC spectroscopy technique: solutions contained within 1 mm path length glass cuvettes with concentrations on the order of  $10^{-2}$  M. Also, like the pump-probe technique, the errors associated with this method are: absolute errors of  $\pm 15\%$  and relative errors of  $\pm 6\%$ . Once again, the largest source of uncertainty comes from the calculation of the irradiance of the excitation beam.

### **3.5 Quantum-Chemical Methodology**

For the reasons discussed in Section 2.2, the approach we have chosen to employ in the theoretical determination of the 2PA cross-sections for the fluorene derivatives in this study is the perturbative Sum-Over-States approach. This involves the calculation of the electronic transition energies as well as the state and transition dipole moments of the molecules under investigation. All of these calculations were performed in Dr. Jean-Luc Bredas' group in the

---

order to convert to the degenerate 2PA cross-section,  $\delta$ , one must use Equation A.12.

School of Chemistry and Biochemistry at the Georgia Institute of Technology. The following is a description of the quantum-chemical methodology employed in these calculations.

The molecular ground-state geometries were optimized using the semiempirical AM1 Hamiltonian [64]. All calculations were performed on isolated molecules, thus neglecting solvent effects. This approximation seems reasonable because hexane was chosen as the solvent in the experiments for the specific reason of minimizing solvent effects. The excited-state energies, state- and transition-dipole moments were obtained by performing a highly correlated calculation where the INDO [65] Hamiltonian is coupled to a Multi Reference Determinant Single and Double Configuration Interaction technique (MRD-CI)<sup>5</sup> [66] using the Mataga-Nishimoto potential [67] to express the Coulomb repulsion term. Alternatively, for better convergence with the experimental results, the calculations performed on molecules **1** and **4** used the Ohno-Klopman potential [68].

The contributions from the excited states can then either be truncated after only a few states to be used in the essential states analysis described in Section 2.3; alternatively, to determine the fully-converged results for the 2PA cross-sections we have included the 300 lowest-lying excited states into the expression for the third-order molecular polarizability  $\gamma(-\omega_1; \omega_1, -\omega_2, \omega_2)$  given by SOS expression defined by Equation 2.7. For degenerate 2PA results, the two frequencies entering Equation 2.7 are equal ( $\omega_1 = \omega_2$ ). The value of the damping

---

<sup>5</sup> As reference determinants in the MRD-CI calculations we chose the determinants most strongly contributing to a single and double CI description of the dominant one- and two-photon states. These are: (i) the SCF determinant; (ii) a determinant in which an electron has been promoted from the HOMO to the LUMO; (iii) one in which an electron has been excited from the HOMO-1 to the LUMO; (iv) the doubly excited determinant in which both electrons are excited from the HOMO to the LUMO, and (v) for molecule 1 the HOMO to LUMO+1 and for molecule 2 the HOMO to LUMO+5 determinants. The CI active space for the single excitations included the 24 highest occupied and 24 lowest unoccupied orbitals in molecule 1; for molecule 2, it was increased to  $28 \times 28$  orbitals due to the

factor,  $\Gamma$ , was taken to be 0.1 eV for all transitions in accordance with previous publications [23,37]. Finally, these results were used in conjunction with Equation 2.5 to determine the values for the 2PA cross-section  $\delta$ .

---

larger number of  $\pi$ -electrons. For the higher excitations, in all cases 5 occupied and 5 unoccupied orbitals have been considered.

## CHAPTER 4: FLUORENE MOLECULES

The methodologies detailed in the previous Chapter provide a strong framework for a comprehensive study of the optical properties for any set of organic molecules. The molecules specifically targeted by this dissertation include a group of fluorene derivatives. The following Chapter details the structures and the corresponding linear optical properties of these derivatives. Section 4.1 concentrates on the fluorene chromophore which is the central base structure for all of the subsequent molecules characterized in this study. The rationale for choosing this chromophore is discussed. The subsequent Section reveals the strategy for altering the chemical structures of the derivatives in order to facilitate the investigation of chemical structure – NLO property relationships. The fluorene derivatives and their varying structural motifs are also presented. The final Section catalogues the linear spectroscopic properties derived from the experimental techniques described in Section 3.1. Some of the possible ramifications of these results on the two-photon absorbing capabilities of these molecules are also mentioned.

### 4.1 Fluorene Chromophore

Each compound to be studied has a common base structure, the fluorene chromophore. This is shown in Figure 4.1.

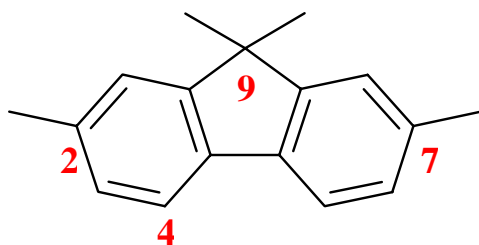


Figure 4.1: The base fluorene chromophore. Positions 2, 4, 7 and 9 are marked for reference.

The benefits of this base structure are four-fold: First, the fluorene chromophore is an aromatic, or  $\pi$ -conjugated, compound. This is a result of the cyclic conjugated nature of the two benzene constituents within the chromophore. Each benzene structure possesses six  $\pi$  electrons which are completely delocalized around the ring. As mentioned in Section 1.1, this electron delocalization can give rise to a large molecular polarizability which promises strong nonlinear interaction upon excitation. Secondly, the rigid ring system which constitutes the fluorene core serves as both a thermal and photochemically stable system. Although organic molecules with strong nonlinear properties are at a premium, if the system cannot withstand the intense radiation which nonlinear excitation requires, the compounds' optical properties may very well degrade along with their utility. One and two-photon photodegradation studies have been performed to investigate the robustness of this stability in these fluorene derivatives. Initial results indicate that photostability under two-photon excitation conditions is nearly identical to that found under similar linear excitation conditions [69]. This bodes well considering the resiliency of these compounds during one-photon excitation (found in Reference 69). The third advantage of the fluorene chromophore involves its highly efficient fluorescent nature. As a result, a significant portion of the molecules investigated in this study possess large quantum yields, in fact, some have yields approaching unity (see Section 4.3). Consequently, derivatives of this chromophore, provided



they are good two-photon absorbers, are strong candidates for use in two-photon fluorescence microscopy.

Finally, the aromatic core of the fluorene chromophore has a high degree of functionality. This means that there are several potential sites where one can append substituent groups onto the base molecule in order to alter its structural properties. The base chromophore may be functionalized, or chemically appended, on the 2, 4, 7 and/or 9 positions of the molecule. These positions are marked for reference in Figure 4.1. Functionalization of position 9 typically allows for the possibility of increased solubility by appending alkane chains (i.e.  $C_{10}H_{21}$  or  $C_2H_5$ ) to the chromophore. This aspect is particularly crucial given the highly concentrated solutions (i.e.,  $10^{-4}$  to  $10^{-2}$  M) used during characterization for the generation of sufficient nonlinear signals. However, concurrent with this requirement is the concern that these solutions may suffer from aggregation-type effects (e.g., dimer formation) which may interfere with the measurements. In order to confirm that this was not the case, we carried out 2PF spectroscopy measurements (see Section 3.2) with sample solutions of varying concentrations (i.e.,  $10^{-5}$  M up to  $10^{-2}$  M). The discrepancies between the 2PA spectra acquired with the more dilute samples versus the more highly concentrated ones were minor. This fact, along with an independent linear absorption experiment verifying that  $10^{-5}$  M solutions do not suffer from aggregation effects, confirmed that aggregation was indeed negligible. This is a direct consequence of the solubility afforded by the appended alkane chains. Above all, functionalization of the 2 and 7 positions, and to a certain extent position 4, proffers the greatest benefits. These positions provide the means to generate different chemical archetypes by appending various functional groups to the fluorene chromophore. This point will be discussed in detail in the following Section. Hence, the

fluorene chromophore has many benefits for use as a molecular backbone, the most important of which is its functionality.

## 4.2 Fluorene Derivatives

Given the functionality afforded by positions 2, 4 and 7 of the fluorene molecule (Figure 4.1), various fluorene derivatives can be designed. Through prudent modification of the chemical structure, a number of different structural motifs can be systematically constructed. The general architecture for our fluorene derivatives is summarized in Figure 4.2. On the left side of the Figure, the fluorene base chromophore is shown with potential substituent groups appended via the 2 and 7 positions (position 4 is used less frequently and will not be discussed here).

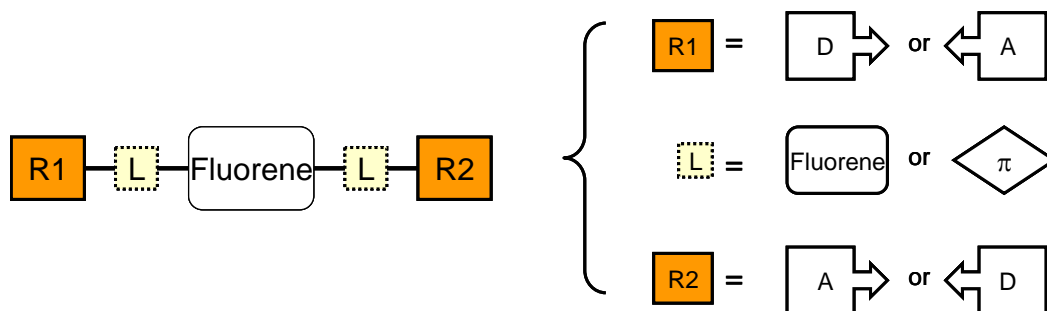
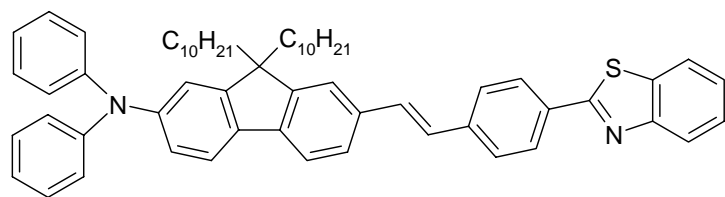
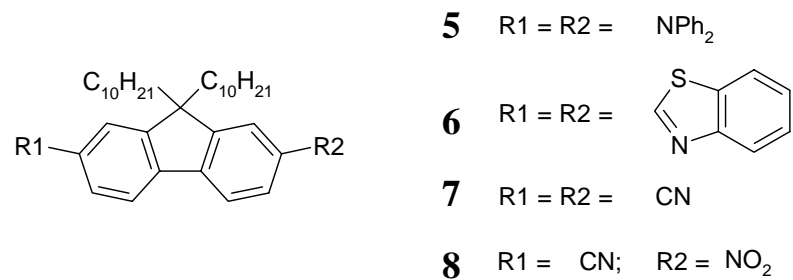
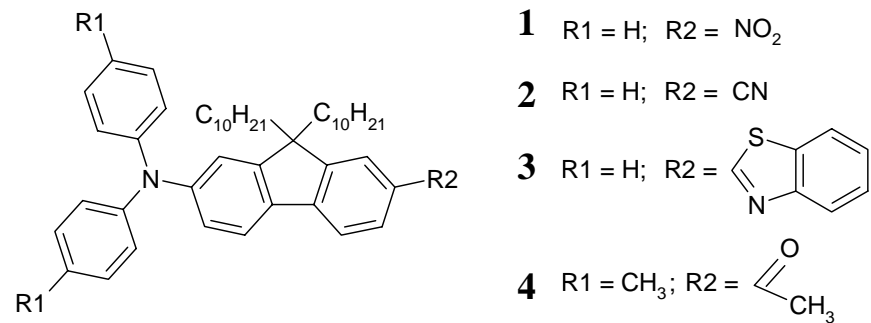
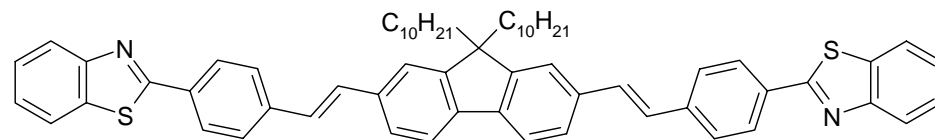


Figure 4.2: General architecture for the fluorene derivatives. The possible substituent groups are shown on the right side of the figure. R1 and R2 denote the terminal groups and L denotes a linking group.

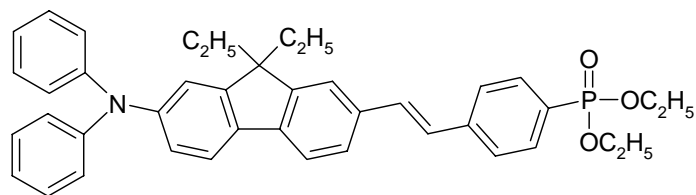
R1 and R2 denote the terminal groups of the derivative and L represents possible linking groups which may be added. The possible substituents are pictorially represented on the right side of the Figure. The terminal groups consist of electron active moieties, that is, groups with either low or high electron affinities. These are denoted by either a donor (D) or an acceptor (A), respectively. Appropriately, they are represented by boxes with arrows illustrating the direction in which electrons are most likely to flow based on that affinity. Appending these electron active end groups directly to positions 2 and 7 allows the creation of the following motifs: (1) Donor –  $\pi$ -conjugated core – Donor (D- $\pi$ -D), (2) Acceptor –  $\pi$ -conjugated core – Acceptor (A- $\pi$ -A), or (3) Donor –  $\pi$ -conjugated core – Acceptor (D- $\pi$ -A). The strengths of these electron donating/withdrawing moieties may also be controlled thereby broadening the scope of these potential archetypes. In addition to this, linking groups (L) may be incorporated into the derivatives prior to the terminal groups. These can consist of either additional fluorene chromophore units or some other  $\pi$ -conjugated sub-structure (e.g., vinyl or styryl structures). Functionalization, in this manner, provides the opportunity to extend the  $\pi$ -conjugated backbone of the molecule. This gives rise to the following possible motifs: A- $\pi$ - $\pi$ -A, D- $\pi$ - $\pi$ -D, D- $\pi$ - $\pi$ -A, D- $\pi$ - $\pi$ - $\pi$ -A, etc. Therefore, modification of the base chromophore is accomplished by influencing the electron accepting and donating properties of the system as well as possibly extending the conjugation length of the molecule.



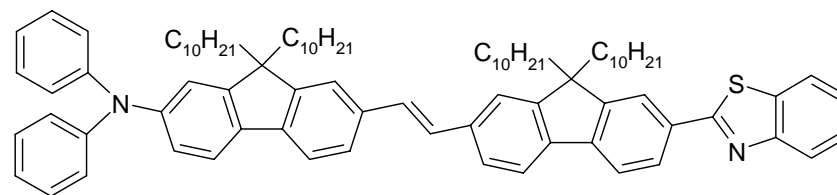
**9**



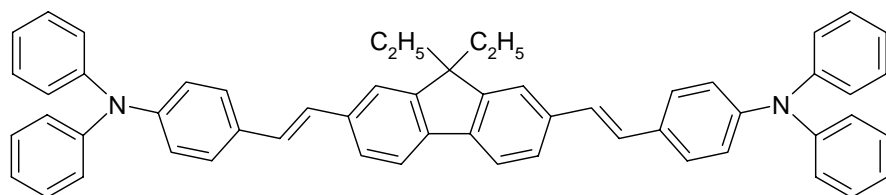
**12**



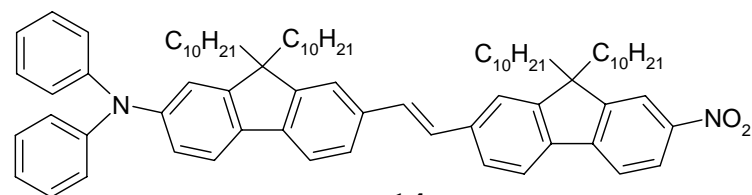
**10**



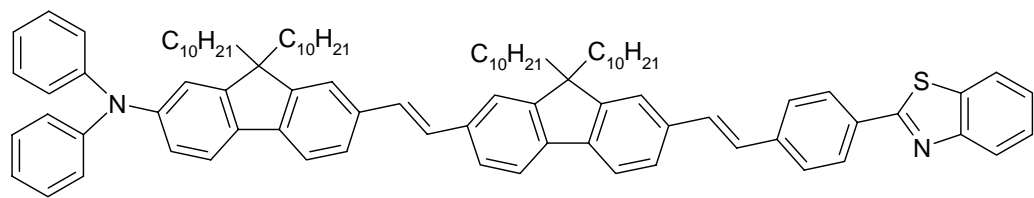
**13**



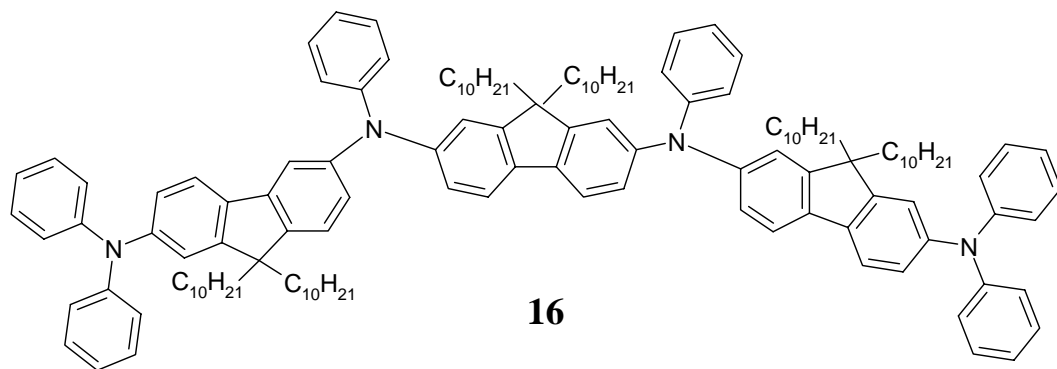
**11**



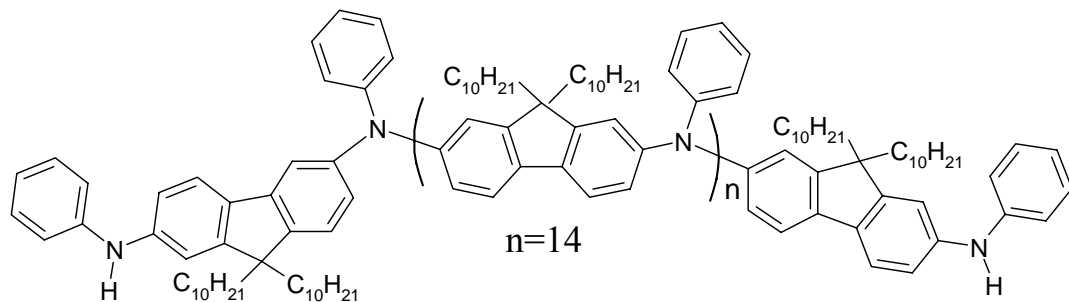
**14**



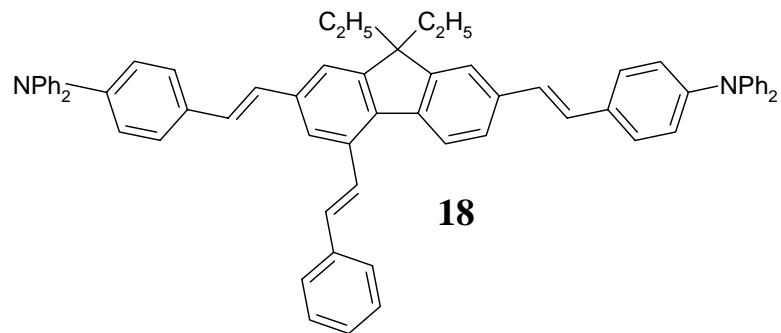
**15**



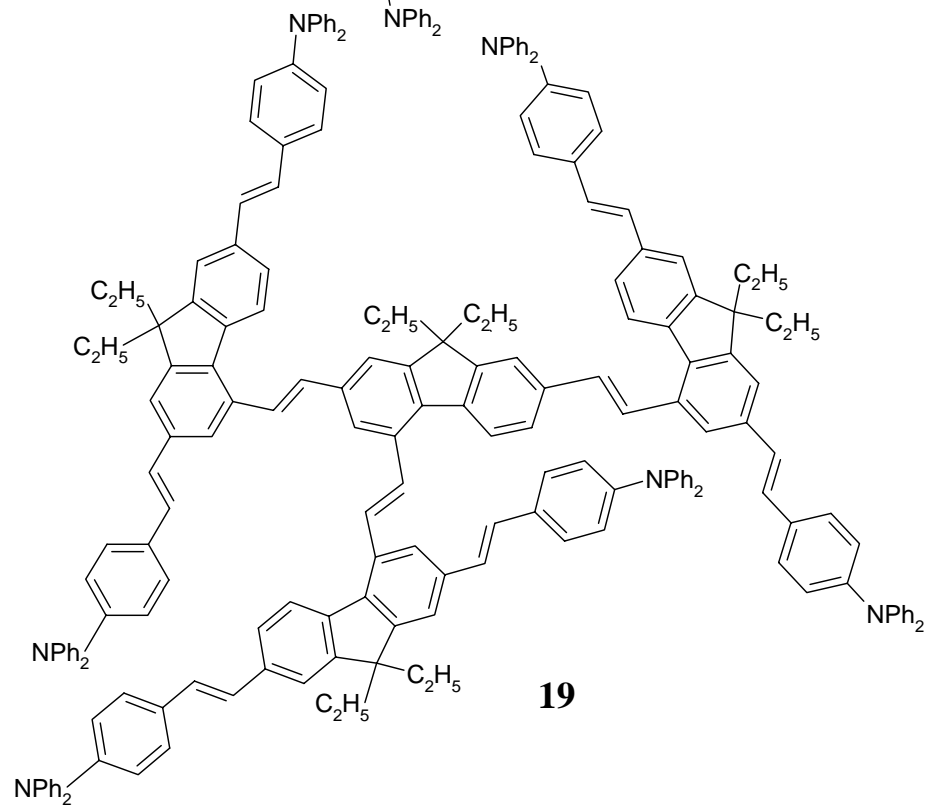
**16**



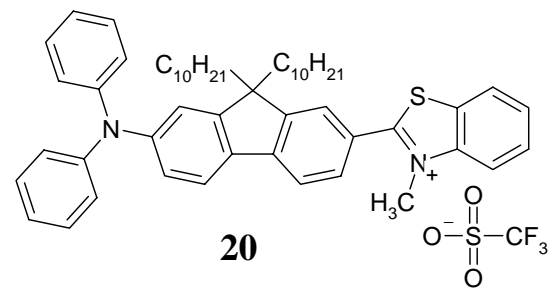
**17**



**18**

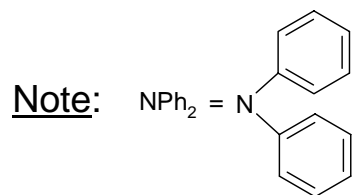


**19**



**20**

Figure 4.3: Chemical structures of fluorene derivatives.



The fluorenyl derivatives investigated in this study are shown in Figure 4.3. All of these molecules were synthesized in Dr. Kevin Belfield's group in the Chemistry Department at the University of Central Florida. Their synthesis methodologies will be referenced during the short description of each molecule given below. The synthesis strategies for those molecules without individual references can be found in the PhD Dissertation of Morales [70]. The proper chemical nomenclature for these molecules is given in Appendix C; however, for the sake of brevity, they will henceforth be referred to by their appropriate numbers as assigned in Figure 4.3. Compounds **1-4** (**1** and **3** in Reference 71) possess a dipolar D- $\pi$ -A type geometry where the strength of the terminal accepting group is varied. In contrast, the following three compounds (**5** in [71], **6** in [72] and [73], **7** in [74]) possess a symmetric structure along the main backbone of the molecule. The archetypes represented are D- $\pi$ -D and A- $\pi$ -A. Molecule **8**, on the other hand, is slightly different, possessing two acceptor end groups of disparate strengths. The two subsequent derivatives (**9** in [72], **10** in [75]) are dipolar molecules with their conjugated backbones extended via a styryl bridge. Analogously, compounds **11** and **12** (**11** in [76], **12** in [72]) also benefit from this bridge structure. However, the bridges are situated on either side of the fluorene chromophore symmetrically end-capped with either a donor or acceptor group. Molecules **13**, **14** and **15** are dipolar systems with their conjugated backbones supplemented by additional fluorene chromophores which are connected via vinyl chains. In addition, **15** possesses a styryl unit along its backbone. Compounds **16** and **17** (**16** in [77], **17** in [78]) are symmetrical diphenylamino fluorene derivatives with **16** being an oligomeric version of molecule **5** and **17** a longer polymeric version. Derivatives **18** and **19** (both in [76]) illustrate the possibility of functionalizing the fluorene chromophore on position 4 (see Figure 4.1). Compound **18** thereby strongly resembles the structure of **11** with the distinction of an additional

diphenylamine end-capped styryl bridge protruding from position 4. This structure deviates from the “linear” type molecules described prior to it, exhibiting a more nearly two-dimensional planar geometry. Compound **19** further accentuates this topology by appending three separate sub-structures (i.e., compound **11**) on its three extended branches. Finally, molecule **20** [79] is a methylated salt, a direct analog of the third molecule in this series. This version of the compound is designed to possess a red-shifted linear absorption spectrum, with respect to **3**, in the hopes of benefiting from resonance enhancement via the first excited state (see Section 2.4.2).

### **4.3 Linear Spectroscopy**

In this Section, the linear spectroscopic characterization of the fluorene derivatives, based on the experimental procedures outlined in Section 3.1, is presented. A significant portion of these measurements have been performed in Dr. Kevin Belfield’s group. Much of the spectral data can be found in References 40, 41, 70, and 77. Therefore, only a summary of the spectral characteristics will be offered here. The normalized absorption (denoted by “(a)”) and steady-state fluorescence spectra (denoted by “(b)”) are shown in Figures 4.4-4.9 (except for molecule **20** whose information will be presented in Section 5.6). The spectra are plotted versus wavelength, in nm, on the lower abscissa and wavelength converted to energy, in eV, on the upper abscissa. The energy values are given specifically to compare the linear and 2PA spectra in the following Chapter. It should be noted that all linear and nonlinear measurements were to be carried out on solutions of these compounds in the nonpolar solvent hexane (with the exception of Section 5.2.2 where the effects of solvism on a dipolar compound are investigated

specifically). This solvent was chosen to avoid solute-solvent interactions thereby making the analyses, both experimental and quantum-chemical, more straightforward. However, compounds **11**, **18**, and **19** were not sufficiently soluble in hexane given the high concentrations necessary for the nonlinear measurements. Therefore, another nonpolar (i.e., non-interacting) solvent, cyclohexane, was substituted. Compounds **12** and **20** also presented solubility issues. Unfortunately, it was necessary to dissolve these molecules in polar solvents, methylene chloride and tetrahydrofuran, respectively, to achieve sufficient concentrations.

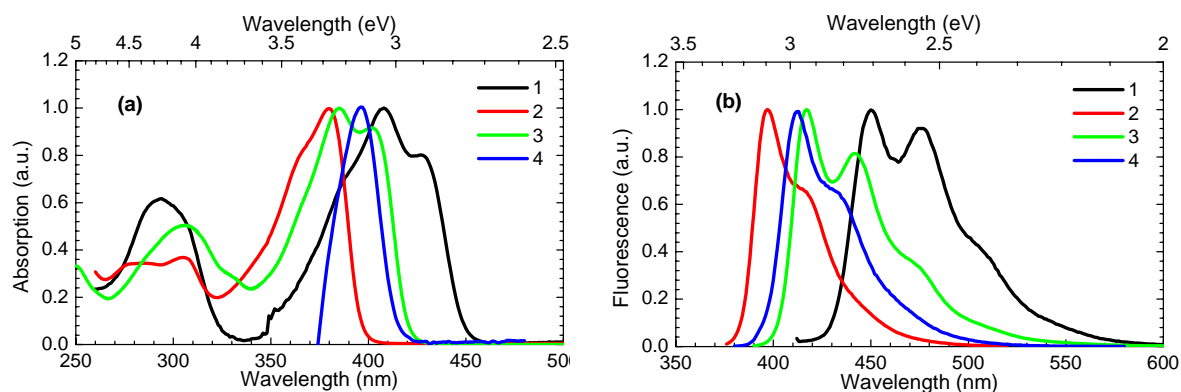


Figure 4.4: Absorption (a) and steady-state fluorescence (b) spectra for molecules **1-4** in hexane.

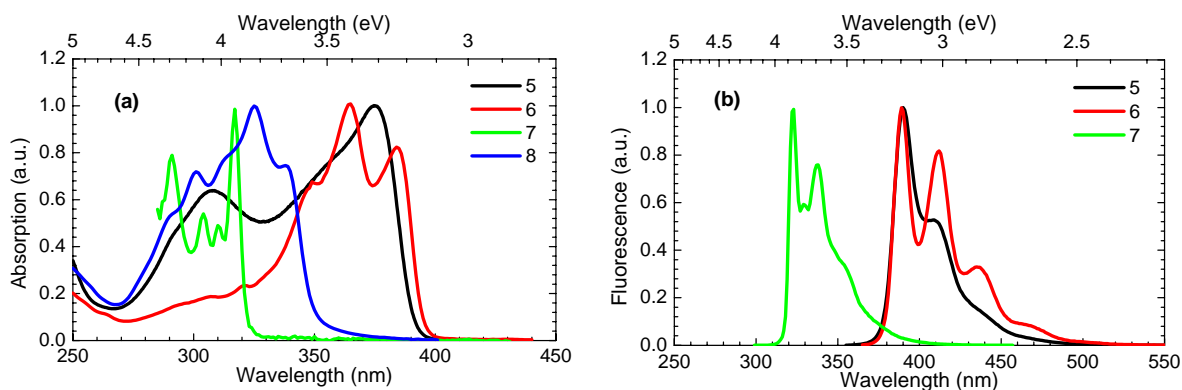


Figure 4.5: Absorption (a) and steady-state fluorescence (b) spectra for molecules **5-8** in hexane. Molecule **8** is non-fluorescent.



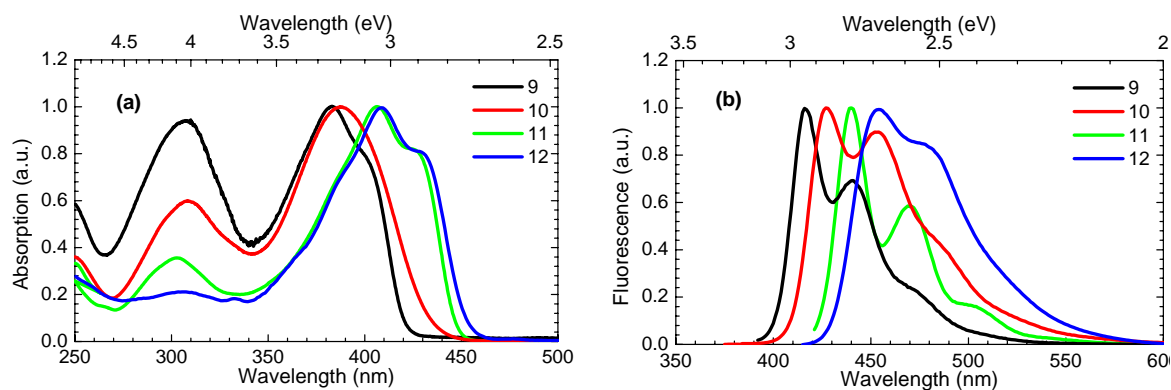


Figure 4.6: Absorption (a) and steady-state fluorescence (b) spectra for molecules **9-12**. Molecules **9** and **10** are dissolved in hexane, molecule **11** in cyclohexane, and **12** in methylene chloride.

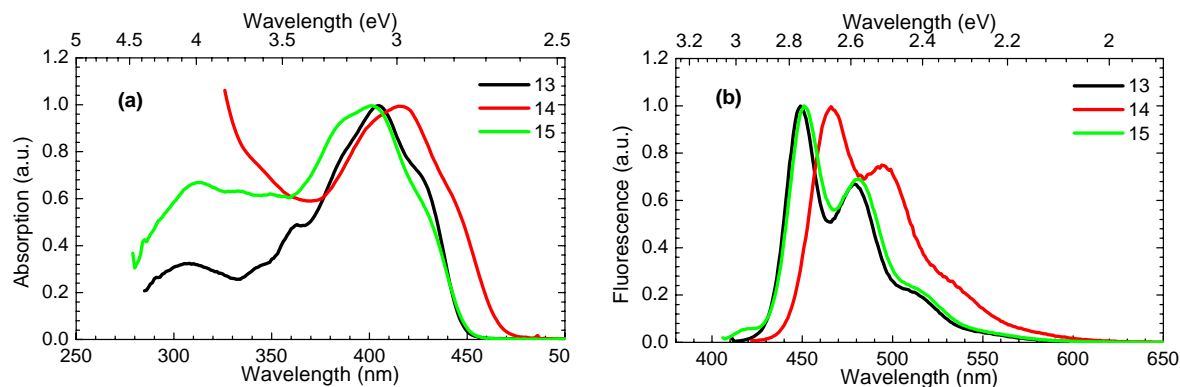


Figure 4.7: Absorption (a) and steady-state fluorescence (b) spectra for molecules **13-15** in hexane.

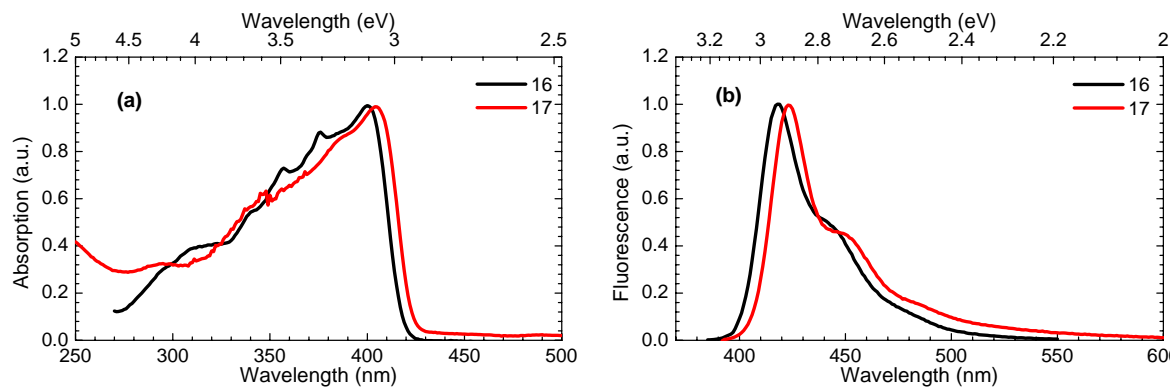


Figure 4.8: Absorption (a) and steady-state fluorescence (b) spectra for molecules **16** and **17** in hexane.

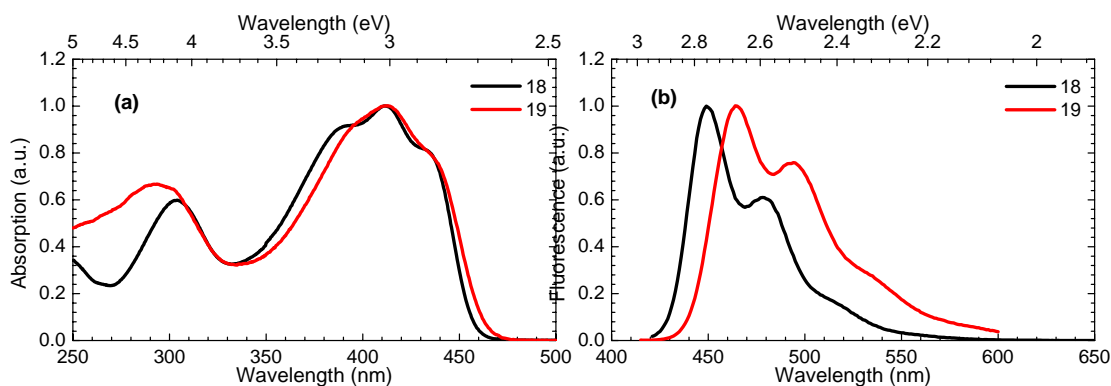


Figure 4.9: Absorption (a) and steady-state fluorescence (b) spectra for molecules **18** and **19** in cyclohexane.

The derivatives have been accordingly grouped for the purpose of allowing ease of comparison during the discussion of their structure-property relationships in Chapter 5. Nearly all of the compounds exhibit well-defined vibronic structures in both their absorption and emission spectra that have a progression of approximately  $1300\text{ cm}^{-1}$ , a value within the range of typical C–C and C=C stretching frequencies. In addition, the majority of compounds show a relatively small Stokes shift,  $\Delta\lambda_{\text{St}}$ , with no molecule exceeding a shift of 55 nm. The dipolar molecules shown in Figures 4.4, 4.6 (**9** and **10**), and 4.7 possess absorption spectra with two distinct peaks, one lying within the range 380–410 nm and the second positioned between 280 and 310 nm. These indicate the positions of the first and second electronic transitions (this is verified by the anisotropy curves below). The second feature is mostly suppressed in the symmetrically substituted molecules given in Figures 4.5, 4.6 (**11** and **12**), and 4.8 with the exception of molecule **5**. This is explained through simple symmetry arguments given in Section 5.1. However, the symmetrically substituted branched molecules (Figure 4.9) recover this second electronic transition feature, an attribute which will be discussed in Section 5.5. Finally,

the strength of the substituted accepting moiety in the dipolar molecules in Figure 4.4 slightly modifies the position of first excited state; a maximum shift of 28 nm is seen between **1** and **2**. On the other hand, the symmetrically substituted structures in Figure 4.5 show a significant shift of this electronic state depending on the electron active substituents; for A- $\pi$ -A molecules the shift can exceed 50 nm.

The results from the absorption and emission spectra shown above are summarized in Table 4.1. The first three columns include: the peak absorption wavelength corresponding to the first electronic transition  $\lambda_{abs}^{max}$ , the peak fluorescence wavelength  $\lambda_{flu}^{max}$ , and the Stokes shift  $\Delta\lambda_{st}$ , all of which are given in units of nm. In addition, the quantum yields of fluorescence  $\eta$  are given. The errors associated with these values are  $\pm 8\%$ . Compounds **8** and **20** were found to be non-fluorescent, that is, the value of  $\eta$  was determined to be less than 0.01. The peak molar absorptivities for the first excited state,  $\epsilon^{max}$ , are also given with units of  $M^{-1} cm^{-1}$ . These values have errors of  $\pm 10\%$ . Finally, using Equation 3.1 in conjunction with the absorption spectra and the values of  $\epsilon^{max}$ , the transition dipole moments between the ground and first excited states of the molecules were calculated. The values for  $\mu_{ge}$  are given in terms of debye (D). The dipole moment calculated for **4** was quite negligible ( $<0.5D$ ) and therefore not inserted. Given that the simplified 2PA cross-sections shown in Section 2.3 are quadratically dependent on  $\mu_{ge}$ , those molecules with stronger transition moments (such as the longer conjugated systems, **12-19**) promise to be the most efficient two-photon absorbers. Nevertheless, the magnitudes of other parameters, specifically changes in state dipole moments and higher level transition moments which play an equal role in the efficacy of 2PA, may suffer as a result of these large values of  $\mu_{ge}$ . Therefore, a compromise between these parameters is most likely to provide the greatest benefit to the measured nonlinearity.

Table 4.1: Linear optical properties for the fluorene derivatives in hexane.

Molecule	$\lambda_{abs}^{max}$ (nm)	$\lambda_{flu}^{max}$ (nm)	$\Delta\lambda_{st}$ (nm)	$\eta$	$\epsilon^{max}$ (M <sup>-1</sup> cm <sup>-1</sup> )	$\mu_{ge}$ (debye)
<b>1</b>	408	450	42	0.05	74,000	10.08
<b>2</b>	380	397	17	0.91	42,800	6.90
<b>3</b>	385	418	33	0.70	53,000	8.15
<b>4</b>	396	412	16	0.71	12,900	NA
<b>5</b>	375	390	15	0.40	44,000	7.14
<b>6</b>	365	389	24	0.90	74,800	9.13
<b>7</b>	316	322	6	0.84	49,300	4.29
<b>8</b>	324	Non-fluorescent	Non-fluorescent	<0.01	22,000	1.89
<b>9</b>	384	416	32	0.93	42,400	7.65
<b>10</b>	389	428	39	0.60	75,000	10.46
<b>11<sup>a</sup></b>	406	440	34	0.89	98,000	12.24
<b>12<sup>b</sup></b>	408	453	45	0.91	58,100	9.66
<b>13</b>	405	449	44	0.86	107,600	13.34
<b>14</b>	415	466	51	0.60	38,300	6.10
<b>15</b>	402	451	49	0.77	107,600	14.47
<b>16</b>	399	412	13	1.00	117,000	13.49
<b>17</b>	404	415	11	1.00	293,000	23.60
<b>18<sup>a</sup></b>	412	449	37	0.95	101,000	14.54
<b>19<sup>a</sup></b>	412	464	52	1.00	304,000	24.77
<b>20<sup>c</sup></b>	440	Non-fluorescent	Non-fluorescent	<0.01	23,500	9.26

<sup>a</sup> Solutions dissolved in cyclohexane

<sup>b</sup> Solution dissolved in methylene chloride

<sup>c</sup> Solution dissolved in tetrahydrofuran

Finally, the steady-state excitation anisotropy spectra for a selected number of molecules were determined. These curves can help resolve the spectral positions of different electronic transitions within absorption bands [43]. The excitation anisotropy spectra for molecules **3**, **5**, **6**, **10**, **12** and **16** (plots a, b, c, d, e and f, respectively) in silicon oil are shown along with their corresponding linear absorption spectra (in silicon oil as well) in Figure 4.10. Anisotropy values are shown on the right ordinate and absorption is represented on the left ordinate. These data can also be found in Reference 80. The constant anisotropy values within the long wavelength

absorption bands (350 - 450 nm) for all the compounds can be linked to the first electronic transition,  $S_0 \rightarrow S_1$ . For  $\lambda_{\text{exc}} \approx 310$  nm excitation anisotropy decreases and reaches a minimum value clearly indicating the position of the second electronic transition,  $S_0 \rightarrow S_2$ . This occurs as a result of the change in the orientation of the  $S_0 \rightarrow S_2$  transition dipole moment with respect to the  $S_0 \rightarrow S_1$  moment. The locations ascribed to these transitions by the anisotropy curves correlate quite well with the peaks of the absorption spectra. Therefore, these peaks can be used as indicators of the electronic transition energies.

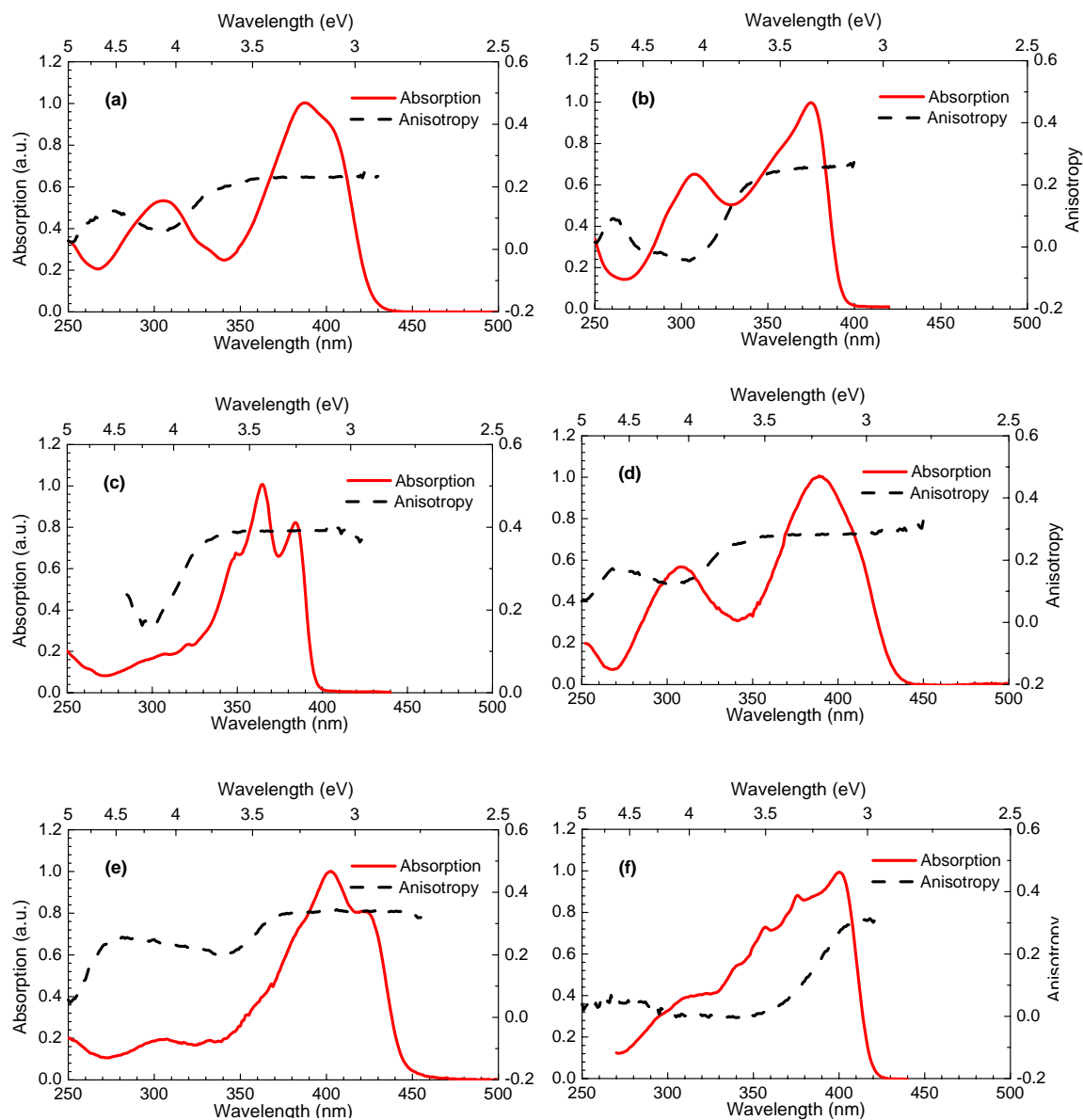


Figure 4.10: Linear absorption and steady-state excitation anisotropy spectra for molecules **3** (a), **5** (b), **6** (c), **10** (d), **12** (e), and **16** (f) in silicon oil.

## CHAPTER 5: STRUCTURE-PROPERTY RELATIONSHIPS

The prior Chapter introduced the fluorene derivatives which are the subject of this study. A brief summary of how their chemical structures have been systematically altered to generate different structural motifs was discussed (see Figure 4.3). In addition, the linear optical properties of these molecules were presented. Using the diagnostic tools described in Chapter 3, we can now calculate their nonlinear spectra and address the relationships between chemical structure and the two-photon absorbing properties of these molecules. Furthermore, given the simplified expressions for  $\delta$  given in Chapter 2, along with the linear optical properties of these derivatives determined both experimentally and quantum-chemically, plausible explanations for these identified trends can be put forth.

This Chapter is organized according to the structural motifs established in the preceding Chapter. The first Section analyzes the impact of structural symmetry on the 2PA spectra of these fluorene derivatives. Section 5.2 investigates the dipolar compounds (**1-4**) and discusses the effect modifying the ground-state polarization has on a molecule's nonlinearity. The subsequent Section looks at the symmetrically end-capped derivatives (**5-8**) and determines the benefits of using electron accepting versus electron donating terminal groups. The effect of extending the conjugated backbone of these molecules on their two-photon absorbing capability is covered in Section 5.4. The structural routes explored are extension via styryl (**9-12**), vinyl-fluorene (**13-15**), and amino-fluorene units (**16** and **17**). Section 5.5 details the consequences of moving away from linear archetypes to more two-dimensional structures using the multi-

branched derivatives (**18** and **19**). Finally, the concluding Section discusses using compound **20** to determine the role resonance enhancement can play in accentuating a molecule's 2PA.

Before the above relationships are broached, it is important to revisit an issue raised in Chapter 3: the use of multiple nonlinear spectroscopic techniques in the characterization of these two-photon absorbing molecules. Once again, multiple methods are used with the expressed intention of providing mutual support for the final experimental results. This is necessary as a consequence of the added requirement, when compared to linear spectroscopy, of having to accurately determine the pulse and beam characteristics of the excitation source. Figure 5.1 illustrates the resulting 2PA data acquired for molecule **3** from the three different methods described in Chapter 3. The formatting of this plot will be indicative of all the subsequent plots to follow in this Chapter. The symbols are the actual data points acquired from the experiments whereas the solid lines will be either one or two-peaked Gaussian fitting functions which are mainly used as guides for the eye. The y-axes denote 2PA cross-sections in GM units ( $1 \times 10^{-50} \text{ cm}^4 \text{ sec photon}^{-1} \text{ molecule}^{-1}$ ) and the top x-axis represents the sum of the two photon energies in eV involved in the 2PA measurement. For degenerate measurements (i.e. 2PF and Z-Scan), this is merely twice the energy of the excitation photon; for nondegenerate measurements (i.e. WLC pump-probe), this will be the sum of both the pump and probe photon energies. The lower x-axis shows these energies converted to a wavelength scale as a reference. Given the absolute errors for these experiments ( $\pm 15\text{-}20\%$ ), it is clear that at the peak of the 2PA spectra (3.22 eV or 385 nm) the results for all of the experiments are nearly the same, as one should expect. The main discrepancy between the two spectra (2PF and WLC pump-probe) exists at higher energies where the nondegenerate spectrum begins to indicate a larger nonlinearity. This is a consequence of the phenomenon of resonance enhancement alluded to in Section 2.4.2 and will



be discussed thoroughly in the following Chapter. Therefore, in order to minimize this effect and to achieve consistency with the results of the D-2PA techniques, when employing the WLC pump-probe method, the pump photon energy is chosen such that it coincides with the peak of the D-2PA spectrum. For compound **3** in Figure 5.1, this corresponds to a pump photon energy of 1.65 eV or 750 nm. Since the resulting nonlinear spectrum then becomes quasi-*degenerate* in nature, this explains the strong agreement noted between the two disparate methods. Given this agreement and the fact that we will mainly focus on peak two-photon absorptivities in this study, the results from these methods will be used interchangeably in the analysis that follows. Nonetheless, it should be noted that, as with any nonlinear characterization technique, occasionally the two methods (2PF and WLC pump-probe) do not show complete satisfactory agreement. In these instances, the Z-Scan method is used as a third, alternative measurement for the nonlinearity. Typically, this is only performed at a few selected wavelengths for validity, as shown in Figure 5.1. The results which exhibit the strongest concurrence from among the three techniques are used in the final analysis.

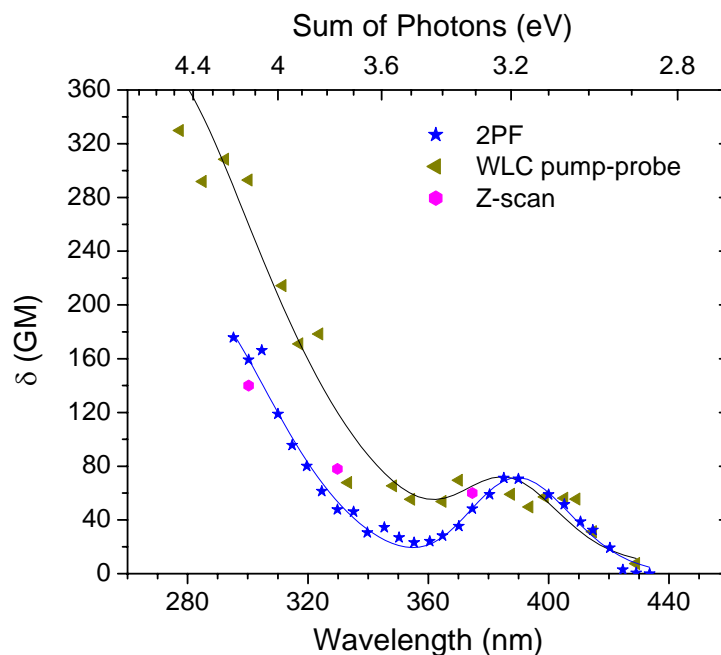


Figure 5.1: 2PA spectra for molecule **3** in hexane as acquired from the three different nonlinear characterization methods used in this study.

## 5.1 Symmetry

From quantum mechanics it is well-known that systems which exhibit symmetry through their center of inversion possess states with definite parity (i.e., the behavior of a wavefunction under reflection through the origin of spatial coordinates). These systems are known as centrosymmetric systems. Their states can generally be divided into symmetric  $g$  or unsymmetric  $u$  states. Furthermore, it is widely accepted that in these centrosymmetric systems linear excitation and two-photon excitation processes access states of differing parity (see, for example, Reference 33). One-photon absorption will gain access to a state which is opposite in symmetry to that of the ground state whereas 2PA will access a state of like symmetry. These are known as parity or dipole selection rules since they are valid under the electric-dipole approximation. Given that Chapter 2 follows the dipole approximation, one should be able to

understand these rules from the analysis given in Section 2.4.1. The transition dipole moment, given by Equations 2.15 and 2.15, can be rewritten as

$$\vec{\mu}_{if} = e \int \Psi_i^*(\vec{r}) \Psi_f(\vec{r}) \vec{r} d^3r \quad 5.1$$

where, as before,  $\vec{r}$  is the spatial coordinate, the  $\Psi_i$  and  $\Psi_f$  are wavefunctions of the initial and final states, and  $e$  is the charge on an electron. For a one photon transition to be allowed the integral must not vanish. Since the integration is applied overall space, the product must have even symmetry. Given that  $\vec{r}$  has odd symmetry, the product of the two wavefunctions must possess odd symmetry as well. This necessitates that the two states possess opposite parity or symmetry and therefore the only transitions that may be induced by one-photon absorption are the like:  $g \rightarrow u$  or  $u \rightarrow g$ . This can be further illustrated by Figure 2.1 where, for optically allowed transitions, the signs of the transition densities on opposite sides of the center of symmetry must be different to satisfy the selection rules. As explained in Chapter 1, two-photon excitation is mediated by a one-photon allowed intermediate state. Another transition from this intermediate state to the final state must also abide by the parity selection rules so that the ultimate state that two-photon absorption accesses must be the same as the initial state, i.e.  $g \rightarrow g$  or  $u \rightarrow u$ . In this sense, for centrosymmetric molecules one- and two-photon absorption are complimentary processes in that 2PA can investigate states that are one-photon forbidden. 2PA is therefore often used as a spectroscopic tool for the investigation of optically forbidden states. Finally, for molecules with no center of symmetry the states have no definite parity and therefore all excited states may be both one- and two-photon allowed.

For instance, in linear polyenes the lowest excited singlet state has the same symmetry as that of the ground state (that is  $A_g$ ) with the lowest one-photon allowed state ( $1B_u$ ) lying at a higher energy [81]. However, in diphenylpolyenic molecules the situation is reversed with the

$1B_u$  state indicated as the lowest excited state and the  $2A_g$  (or the lowest accessible two-photon state) state located energetically higher [37]. These diphenylpolyenic compounds are structurally more similar to the fluorene compounds than are the linear polyenes mainly due to the presence of aromatic phenyl groups within the compound. Therefore, one may very well expect the electronic structure of the fluorene derivatives to show a similar trend to that of the diphenylpolyenic compounds.

In fact, this is indeed the case. However, it should be noted that none of the fluorene compounds can be considered strictly a centrosymmetric molecule. Nonetheless, if one assumes the main portion of the photophysical activity of the molecules to occur along the conjugated backbone of the molecule (a valid assumption considering the appended alkane chains play little role in the optical properties of the system), certain derivatives can indeed exhibit the same parity selection rules associated with true centrosymmetric systems. These properties are demonstrated in Figure 5.2. In Figure 5.2a, the 2PA spectrum for the symmetric compound **6** in hexane is shown as acquired from the 2PF method. The formatting of the graph is the same as described above. In addition, both the linear absorption spectrum from Figure 4.5a and the excitation anisotropy spectrum from Figure 4.10c are also plotted. This molecule shows negligible 2PA into the first excited state which is identified by the peak in the linear absorption spectrum located at  $\sim 375$  nm (or 3.3 eV). This is expected given the nearly centrosymmetric structure of the A- $\pi$ -A molecule. Furthermore, the first two-photon allowed state (identified by the peak in the nonlinear spectrum located at 295 nm or 4.2 eV) is positioned very near the second excited state of the system (as identified by the minimum in the anisotropy curve), in a region located energetically higher than the first excited state. This is very similar to the true centrosymmetric diphenylpolyenic compounds mentioned above. The linear and nonlinear spectra for the dipolar

molecule number **3** are shown in Figure 5.2b. The 2PA data was acquired via the 2PF technique. In addition, the excitation anisotropy spectrum extracted from Figure 4.10a is also plotted. One can immediately see that not only is there significant 2PA into the second excited state (located at ~300 nm and identified by both the linear absorption and anisotropy spectra) of the molecule, but the peak position of the 2PA spectrum correlates quite well with the position of the first excited state for this system as illustrated by the location of the first peak in the linear absorption spectrum (385 nm or 3.22 eV). Given that this molecule possesses no center of symmetry, it is not surprising that each of the transitions ( $S_0 \rightarrow S_1$  and  $S_0 \rightarrow S_2$ ) is two-photon allowed.

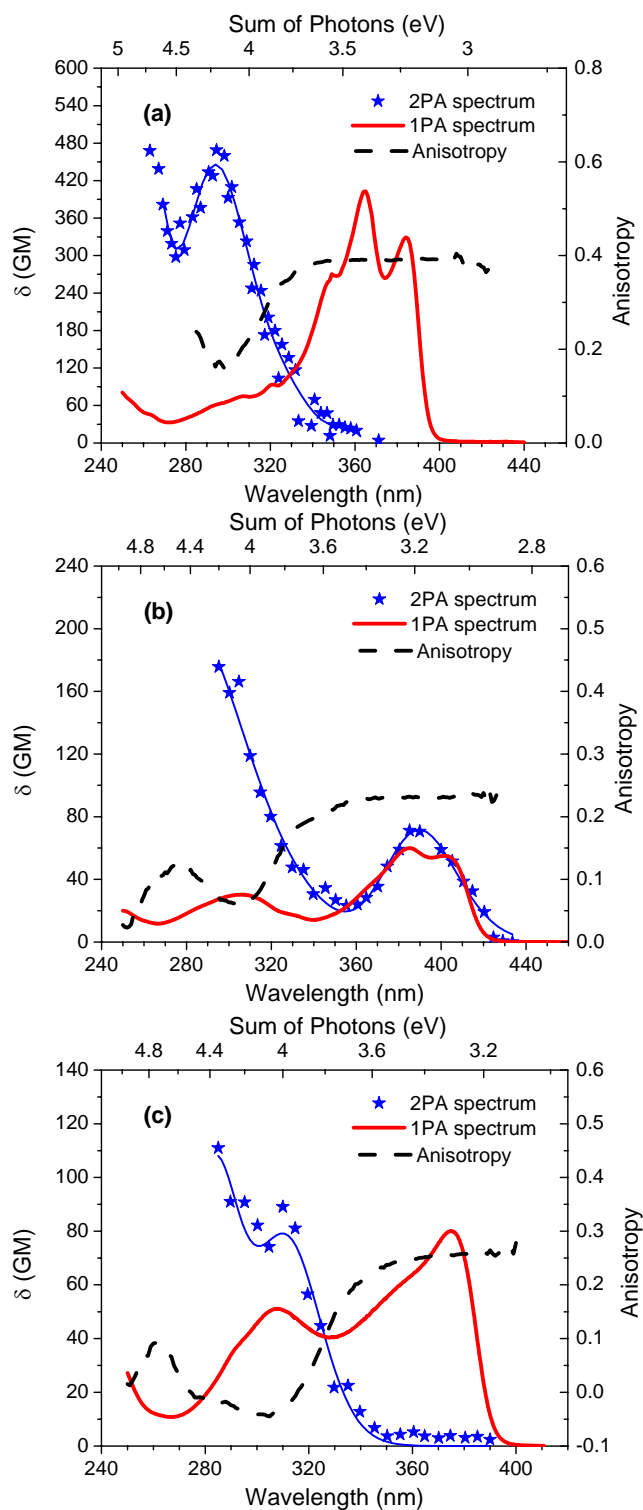


Figure 5.2: 2PA and 1PA spectra for molecules **6** (a), **3** (b), and **5** (c) in hexane. The excitation anisotropy spectra in silicon oil were taken from Figure 4.10.

Finally, the one- and two-photon absorption spectra along with the excitation anisotropy spectrum for the symmetric compound **5** are plotted in Figure 5.2c. Once again, the nonlinear spectrum is a result of the 2PF method. Given the symmetric nature of this system (D- $\pi$ -D), one should expect similar trends to those observed for compound **6**. As expected, there appears to be negligible nonlinear absorption into the first strongly allowed one-photon state (3.3 eV). However, although the 2PA peak does lie energetically higher than this first state, it also seems to correspond to the peak of a second strongly allowed linear transition (300 nm or 4 eV). This is in contrast to molecule **6** whose peak 2PA lies in a region where linear absorption is quite weak. If indeed parity selection rules are to hold, a two-photon allowed transition must be strictly one-photon forbidden. In order to investigate this, quantum-chemical calculations (see Section 3.5) were carried out which verified that, indeed, the molecule possesses both a two-photon allowed state and a strongly allowed one-photon state which are separated by less than 0.05 eV. The summary of this information is given in Table 5.1. The transition energies are given (in eV) on the left side of the Table while the strengths of the transition dipole moments (in debye or D) are on the right side. There is a slight overestimation of the position of the first excited state (by 0.22eV) in the quantum-chemical calculations which is mainly attributed to an overcorrelation of the ground state in the MRDCI approach (see Section 3.5). However, the position of the second strongly allowed one-photon transition is calculated quite accurately (i.e.,  $E_{05}=4.01$  eV).<sup>6</sup> The next transition,  $E_{06}$ , is weakly one-photon allowed as evidenced by the low magnitude of its transition dipole moment. However, as described by Equation 2.14 in Section

2.3, strong 2PA in centrosymmetric systems requires there to be a strong transition dipole between higher lying excited states (i.e.,  $\mu_{ee'}$ ). The sixth singlet state clearly exhibits this with a value for  $\mu_{16}$  of nearly 6 D. Therefore, this state is responsible for the strong 2PA indicated in Figure 5.2c and it becomes obvious why the linear and nonlinear absorption spectra are coincident given that  $E_{05}$  and  $E_{06}$  are separated by less than 0.05 eV.

Table 5.1: Select quantum-chemically calculated transition energies and dipole moments for molecule **5**.

Transition Energy (eV)		Transition Dipole Moment (debye)	
$E_{01}$	3.53	$\mu_{01}$	8.78
$E_{05}$	4.01	$\mu_{05}$	4.95
$E_{06}$	4.05	$\mu_{06}$	0.92
		$\mu_{16}$	5.80

In conclusion, although the symmetric fluorene derivatives are not strictly centrosymmetric systems, they exhibit the same parity selection rules present in these latter systems. Furthermore, the asymmetric derivatives clearly indicate that significant 2PA is possible into any excited state. Moreover, these trends will follow for all of the derivatives studied here and not just the three molecules analyzed above. The two exceptions to this rule will be the multi-branched structures, **18** and **19**, and these deviations will be discussed in Section 5.5.

---

<sup>6</sup> The second strongly excited one-photon transition actually corresponds to the 5<sup>th</sup> excited singlet state. There are weakly excited transitions at lower energies however they are not detectable in the linear absorption and excitation



## 5.2 Dipolar Molecules

Optimization strategies involving the nonlinearity of dipolar type organic compounds have been studied in great detail [82]. It has been well-established that modulating the degree of ground-state polarization, or the degree of charge separation in the ground state, in these molecules can exert significant influence over their molecular polarizability and hyperpolarizabilities (see, for example, References 17 and 83). This charge separation in the ground state can be controlled primarily by either modifying the chemical structure (i.e., altering the strength of the donating and accepting substituents) or the system's environment (i.e., controlling the polarity of the host solvent). The effects of altering the chemical structure in this way were detailed by Oudar in 1977 [84]. He demonstrated that a series of di-substituted molecules with strong donor-acceptor intramolecular charge transfer character exhibited very large values of  $\beta$ , the first hyperpolarizability. He also showed that these enhancements could be predicted from the basic properties of the first electronic excited state. Furthermore, in 1989, Garito *et al.* [85] predicted that donor-acceptor polyenes with significant charge transfer character would show enhanced values of  $\gamma$ , the second hyperpolarizability, compared to unsubstituted centrosymmetric polyenes. The idea of altering molecular geometry by varying solvent polarity to achieve desired optical properties was established far earlier by Brooker and Sprague in 1941 [86]. Its extension to nonlinear optical properties was introduced by Marder in 1993 [87].

Although both of these effects may behave differently on a local level, they effectively correspond to applying an electric field across a polarizable  $\pi$ -conjugated system. From this

---

anisotropy experiments.

concept, Meyers and co-workers [88] were able to develop a quantum-chemical methodology to systematically investigate how the ground-state polarization can modify the molecular polarizabilities. The authors examined, theoretically, how the influence of an external static electric field affected conjugated chromophores such as linear polymethines. This applied field was shown to be effective in controlling charge separation in the ground state and consequently was quite useful in simulating the effects of varying donor/acceptor (D/A) strength as well as medium polarity. They were subsequently able to determine  $\alpha$ ,  $\beta$ , and  $\gamma$  (using the same Sum-Over-States formalism presented in Section 2.2) as a function of the strength of the applied field. This approach spurred on numerous experimental and theoretical studies by Marder and co-workers investigating how substituent and/or solvent-induced geometric changes can play an important role in determining molecular NLO response [83,87,88,89].

For donor-acceptor polyenes, Meyers *et al.* [88] showed that ground-state polarization is related to a geometrical parameter, the bond-order alternation (BOA) which is defined as the average of the difference in the  $\pi$ -bond order between adjacent carbon-carbon bonds. Since the applied field used by the authors served the expressed purpose of modulating the ground-state polarization, BOA is also controlled by this parameter. Consequently, the evolution of the polarizabilities  $\alpha$ ,  $\beta$ , and  $\gamma$  as a function of the ground-state polarization can be mapped in terms of bond-order alternation as well. Given that the second hyperpolarizability  $\gamma$  is directly related to the 2PA cross-section  $\delta$  (see Equation 2.5), we will only be concerned with its evolution versus BOA. This evolution is shown in Figure 5.3 for a D/A polyene exactly as it appeared in Reference 88. Here,  $\gamma$  (in units of  $10^{-36}$  esu) is plotted versus the BOA of the polyene as the strength of the external field is tuned (BOA is tuned in a positive sense, that is, left to right as the

ground-state polarization or field strength is increased). Specific regions of ground-state polarization are labeled (A through F) for ease of identification.

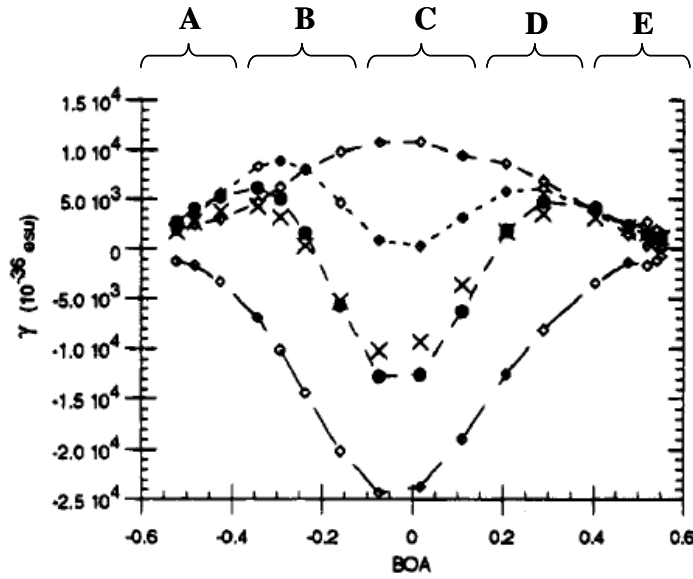


Figure 5.3: Evolution of the second hyperpolarizability  $\gamma$  versus BOA for a donor-acceptor polyene. Curves:  $\gamma_{SOS}$  – crosses;  $\gamma_{model}$  – full circles, dash line; D term – diamonds, short dash line; N term – diamonds, long dash line; T term – diamonds, medium dash line (taken from [88]).

The  $\gamma_{SOS}$  curve, which is shown using crosses, exhibits two positive peaks appearing in regions B and D. There also exists a large negative minimum in region C, near the zero BOA point. As we have chosen to do in this study, the authors compared their full SOS calculations with the simplified essential states model described in Section 2.3. The results from this analysis, namely  $\gamma_{model}$ , can be identified by the full circles lying along the dash line. Since the simplified analysis reproduces the fully-converged results quite well, they also plotted the individual terms from this analysis (similar to the D, N and T terms appearing in Equation 2.8). The D (dipolar) term, which is dependent on  $\Delta\mu_{ge}$  and  $\mu_{ge}$ , is shown with the diamonds and the short dash line. It is

apparent that this term is responsible for the two positive peaks. The N (negative) term, dependent only on  $\mu_{ge}$ , causes the large negative peak at the zero BOA limit (identified by diamonds, long dash line). Finally, the T (two-photon) term, which is dependent on  $\mu_{ge}$  and  $\mu_{ee'}$ , is always positive and presents a maximum in region C (diamonds, medium dash line). The most crucial revelation from the T and D curves (which we have already established are the only important terms involved in two-photon absorption) is that there exists an optimum degree of ground-state polarization (or BOA) that maximizes  $\gamma$ . Therefore, these curves should provide plausible explanations for the results discussed in the following Sections mainly because they relate the nonlinearity to other properties, such as the transition and state dipole moments.

### 5.2.1 Acceptor Strength

The first approach we have taken to modifying the ground-state polarization is to alter the strength of the electron withdrawing terminal group on a fluorene molecule which is end-capped with a diphenylamine donating group. The donor-acceptor molecules under investigation are derivatives **1-4**. As we progress through the molecules **1** to **4**, the strength of the acceptor group decreases: nitro > cyano > benzothiazole > acetyl. The 2PA spectra for all the molecules are shown in Figure 5.4.

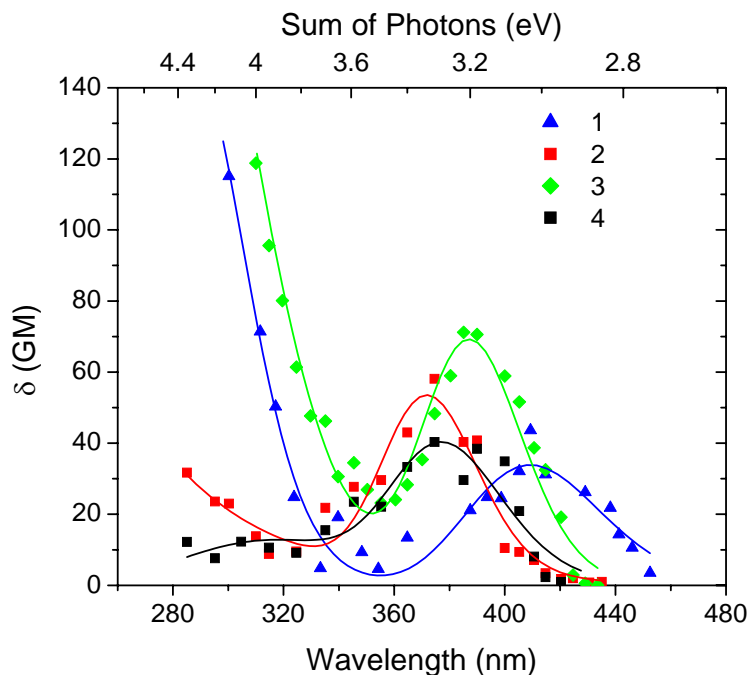


Figure 5.4: Experimentally determined 2PA spectra for dipolar molecules **1-4** in hexane.

All four of the molecules were dissolved in hexane and the spectra for molecules **2-4** were acquired via the 2PF technique. The 2PA spectrum for **1** is a result of the WLC pump-probe method where a pump wavelength of 750 nm was used. Although the linear absorption spectra for the molecules are not shown, their nonlinear spectra are nearly coincident with the first peaks in the linear spectra shown in Figure 4.4a which identify the first excited states ( $S_1$ ) in these molecules. This can be verified by comparing the peaks of the linear absorption spectra tabulated in Table 4.1 with the locations of the peak two-photon absorptivities listed in Table 5.2 below (labeled as  $\lambda_{\text{exp}}^{\text{max}}$ ). This trend is certainly consistent given the fact that these dipolar systems possess no center of symmetry (see Section 5.1). As expected (from the linear absorption analysis), the value of  $\lambda_{\text{exp}}^{\text{max}}$  does not vary significantly as the strength of the donating

species is altered. However, the peak magnitude of the nonlinearity (labeled as  $\delta_{\text{exp}}^{\text{max}}$  in Table 5.2) in  $S_1$  does show variation as the withdrawing group is changed. Compound **3**, which possesses the benzothiazole structure as its terminal group, exhibits the largest 2PA cross-section. In fact, it looks to be a local maximum within this region of ground-state polarization. This is interesting considering its accepting group has an intermediate value of electron withdrawing character compared to the other substituents studied. It should be noted here that molecules **1** and **3** have been studied previously in our group [56]. Although the magnitudes of the cross-sections given in Reference 56 have since been proven to be inaccurate, the trend seen in that study matches the one seen here: the molecule with the weaker accepting end-group (**3**) shows an enhanced nonlinearity.

Table 5.2: Location and magnitude of the peaks of the 2PA spectra for molecules **1-4** as determined experimentally (Figure 5.4) and quantum-chemically (Figure 5.5).  $\lambda$  is given in nm and  $\delta$  in GM units. The peak 2PA cross-sections derived from the essential states model (Equation 2.11) are also given.

Molecule	Experimental		Quantum-Chemical		
	$\lambda_{\text{exp}}^{\text{max}}$	$\delta_{\text{exp}}^{\text{max}}$	$\lambda_{\text{SOS}}^{\text{max}}$	$\delta_{\text{SOS}}^{\text{max}}$	$\delta_{\text{ESM}}^{\text{max}}$
<b>1</b>	410	43.6	356	75.3	95.1
<b>2</b>	372	58.1	340	58.0	108.3
<b>3</b>	387	71.2	358	68.0	133.3
<b>4</b>	377	40.3	340	33.7	41.5

In an attempt to provide a suitable explanation for these observations, the degenerate 2PA spectra for molecules **1-4** were calculated via the quantum-chemical methodology detailed in Section 3.5. These spectra are presented in Figure 5.5. In addition, the wavelengths and

magnitudes associated with their peak values are given in Table 5.2 ( $\lambda_{SOS}^{\max}$  and  $\delta_{SOS}^{\max}$ ). Immediately, one can see that the theoretically predicted 2PA maxima are slightly blue-shifted with respect to their experimentally determined counterparts (~30-40 nm). This is again due to an overcorrelation of the ground state geometry as discussed in the previous Section. Yet still, the relative spectral positions of these curves show reasonable agreement with the experimental data. And, perhaps more importantly, these results predict the shape and magnitude of the experimentally determined spectra remarkably well. The one exception is molecule **1** where the peak 2PA cross-section into  $S_1$  is overestimated in the SOS analysis. This is a consequence of the resonant nature of the nitro ( $NO_2$ ) end-group in molecule **1** which precluded a completely accurate determination of the ground-state geometry for this structure during the quantum-chemical analysis. The discrepancies in the SOS and experimental spectra at shorter wavelengths (<340 nm) are merely an artifact of the nondegenerate nature of the experimental technique. Nonetheless, the overall agreement of the results gathered from theory and experiment is quite promising.

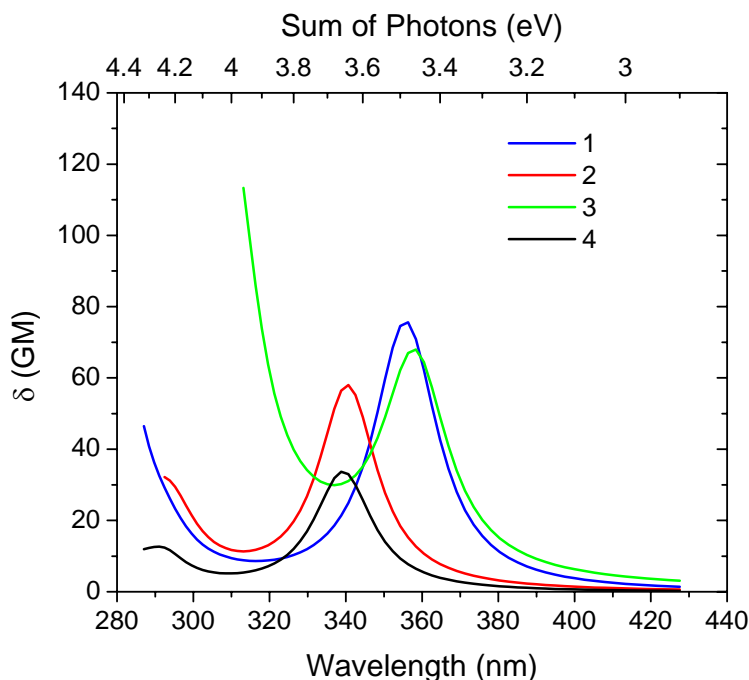


Figure 5.5: Quantum-chemically determined 2PA spectra for dipolar molecules **1-4** according to the methodology detailed in Section 3.5.

This success prompted our use of the essential states model put forth in Section 2.3 to determine the peak 2PA cross-sections into the first excited state of these derivatives. Since these are dipolar molecules, the simplified expression for the D-term (Equation 2.11) in the essential states analysis was used and the results are presented in Table 5.2 ( $\delta_{ESM}^{\max}$ ). The relevant dipole moments for these calculations (as determined quantum-chemically) are given in Table 5.3. One can immediately note that the peak cross-sections are larger than the results derived from the fully-converged SOS approach. This is a consequence of the contribution of higher-lying one-photon allowed states to the fully converged results that result in mixed contributions which tend to reduce  $\delta_{SOS}^{\max}$ . This is not surprising given that the linear absorption spectra for these systems (Figure 4.4a) clearly indicate that there are additional strongly allowed one-photon



states around 4 eV. Nevertheless, this simplified analysis reproduces quite well the trends we have observed previously. After viewing the governing elements in these calculations (Table 5.3), the results seem justified. Even though compound **3** possesses a much weaker withdrawing group than either of the first two molecules, the change in state dipole moment ( $\Delta\mu_{01}$ ) upon excitation is not drastically reduced and furthermore its first transition moment ( $\mu_{01}$ ) more than compensates for this small discrepancy. Given the quadratic dependence of these terms in Equation 2.11, it is not surprising that molecule **3** shows the largest nonlinearity.

Table 5.3: Select quantum-chemically calculated dipole moments (in Debye) for molecules **1-4**. These terms are used in the calculations for  $\delta_{ESM}^{\max}$  which are given in Table 5.2.

Molecule	$\mu_{01}$	$\Delta\mu_{01}$
<b>1</b>	7.47	9.06
<b>2</b>	7.64	9.45
<b>3</b>	10.31	7.77
<b>4</b>	7.16	6.24

In conclusion, the theoretical analysis reinforces the trends shown in the experimental results: molecule **3** seems to possess an optimal ground-state polarization for 2PA into the first excited state. Furthermore, this trend could have been predicted by the evolution of the dipolar (D) with BOA shown in Figure 5.3. This is evidenced in region B where the D term from the simplified version of  $\gamma$  exhibits a local maximum in its contour. Given the relationship between  $\gamma$  and  $\delta$ , it is not unexpected that Kogej *et al.* [23] also showed that there exists an optimum BOA at which 2PA is maximized in a series of donor-acceptor substituted stilbene derivatives.

Although the strongest accepting moiety in our series (molecule **1**) does not seem to reproduce the eventual reduction of the nonlinearity to zero as suggested by region C in Figure 5.3, there is evidence that the external fields used in the work by Meyers [88] and Kogej [23] may, in fact, be unrealistically large thereby preventing observation of this minimum in the nonlinearity. This point will be discussed further in the next Section. Therefore, this study of the fluorene dipolar derivatives illustrates that there is an optimum degree of ground-state polarization which maximizes  $\delta$  and furthermore it does not necessarily correspond to the molecule which possesses the strongest ground-state dipole moment. Molecule **3**, with its benzothiazole terminal group, has the optimal charge transfer character which maximizes its state and transition dipole moments, the main factors which dictate the strength of the 2PA.

### 5.2.2 Solvism

Solvism is the effect that solvent environment can have on the physical or photophysical properties of a solute. This concept is germane because the second avenue we have chosen to pursue in the modification of the ground-state polarization is to vary the polarity of the host solvent. The molecule we have chosen to investigate is the dipolar derivative **3** since it exhibited the optimal charge transfer character for 2PA. The polarity of the solvents can be characterized by their orientational polarizability which is given by

$$\Delta f = \frac{\varepsilon - 1}{2\varepsilon + 1} - \frac{n^2 - 1}{2n^2 + 1} \quad 5.2$$

where  $\varepsilon$  is the static dielectric constant (not to be confused with the peak molar absorptivity  $\varepsilon^{\text{max}}$ ) and  $n$  is the refractive index of the solvent [43]. These parameters are tabulated in Table 5.4 for

the solvents which we have chosen to use: hexane (HEX), tetrahydrofuran (THF), methylene chloride (MCL), cyclohexanone (CYC), and acetone (ACT). The solvents are listed in order of increasing polarity.

Table 5.4: The dielectric constant  $\epsilon$ , refractive index  $n$ , and polarity  $\Delta f$  of the solvents used in the solvism investigation.

Solvent	$\epsilon$	$n$	$\Delta f$
HEX	1.9	1.375	$8 \cdot 10^{-5}$
THF	7.5	1.403	0.210
MCL	9.1	1.424	0.219
CYC	18.2	1.450	0.248
ACT	20.7	1.359	0.284

The linear absorption and fluorescence spectra for molecule **3** in these solvents are presented in Figure 5.6. In addition, their linear optical properties are summarized in Table 5.5. These parameters are similar to the ones presented for all of the derivatives in Table 4.1 earlier: peak absorption and emission wavelengths, Stokes shifts, quantum yields, peak molar absorptivities, as well as the dipole moments for the  $S_0 \rightarrow S_1$  transition. Immediately, one notes the negligible solvatochromism (the spectral shift associated with the peak absorption or emission wavelength as solvent is varied [43]) that is present in the linear absorption spectra; the differences between  $\lambda_{abs}^{max}$  do not vary by more than 5-9 nm.

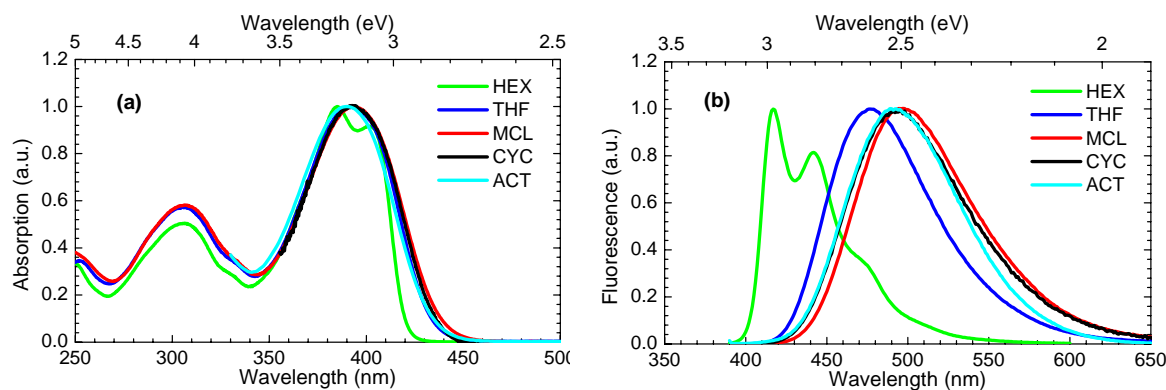


Figure 5.6: Absorption (a) and steady-state fluorescence (b) spectra for molecule **3** in various solvents.

On the contrary, the fluorescence spectra exhibit a considerable dependence on solvent polarity. This behavior is typical for molecules which undergo a large change in dipole moment upon excitation and is attributed to rearrangement of the solvent shell when the molecule is in the excited state [43]. The Stokes shifts are seen to exceed 100 nm giving promise that the molecule has non-negligible interaction with the host solvent. The quantum yields remain quite high in all of the host environments. In addition, the transition dipole moments (as calculated from  $\epsilon^{\max}$  and Equation 3.1) remain relatively constant as the solvent polarity is varied. Provided that the dipolar term (D) can adequately describe the induced 2PA in these systems (as was the case for molecule **3** in hexane, see previous Section), this constancy of  $\mu_{01}$  implies that any dependence of the 2PA cross-section on host solvent must be attributed to a variation of  $\Delta\mu_{01}$ .

Table 5.5: Linear optical properties for the molecule **3** in various solvents. In addition, the peak 2PA cross-sections as determined experimentally (Figure 5.7) are also given.

<b>Solvent</b>	$\lambda_{abs}^{max}$ (nm)	$\lambda_{flu}^{max}$ (nm)	$\Delta\lambda_{st}$ (nm)	$\eta$	$\epsilon^{max}$ (M <sup>-1</sup> cm <sup>-1</sup> )	$\mu_{01}$ (debye)	$\delta_{exp}^{max}$
<b>HEX</b>	385	418	33	0.70	53,000	8.15	71.2
<b>THF</b>	392	467	75	0.55	62,000	9.33	98.3
<b>MCL</b>	394	494	100	0.90	38,000	7.41	133.1
<b>CYC</b>	393	495	102	1.00	46,600	8.02	167.1
<b>ACT</b>	391	492	101	0.58	42,000	7.80	202.3

The 2PA spectra determined from the 2PF technique are shown in Figure 5.7 for all of the solvents under investigation. The peak 2PA cross-sections ( $\delta_{exp}^{max}$ ) for these curves are summarized in Table 5.5. Clearly, host solvent polarity shows a profound effect on the nonlinearity. As the polarity is increased from that of hexane ( $\Delta f \approx 0$ ) to that of the most polar solvent acetone ( $\Delta f = 2.84$ ), the nonlinearity nearly triples in magnitude going from 71 GM to over 200 GM. Furthermore, the strength of the 2PA monotonically increases as the polar character of the solvent is raised. We now return to the trends predicted by Meyers [88] and Kogej [23] discussed in the previous Section. Making the assumption that the D term accurately describes the 2PA process, as BOA increases (or equivalently as one increases solvent polarity) a maximum in the nonlinearity should occur (region B) followed by a minimum which occurs near the zero BOA point (region C). Clearly, the experimental results reproduce the increase in the nonlinear response present at lower values of the BOA. However, no maximum is observed and certainly no subsequent minimization of the nonlinearity is found which would indicate an optimal solvent polarity for 2PA. Therefore, it seems that solvent polarity does not possess the capability to modify the degree of ground-state polarization in this molecule to the extent that

altering the withdrawing character of the acceptor end-group had in the previous Section. It has been noted by both Albert [90] and Luo [91] in their studies of dipolar polyenes, that the external fields used by the authors above are too unrealistically large to accurately portray the effect solvent polarity has on either  $\gamma$  or  $\delta$ . In fact, Luo *et al.* found a similar trend to the one observed in this study in a push-pull polyene: the 2PA cross-section increased monotonically and showed no apparent maximum when varying the polarity of the host solvent over a similar range.

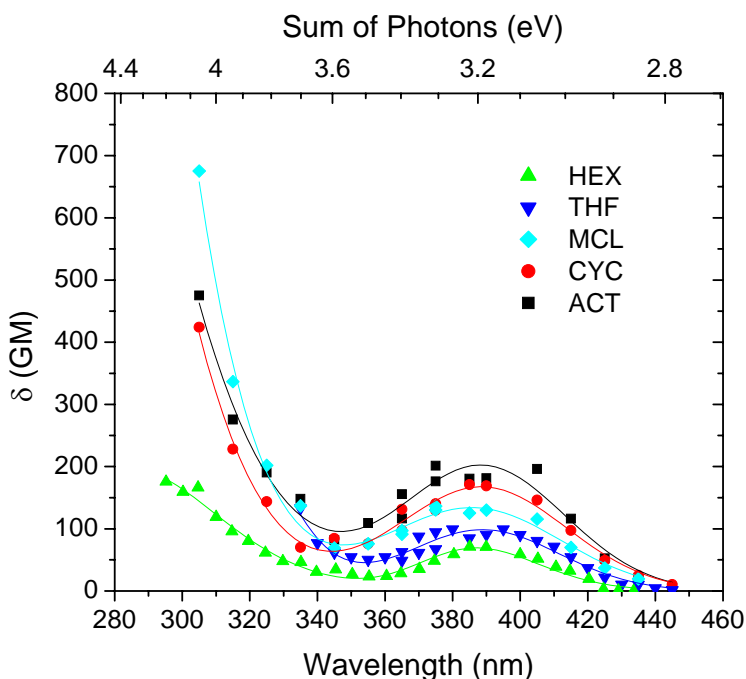


Figure 5.7: Experimentally determined 2PA spectra for dipolar molecule **3** in various solvents.

Quantum-chemical calculations were not carried out to verify the solvent dependence our dipolar molecule exhibited. The reason for this is that these calculations (see Section 3.5) are specifically performed on isolated molecules, thus neglecting solvent effects altogether.

Nonetheless by viewing the dipolar term from the essential states model, one can clearly see that the variation in  $\delta$  with polarity must be associated with a strengthening of the charge transfer characteristics of the molecule in the excited state. This modification of  $\Delta\mu_{01}$  is assured because of the relatively constant value of  $\mu_{01}$  observed in all the solvents. This suggests that those molecules which benefit from large changes in state dipole moment in nonpolar solvents, stand to profit the most from these solvism effects. Bourhill [89] and Albert [90] supported this assertion finding that solvent dependent changes are highly architecture specific and that large changes should be observed in systems which are substantially stabilized upon charge separation. To test this supposition, molecule **9** was dissolved in two different host solvents and its 2PA spectra were attained. This molecule is a modified version of **3** with its conjugated backbone extended via a styryl bridge. The detailed effects of this extended conjugation will be discussed in Section 5.4.1 however, it is sufficient to note that this molecule possesses a larger value of  $\Delta\mu_{01}$  than derivative **3** and therefore should be more susceptible to environmental conditions. The results obtained from the 2PF technique for this molecule in hexane and methylene chloride are shown in Figure 5.8. Clearly the molecule enjoys the same enhancement in its nonlinearity that was afforded molecule **3** when its host polarity was increased. The peak 2PA cross-sections into  $S_1$  ( $\sim 3.1$ - $3.2$  eV) in hexane and MCL are 183.6 GM and 642 GM, respectively. This translates to a 3.5 times enhancement of  $\delta$  which is significantly larger than the 1.87 times improvement observed for molecule **3** in the same solvents (see Table 5.5).

Another interesting observation is that the second peak ( $\sim 4.0$  eV) in both nonlinear absorption spectra indicates 2PA accessing the  $S_0 \rightarrow S_2$  transition. This transition also shows greater than 3 times enhancement for the solution in the more polar solvent. This is reminiscent of the process described by the two-photon term (T) in the essential states model for

centrosymmetric systems (see Section 2.3). In fact, the T term has been used to describe such transitions in dipolar systems previously [23]. It is clear from Figure 5.3 that the T term should enjoy enhancement of the nonlinearity with increasing ground-state polarization (or BOA) similar to that observed for D-type transitions. Furthermore, Equation 2.14, which describes the T term, indicates that this enhancement is most likely attributed to a corresponding enhancement in the higher level transition dipole moment,  $\mu_{12}$ . This promises improvement not only in dipolar systems such as this one but may very well portend enhancement in centrosymmetric systems as well where  $\mu_{ee'}$  is a crucial term governing 2PA. In conclusion, dipolar fluorenyl systems such as molecules **3** and **9** undoubtedly benefit from a more polar environment. This enhancement in the nonlinearity is a result of the greater charge transfer produced upon excitation, a situation which is further ameliorated in systems which possess intrinsically larger values of  $\Delta\mu_{ge}$ . Although the effects of solvism do not indicate an optimum degree of ground-state polarization which maximizes  $\delta$ , as was the case when varying the terminal acceptor strength, the consequences of modifying the polarization in either manner have proven to be quite beneficial.



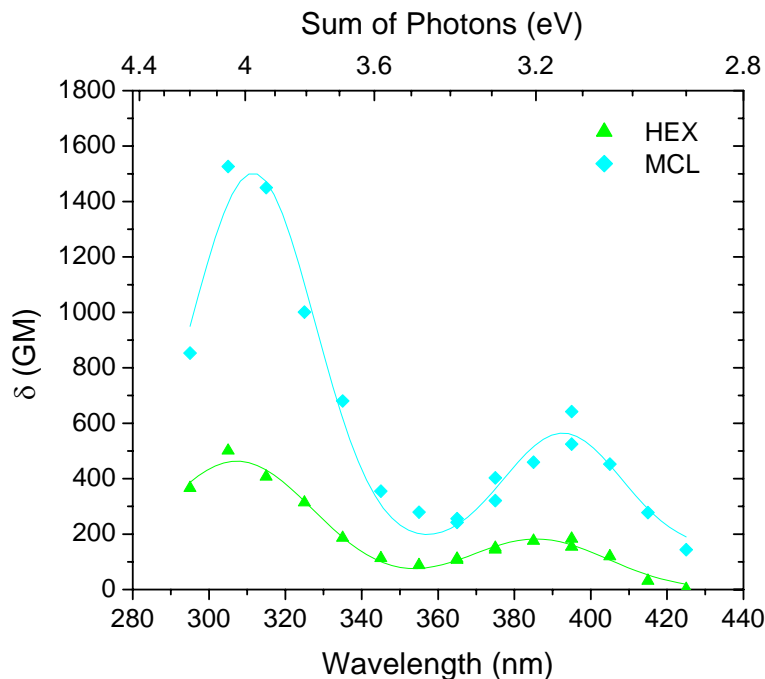


Figure 5.8: Experimentally determined 2PA spectra for dipolar molecule **9** in hexane and methylene chloride.

### 5.3 Symmetric Molecules

Just as altering the strengths of the electron donating and accepting substituents in dipolar systems can be a means to investigate structure-property relationships, the same avenue exists for symmetric systems as well. A significant amount of work has been devoted to optimization strategies involving symmetrically substituted conjugated molecules [22,37,38,92]. In particular, a great portion of this work utilizes molecules with quadrupolar type geometries, that is, centrosymmetric systems with the following motifs: D- $\pi$ -A- $\pi$ -D or A- $\pi$ -D- $\pi$ -A. In this architecture, the enhancement of the nonlinearity is achieved through effective charge transfer upon excitation. This charge transfer can occur from the ends of the molecule to its center or vice versa. One can see why quadrupolar geometries may serve in maximizing this phenomenon

since the central substituent (either A or D) should assist this transfer in the excited state. As discussed in Section 2.3, the essential states model predicts the two-photon or T term should adequately describe 2PA in symmetrically substituted systems. This has been verified in many of the works mentioned above. Equation 2.14 immediately declares that the two transition moments,  $\mu_{ge}$  and  $\mu_{ee'}$ , play the most significant roles in optimizing 2PA in these systems (assuming negligible contribution from the detuning term). Specific discussion concerning the transition moments (Section 2.4.1) justifies why enhancement of the two-photon absorptivity should occur irrespective of the direction of charge transfer in quadrupolar molecules. Given that large charge densities on the periphery of the molecule tend to increase the magnitude of the dipole moment, even if one of the transition moments concentrates charge density at the center of the molecule the other transition moment will compensate by moving it to the periphery. Furthermore, it stands to reason that the same arguments used for optimizing dipolar molecules by modulating their degree of ground-state polarization should follow for quadrupolar systems as well. However, in this case, the polarization is sought to favor charge transfer from the donor groups to the acceptor moieties.

### 5.3.1 Donor Versus Acceptor End-Groups

However, dissimilar to the quadrupolar systems described above, the molecules investigated here will be symmetrically end-capped derivatives with the general architecture of D- $\pi$ -D or A- $\pi$ -A. Unlike stilbene derivatives [22,37,38], for instance, the fluorene derivatives are not strictly centrosymmetric and therefore do not possess a center of inversion. This makes appending electron active moieties as side groups to the central  $\pi$  bridge, a cornerstone of

quadrupolar synthesis, rather difficult. However, the possibility of pursuing this route in the future will be discussed below. Nevertheless, the arguments which were presented above for quadrupolar systems are still quite valid for pure symmetrically end-capped systems (see either Reference 37 or Albota *et al.* in Reference 92). This Section will concentrate on the benefits of using electron accepting versus electron donating terminal groups in symmetrically end-capped fluorene derivatives. As explained in Section 5.1, these derivatives exhibit the same parity selection rules associated with true centrosymmetric systems and therefore 2PA will only access the second excited states (or equivalently the first two-photon allowed state) in these molecules. As such, we will use the two-photon or T term from the essential states model to provide plausible explanations for the trends observed.

The two compounds we have chosen to investigate are molecules **5** and **6**. Molecule **5** has a D- $\pi$ -D structure with diphenylamine end-groups as the donating moieties. Molecule **6** exhibits an A- $\pi$ -A geometry with the accepting moieties being the benzothiazole units. Since these molecules were briefly investigated in Section 5.1, their 2PA spectra will merely be re-plotted in Figure 5.9. Once again, the spectra were obtained via the 2PF method.

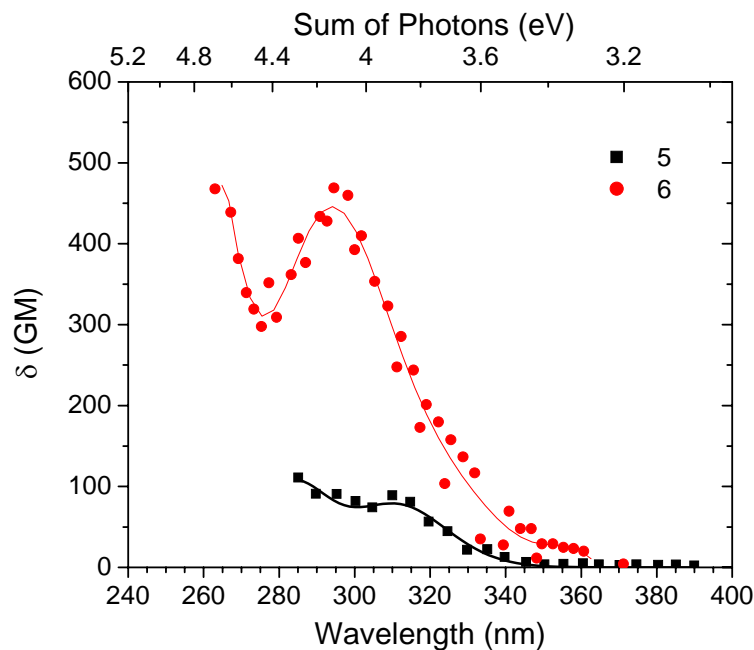


Figure 5.9: Experimentally determined 2PA spectra for symmetric molecules **5** and **6** in hexane.

Immediately, one can see that the end-capped acceptor derivative provides over a five times enhancement in the peak two-photon absorptivity compared to the symmetrical donor substituted molecule. Since acceptor moieties are more likely to induce charge transfer from the center of the molecule to its periphery upon excitation, the enhancement of nonlinearity is not completely unexpected. Referring back to Figure 5.2, it is clear that both peaks in the nonlinear spectra correspond to the second excited state as identified by the steady-state fluorescence anisotropy spectra and therefore their comparison should be valid. However, we should bear in mind that **5** was shown to have a nearly degenerate one-photon state at the location of the first strongly allowed two-photon transition as well. Although this should not invalidate the comparison of these two systems, it may be a plausible explanation as to the greater efficiency of 2PA in **6**. The Thomas-Kuhn sum rules [93] state that the total amount of oscillator strength (a term directly

related to the dipole moment) in a conservative molecular system is dictated by the number of electrons in that molecule. Assuming an equal number of electrons present in **5** and **6**, which is approximately true, the lack of a second strongly allowed one-photon state (i.e., a significant amount of oscillator strength associated with this transition) in **6** may very well cause redistribution of the total oscillator strength into a higher lying transition. In terms of the T term, this would certainly benefit that molecule's 2PA.

In order to investigate this supposition, quantum-chemical calculations were performed to determine the degenerate 2PA spectra for both of these molecules. The results from these calculations are shown in Figure 5.10.

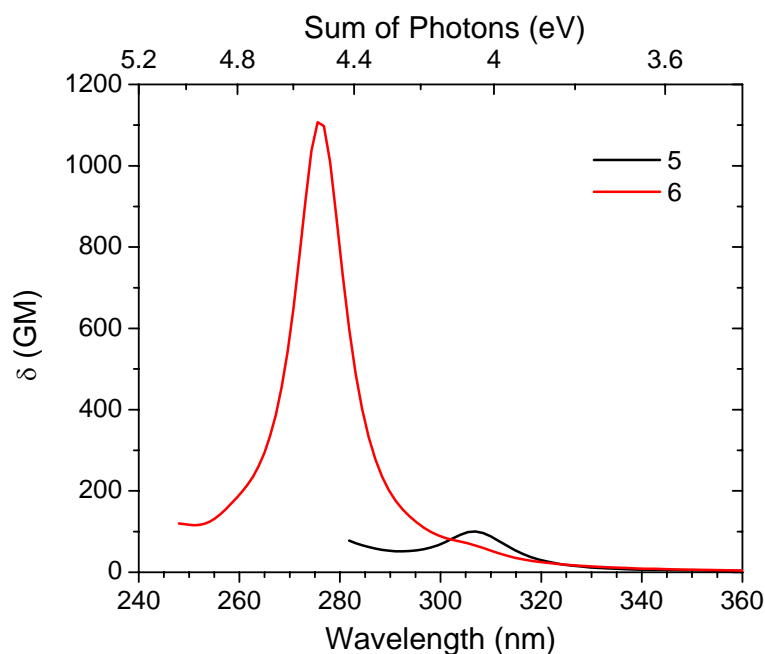


Figure 5.10: Quantum-chemically determined 2PA spectra for symmetric molecules **5** and **6** according to the methodology detailed in Section 3.5.

The spectra reproduce the trend that the acceptor substituted system outperforms the donor end-capped system. However, while the peak nonlinearity for molecule **5** gives nearly quantitative agreement with the experimental results, the theoretically predicted spectrum for **6** clearly overestimates the nonlinearity. The peak 2PA cross-sections and their associated  $\lambda^{\max}$  values for both the experimental and theoretical spectra are shown in Table 5.6 for convenience. A possible explanation for this overestimation of the nonlinearity may be due to intra-molecular torsion. It has been well-established [38,94] that a departure from planarity (or twisting) within a molecule can result in reduced conjugation and subsequent reduction in the 2PA cross-sections. Since the quantum-chemical calculations performed here do not take into account the fully relaxed, nonplanar conformations of the molecules, the nonlinearity for molecule **6** may be artificially inflated. This is not surprising given that Zhao *et al.* [95] showed that compounds containing benzothiazole units exhibit a reduction in their nonlinearity when nonplanar configurations are considered.

Table 5.6: Location and magnitude of the peaks of the 2PA spectra for molecules **5** and **6** as determined experimentally (Figure 5.9) and quantum-chemically (Figure 5.10).  $\lambda$  is given in nm and  $\delta$  in GM units. The peak 2PA cross-sections derived from the essential states model (Equation 2.14) are also given.

Molecule	Experimental		Quantum-Chemical		
	$\lambda_{\text{exp}}^{\max}$	$\delta_{\text{exp}}^{\max}$	$\lambda_{\text{SOS}}^{\max}$	$\delta_{\text{SOS}}^{\max}$	$\delta_{\text{ESM}}^{\max}$
<b>5</b>	310	89.1	307	100.1	97.5
<b>6</b>	295	468.9	276	1107.4	1400.2

With the discrepancy in the theoretical spectrum of molecule **6** acknowledged, we still hoped to gain insight from results garnered from the essential states model. Using the equation for the T term given in Section 2.3, the peak 2PA cross-sections into the first two-photon allowed state were calculated and the results are shown in Table 5.6. Although the value of  $\delta_{ESM}^{\max}$  for molecule **6** still overestimates the nonlinearity, the trend observed remains the same. Therefore, we chose to look at the dominant transition dipole moments which contribute to this transition. The relevant dipole moments for these calculations (as determined quantum-chemically) are given in Table 5.7.

Table 5.7: Select quantum-chemically calculated transition energies and dipole moments for molecules **5** and **6**. These terms are used in the calculations for  $\delta_{ESM}^{\max}$  which are given in Table 5.6.

<b>Molecule 5</b>				<b>Molecule 6</b>			
Transition Energy (eV)		Transition Dipole Moment (debye)		Transition Energy (eV)		Transition Dipole Moment (debye)	
E <sub>01</sub>	3.53	$\mu_{01}$	8.78	E <sub>01</sub>	3.59	$\mu_{01}$	11.82
E <sub>05</sub>	4.01	$\mu_{05}$	4.95	E <sub>02</sub>	4.05	$\mu_{12}$	3.40
E <sub>06</sub>	4.05	$\mu_{16}$	5.80	E <sub>07</sub>	4.49	$\mu_{17}$	13.16

First of all, we note that the peak of the fully-converged SOS spectrum for **6** is located at 276 nm or 4.49 eV (see Table 5.6). According to the quantum-chemical results, this corresponds to the  $S_0 \rightarrow S_7$  transition and yet there is another two-photon allowed transition at 4.05 eV ( $S_0 \rightarrow S_2$ ). This is denoted by the non-negligible value of  $\mu_{12}$ . Since the experimentally observed peak for 2PA lies at 295 nm or 4.2 eV, one could argue that this  $S_0 \rightarrow S_2$  transition corresponds to this

peak. However, the value of  $\mu_{12}$  associated with this transition would produce a peak cross-section of less than 60 GM, clearly not a magnitude which would well describe the experimental results. Therefore, we are reasonably certain that the  $S_0 \rightarrow S_7$  transition corresponds to the observed two-photon process. Secondly, the first transition moment  $\mu_{01}$  of **6** is roughly 1.3 times greater than that of **5** (11.8 D compared to 8.8 D). This agrees well with our experimental findings (9.13 D to 7.14 D – taken from Table 4.1). Given that these differences are not nearly sufficient to account for the differences in nonlinearity observed experimentally, the dominating factor must be the higher lying transition moment  $\mu_{ee'}$ . This seems to be the case given the observation that the  $\mu_{16}$  moment for molecule **5** is less than half that of the large value of 13.2 D calculated for  $\mu_{17}$  in molecule **6**. This could certainly be a result of the redistribution of oscillator strengths mentioned previously when one notes that the one-photon allowed transition  $S_0 \rightarrow S_5$  for **5** possesses nearly the same magnitude dipole moment as the  $S_1 \rightarrow S_6$  transition which actively participates in the 2PA process. Along these lines, Kuzyk [96] showed that redistribution of oscillator strengths can play a major role in the efficacy of 2PA in organic molecules.

Finally, the ZDO transition densities associated with the higher lying transition moments  $\mu_{ee'}$  were calculated for the two molecules. These plots are similar to those found in Section 2.4.1. The transition densities corresponding to the  $S_1 \rightarrow S_6$  transition for molecule **5** and the  $S_1 \rightarrow S_7$  transition in **6** are shown in Figure 5.11. Although the large atomic densities found towards the periphery of molecule **5** would normally promise a large transition moment, the densities on the nitrogen atoms and the nearest neighbor carbon atoms are opposite in sign, somewhat neutralizing their overall effect. On the contrary, although the atomic densities shown for **6** are not as pronounced, they are all of similar sign and extend further from the center of the



molecule than is the case for **5**. This essentially accounts for the larger transition moment and consequently enhanced 2PA observed in molecule **6**. So, for the two architectures analyzed here – the D- $\pi$ -D structure of molecule **5** and the A- $\pi$ -A structure of molecule **6** – the acceptor substituted derivative clearly outperforms the donor end-capped derivative. From quantum-chemical calculations, this can be attributed to an enhanced transition moment created upon excitation. This is not surprising given that electron withdrawing groups are more likely to induce center-to-periphery charge transfer, a necessity for efficient 2PA in symmetric systems.

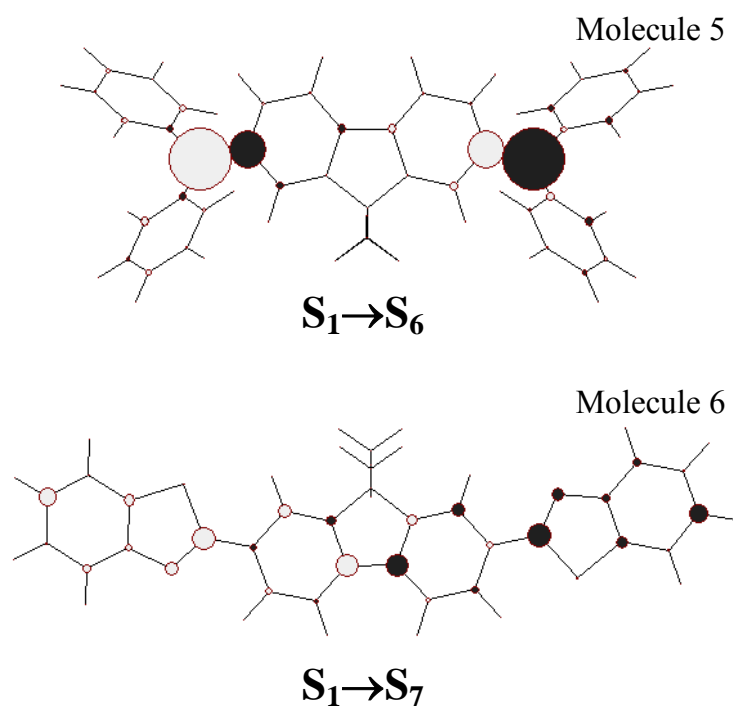


Figure 5.11: Quantum-chemically calculated atomic transition densities for upper level transitions in molecules **5** and **6**.

### 5.3.2 Acceptor Strength

As in dipolar systems, it should be possible to optimize symmetric molecules by modulating the degree of ground-state polarization. Given the success with the acceptor substituted derivative number **6**, molecules **7** and **8** were synthesized in the hopes of providing even greater charge transfer in the excited state. The fluorenyl derivative **7** is end-capped with cyano groups which we have established are stronger accepting moieties than the benzothiazole groups in molecule **6**. Although the next logical step would be to use nitro groups in a symmetrically substituted geometry, synthesis of this derivative proved to be difficult and therefore one cyano species in molecule **7** was replaced with a nitro substituent to create derivative **8**. The 2PA spectrum for molecule **8** in hexane is shown in Figure 5.12 along with the nonlinear spectrum for molecule **6** as a reference. Since this compound exhibited extremely weak fluorescence ( $\eta < 0.01$ ), the WLC pump-probe method was employed using a pump wavelength of 600 nm. First, the peak of the nonlinear spectrum lies at ~290 nm whereas its linear absorption spectrum is peaked at 324 nm. This indicates that the system, although not strictly symmetrical, behaves as one by exhibiting negligible 2PA into the  $S_1$  state. But, more to the point, the magnitude of the nonlinearity is considerably smaller than that of the benzothiazole substituted derivative showing a peak cross-section of only 30.3 GM. Note that the 2PA spectrum for **8** has been artificially increased by a factor of 5 for ease of viewing. A plausible explanation for this is the extremely small value of  $\mu_{01}$  calculated experimentally (Table 4.1). The value of 1.9 D is almost five times smaller than that of molecule **6**. Furthermore, it is unlikely that the higher lying transition moment in **8** would show comparative magnitude either.

This would most likely be a consequence of the shorter conjugation length over which charge could be transferred (i.e., terminal groups with shorter lengths).

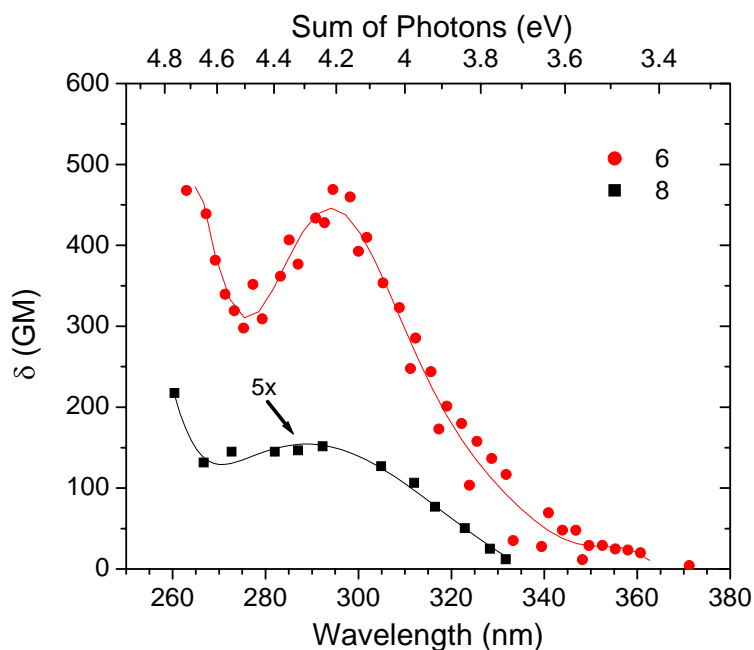


Figure 5.12: Experimentally determined 2PA spectra for symmetric molecules **6** and **8** in hexane. The nonlinear spectrum for **8** has been magnified for ease of viewing.

We were unable to detect any substantial 2PA for molecule **7** using any of the three experimental techniques available. This could also be a consequence of a reduced conjugation which prohibits significant charge transfer. Another possible explanation could be the fact that since the location of the first excited state is already at relatively high energies (Table 4.1 indicates a peak wavelength of 316 nm or 3.9 eV), the first two-photon allowed state may lie too far into the ultraviolet region for detection. At any rate, from the limited amount of data acquired, molecule **6** seems to exhibit the maximum nonlinearity. This seems to reinforce the

same observation put forth in Section 5.2.1: that the accepting terminal group of benzothiazole optimizes a system's nonlinearity. Most likely, this optimization can still be improved upon even by using stronger accepting end-groups. However, care should be taken that the chosen substituent provides a good conjugation pathway for effective charge transfer. Finally, future work should certainly involve attempts at synthesizing molecules with quadrupolar geometries given that many groups have observed substantial benefits to 2PA when employing these architectures. Given the success shown by molecule **6**, this provides the most likely starting point. Appending a donor substituent somewhere along the central  $\pi$ -conjugated backbone (perhaps using strategies along the lines of those used in the synthesis of derivatives **18** and **19**) may serve in maximizing the nonlinearity by assisting charge transfer in the excited state.

## 5.4 Conjugation Length

Section 2.4.1 details the benefits of optimizing both transition and state dipole moments (and consequently two-photon absorption) by ensuring that transition densities far from the center of a molecular system be large. We have previously shown that large changes in terminal charge density can be facilitated by manipulating molecular endgroups which are electron active, that is, by effectively controlling the ground-state polarization. However, perhaps a more straightforward way to maximize these peripheral charge densities is by extending the conjugation length of a molecule. This effectively increases the distance over which charge can migrate in the excited state. The benefits of systems possessing large conjugated backbones were understood as far back as the early 1970's. Hermann and Ducuing [97] were one of the first persons to recognize that large optical nonlinearities should be expected in conjugated

chains found in organic molecules. To test this theory, they measured the second-order hyperpolarizability  $\gamma$  for a series of saturated and unsaturated molecules. The saturated molecules (i.e., non-conjugated carbon chains) consisted of alkanes ( $C_nH_{2n+2}$ ) and cycloalkanes ( $C_nH_{2n}$ ) and their results are shown in Figure 5.13a.

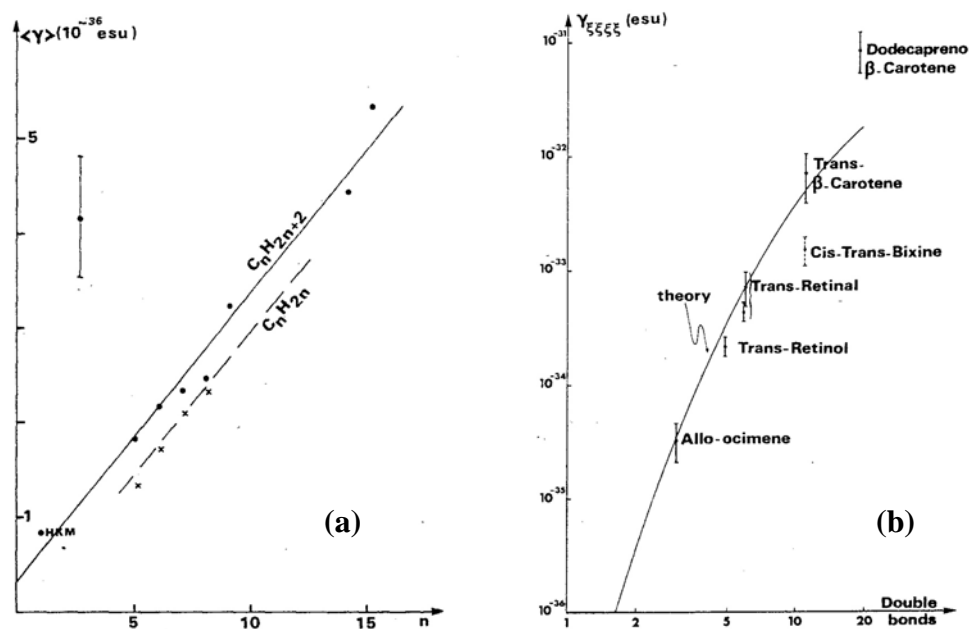


Figure 5.13: Dependence of chain length on the value of  $\gamma$  for a series of (a) saturated molecules – alkanes and cycloalkanes and (b) unsaturated molecules – polyenes (taken from [97]).

Both of these families indicated a fairly linear variation of  $\gamma$  with the number of carbon atoms  $n$  in the molecules. However, the study of a series of linear conjugated molecules (i.e., unsaturated molecules) consisting of polyene chains showed remarkably different results. Figure 5.13b reveals a superlinear increase of  $\gamma$  with chain length (the graph is plotted on a log-log scale).

These results revealed not only the influence of delocalization on optical nonlinearities but also illustrated the sizeable gains which could be achieved by extending conjugation length.

Since this discovery, a considerable body of work focused on exploiting conjugation length for increased nonlinearities has developed. A good synopsis of this work (as well as an excellent review on structure-property relationships in general) was produced by Tykwinski and co-workers [98]. The authors point out that, for a number of specific organic systems, it has been well-established that  $\gamma$  can generally be related exponentially to conjugation length or number of repeat units  $N$  in the following form:

$$\gamma \propto N^{\alpha} . \quad 5.3$$

Values of  $\alpha$  have been shown to vary in a range from 2.3 to 5.4 depending upon the chemical structure. Furthermore, it should be noted that one should not expect this dependence to continue on indefinitely. Beyond some chain length  $\gamma$  will saturate due to the tradeoff between the increase in the distance over which charge can migrate and the decrease in effective coupling between the center and periphery [99]. Conjugation length dependent nonlinearity studies have been performed on unsubstituted systems such as polytriacetylenes [100] as well as on extended quadrupolar type molecules [101]. And, perhaps the most germane for our study, Puccetti *et al.* [102] investigated the chain-length dependence of  $\gamma$  for both donor and acceptor symmetrically substituted polyenes as well as asymmetric donor-acceptor (push-pull) polyenes.

Despite the large body of work detailing the dependencies of  $\gamma$  on conjugation length, nearly all of these studies involve either polyene type structures or some other linearly conjugated system. Systems which employ aromatic ring structures as part of their conjugated backbone, like the fluorenes investigated here, have received a paucity of attention perhaps due to the difficulty in synthesizing long, conjugated aromatic systems. The effects these longer

molecules have on the efficiency of 2PA are even less well-known. Two studies, in particular, have addressed these issues: Albota *et al.* [92] and Rumi and co-workers [37] each investigated both bis(styryl)benzene and bis-donor diphenylpolyene compounds. These molecules are derivatives of the more commonly recognized stilbene molecule with various modifications made to the substitution patterns. The conjugation length is extended by either lengthening the intermediate polyene chain or by substituting phenylene groups (i.e. a benzene substituent) along the main backbone. Since these systems cannot be characterized by a true “chain” length, the authors gauge the effect of extending the conjugation length by looking at the contribution to the peak nonlinearity ( $\delta^{\max}$ ) per double bond or  $\delta^{\max}/N$  (where  $N$  is the number of double bonds in the  $\pi$ -conjugated bridge and a phenylene group counts as 1.5 double bonds). The authors determined that  $\delta$  depended almost linearly on conjugation length among all of these molecules. Although this might portend negligible benefits to conjugation extension in aromatics when compared to linear polyene chains, one should note that aromatic systems enjoy other advantages such as high photostability (see Section 4.1). Furthermore, in slightly shorter molecules, aromatic systems enjoy comparable if not larger nonlinearities. Therefore, the following Section will investigate the benefits to extending the  $\pi$ -conjugated backbone of these fluorene derivatives using different structural routes. In order to gauge the efficacy of these structural modifications, the peak nonlinearity  $\delta^{\max}$  will be studied as well as its contribution per double bond  $\delta^{\max}/N$ .

### 5.4.1 Styryl Extension

As mentioned above, the effects of conjugation length extension should benefit both asymmetric as well as symmetrically substituted systems. As such, we chose to investigate elongated versions of the dipolar archetypes discussed in Section 5.2 as well as the symmetrically substituted motifs studied in Section 5.3.

#### 5.4.1.1 Dipolar Molecules

Molecules **9** and **10** represent variations of the dipolar systems studied in Section 5.2 with a styryl extension (vinyl group or double bond followed by a phenylene group) preceding the electron withdrawing terminal group. Molecule **9** has a benzothiazole end-group attached to the styryl bridge while **10** possesses a phosphonic acid diethyl ester as its terminal unit. The 2PA spectra for these compounds in hexane are shown in Figure 5.14. The nonlinear spectrum for molecule **3** is given as a reference. The spectra for **9** (as shown previously in Figure 5.8) and **10** were acquired using the 2PF technique. As expected, for a dipolar system, the nonlinear spectra are nearly coincident with their linear absorption spectra. This can be verified by comparing the values of  $\lambda_{\text{exp}}^{\text{max}}$  given in Table 5.8 with the locations of linear absorption peaks given in Table 4.1. As mentioned in Section 5.2.2, this is a clear indication that 2PA is accessing both the  $S_1$  and  $S_2$  states. In addition, Table 5.8 summarizes the peak 2PA cross-sections  $\delta_{\text{exp}}^{\text{max}}$  for each transition as well as their effective cross-sections  $\delta^{\text{max}}/N$ . These values reveal that there is a definitive enhancement in the nonlinearity as a result of the styryl extension.



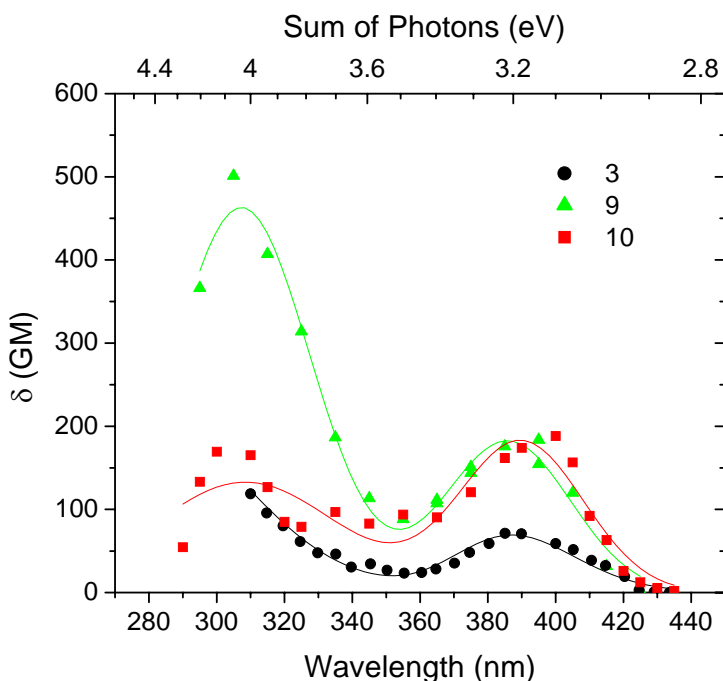


Figure 5.14: Experimentally determined 2PA spectra for molecules **3**, **9** and **10** in hexane.

The most direct comparison should be made between molecules **3** and **9** since they possess identical withdrawing moieties. The peak cross-section for the  $S_0 \rightarrow S_1$  transition is approximately 2.5 times greater in the elongated system while the higher level transition shows over a 4 times enhancement in the nonlinearity. However, taking into account the number of conjugating double bonds involved (3 for molecule **3** and 5.5 for molecules **9** and **10**), the contributed nonlinearity per double bond remains relatively constant for the lower transition ( $\sim 28$  GM) while the upper level transition seems to indicate greater efficiency (90 GM compared to 40 GM). When comparing the longer molecules with disparate electron withdrawing moieties, that is, **9** and **10**, the strength of the nonlinearity into the first excited state remains unchanged. However, the strong enhancement into  $S_2$  which was noted for molecule **9** seems to be destroyed

for molecule **10**. Consequently, the efficacy of this two-photon transition is severely depleted falling below that of the shorter conjugated system.

Table 5.8: Location and magnitude of the peaks of the 2PA spectra into the first two excited states for molecules **3**, **9** and **10** as determined experimentally (Figure 5.14).  $\lambda$  is given in nm and  $\delta$  in GM units. In addition, the contribution of  $\delta$  per double bond is given.

Molecule	$S_0 \rightarrow S_1$			$S_0 \rightarrow S_2$		
	$\lambda_{\text{exp}}^{\text{max}}$	$\delta_{\text{exp}}^{\text{max}}$	$\delta_{\text{exp}}^{\text{max}}/N$	$\lambda_{\text{exp}}^{\text{max}}$	$\delta_{\text{exp}}^{\text{max}}$	$\delta_{\text{exp}}^{\text{max}}/N$
<b>3</b>	387	71.2	23.7	310	121.5	40.5
<b>9</b>	395	183.6	33.3	305	501.2	91.2
<b>10</b>	400	188.2	34.2	300	169.4	30.8

Although quantum-chemical calculations have not been carried out for these molecules, the essential states model can still be applied for intuitive explanations. The experimentally determined values for the first transition dipole moment  $\mu_{01}$  are very nearly the same for molecules **3** and **9** (see Table 4.1). Therefore, the enhancement in the nonlinearity for **9** must be a result of an augmented value for  $\Delta\mu_{01}$  when dealing with D- type transitions into the first excited state and larger values of  $\mu_{12}$  for T-type transitions into  $S_2$  (see Section 2.3). This argument is equally valid when applied to molecules **9** and **10**. Given that **10** possesses a larger dipole for the  $S_0 \rightarrow S_1$  transition, the contribution from  $\Delta\mu_{01}$  must be greater for molecule **9** to generate an equivalent nonlinearity. This becomes even more evident for the value of  $\mu_{12}$  when examining the nonlinearity into  $S_2$  in view of the fact that molecule **10** suffers such a decrease in 2PA. Both of these observations could probably be attributed to the reduced conjugation present in **10** as a result of the phosphonic acid terminal group although such conjectures are difficult to

support without the aid of transition density plots. Next, when studying the peak cross-sections  $\delta_{\text{exp}}^{\text{max}}$  for all the molecules, one notes that these values are larger for 2PA into the second excited state than into the first state. At first glance, this would seem to imply that the magnitude of the higher lying transition moment must be significantly larger than the change in state dipole moments  $\Delta\mu_{01}$ . However, there also exists the resonant enhancement or detuning term in the T-type expression (Equation 2.14) which undoubtedly plays a role in this transition's nonlinearity. Nonetheless, as evidenced by the increase in effective nonlinearity  $\delta^{\text{max}}/N$  for the  $S_0 \rightarrow S_2$  transition in molecule **9**, the styryl extension clearly benefits 2PA into the higher lying state to a greater degree. Although it is difficult to make assertions without access to the actual magnitudes of the dipole moments, one might expect the dependence of  $\mu_{12}$  on styryl conjugation length to be favored over  $\Delta\mu_{01}$ . Despite these minor details, clearly the overall nonlinearity profits from this structural change. Judging by these results, as well as the results presented in the following Section, a future direction would be to either further extend the bridge with an additional styryl unit before the withdrawing end-group or possibly interleave a styryl bridge before the diphenylamine donating group. This would give clear evidence as to the functional dependence of the dipole moments (and consequently the nonlinearity) on this type of conjugation extension.

#### 5.4.1.2 Symmetric Molecules

Molecules **11** and **12** are variations of the symmetric systems studied in Section 5.3 with a styryl extension preceding the terminal group on both sides. Molecule **11** is symmetrically

substituted with diphenylamine end-groups and molecule **12** possesses benzothiazole terminal groups. The 2PA spectra for these compounds, **11** in cyclohexane and **12** in methylene chloride, are shown in Figure 5.15 along with their linear absorption spectra. In addition, the nonlinear spectra for molecules **5** and **6** are shown with **11** and **12**, respectively, for points of reference. The nonlinear spectra for **11** and **12** were acquired via the 2PF method. As expected, in these symmetric systems the dominant 2PA in both molecules seems to be accessing a higher lying two-photon state. Unfortunately, it is unclear if this is the  $S_2$  state which lies around 300 nm (or 4.13 eV) since the nonlinear spectra do not exhibit definitive peaks. We have therefore identified these peaks by the shortest wavelength for which data was acquired.

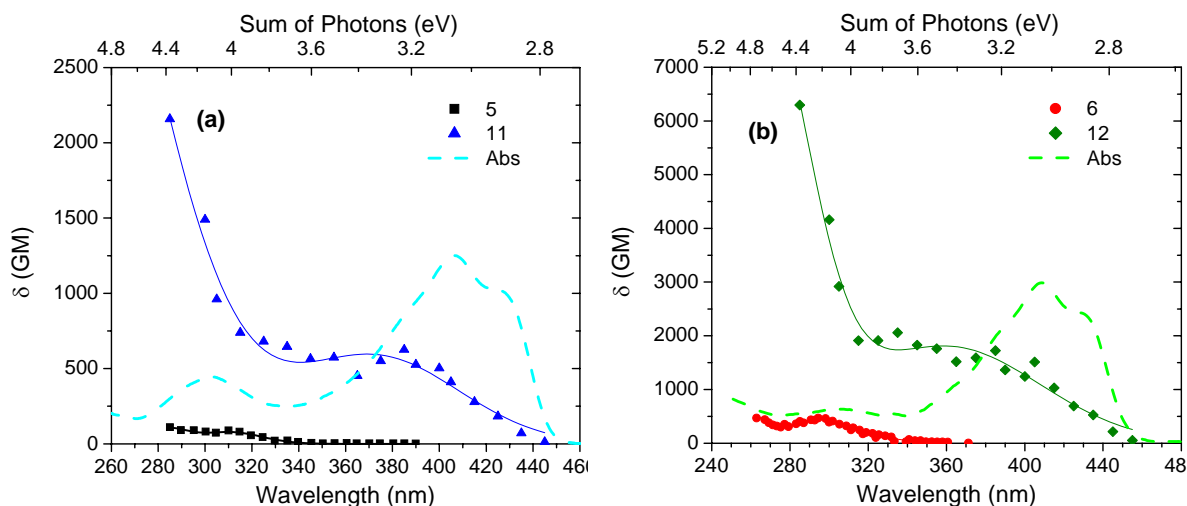


Figure 5.15: Experimentally determined 2PA spectra for (a) molecules **5** and **11** in hexane and (b) molecule **6** in hexane and **12** in methylene chloride. The linear absorption spectra for **11** and **12** are also shown.

These values ( $\lambda_{\text{exp}}^{\text{max}}$ ) as well as the corresponding peak 2PA cross-sections  $\delta_{\text{exp}}^{\text{max}}$  and their effective counterparts  $\delta^{\text{max}}/N$  are given in Table 5.9. It is interesting to note that although there

is no evidence of a distinct peak in the nonlinear spectra around the first excited state ( $\sim 410$  nm or 3.0 eV), there is significant two-photon character for wavelengths longer than those associated with the first two-photon allowed state. This is a clear departure from the shorter conjugated systems which possessed 2PA only in well-defined Gaussian profiles around the two-photon allowed transition.

Table 5.9: Location and magnitude of the peaks of the 2PA spectra for molecules **5**, **6**, **11** and **12** as determined experimentally (Figure 5.15) and quantum-chemically (Figure 5.16). In addition, the contribution of  $\delta$  per double bond is given as well as the peak 2PA cross-sections derived from the essential states model (Equation 2.14).  $\lambda$  is given in nm and  $\delta$  in GM units.

Molecule	Experimental			Quantum-Chemical		
	$\lambda_{\text{exp}}^{\text{max}}$	$\delta_{\text{exp}}^{\text{max}}$	$\delta_{\text{exp}}^{\text{max}}/N$	$\lambda_{\text{SOS}}^{\text{max}}$	$\delta_{\text{SOS}}^{\text{max}}$	$\delta_{\text{ESM}}^{\text{max}}$
<b>5</b>	310	89.1	29.7	307	100.1	97.5
<b>6</b>	295	468.9	156.3	276	1107.4	1400.2
<b>11</b>	285	2158.0	269.8	288	2930.8	3713.5
<b>12</b>	285	6297.5	787.2	291	2746.6	2021.6

As expected, the longer conjugated systems show considerable improvement from the shorter symmetrically substituted compounds. The donor substituted molecules exhibit the largest enhancement with  $\delta_{\text{exp}}^{\text{max}}$  growing by nearly 24 times from 90 to 2160 GM. The acceptor terminated systems also show considerable improvement increasing the peak nonlinearity from 470 to 6300 GM, a 13-fold increase. Furthermore, the trends remain the same in these elongated molecules: the electron withdrawing end-groups outperform their electron-donating counterparts. As for the effective nonlinearity per double bond (where molecules **5** and **6** have  $N=3$  and

molecules **11** and **12** show  $N=8$ ), the values of  $\delta^{\max}/N$  show a marked increase in agreement with the results for the T-type transitions in the dipolar compounds mentioned above.

Quantum-chemical calculations were performed and the degenerate 2PA spectra for both molecules were determined. The results from these calculations are shown in Figure 5.15 and the calculated spectra for **5** and **6** are shown as well. Their  $\lambda_{SOS}^{\max}$  and  $\delta_{SOS}^{\max}$  values are shown in Table 5.9.

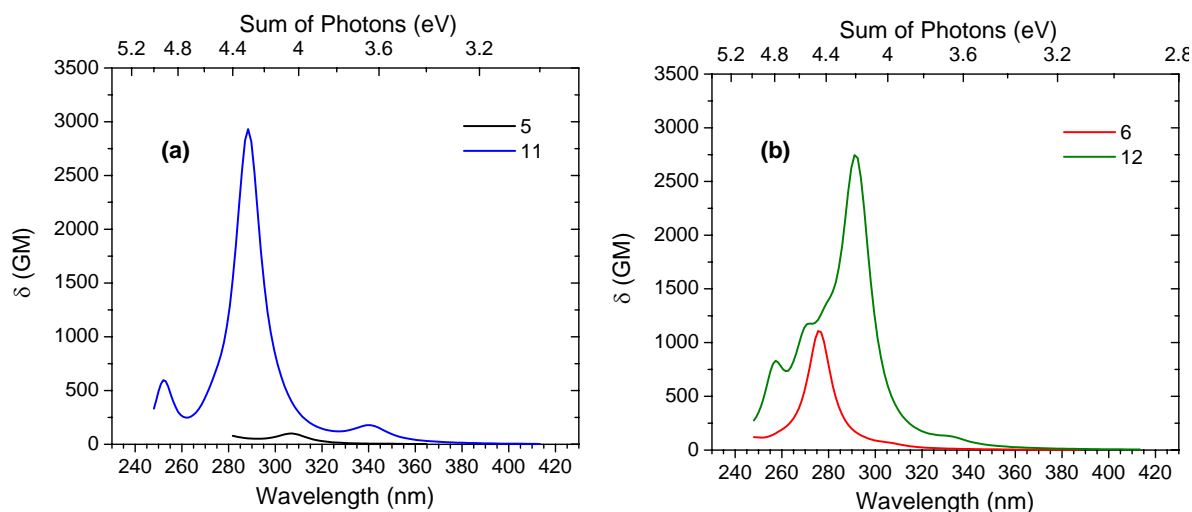


Figure 5.16: Quantum-chemically determined 2PA spectra for molecules **5**, **6**, **11** and **12** according to the methodology detailed in Section 3.5.

Interestingly, the wavelengths associated with the peaks of these spectra agree reasonably well with the peaks of the experimental spectra. Furthermore, the spectra for the longer conjugated systems both show enhancement when compared to their shorter backbone counterparts. However, while the SOS spectrum for **11** shows reasonably good quantitative agreement with the experimentally determined values, the  $\delta_{SOS}^{\max}$  value for **12** is significantly lower. In fact, the peak

nonlinearity in the donor-substituted system exceeds that of the acceptor-substituted molecule, a trend which was not observed in either the calculated or experimental spectra for the shorter systems. There is the possibility that some effects due to solvent interaction may have enhanced the experimental values of  $\delta$  associated with **12** given that it was dissolved in methylene chloride. However, this reversal of trends as conjugation length is increased would be puzzling. At this point, it is worth noting that, due to the large lengths of these molecules, size consistency issues appeared during the quantum-chemical calculations. Therefore, these results may suffer from these difficulties.

And yet, given the reasonably good correlation with the peak positions of the spectra and the trends that show enhancement for the longer conjugated systems, we approached the essential states model to gain insight into these results. Using the equation for the T term given in Section 2.3, the peak 2PA cross-sections into the first two-photon allowed state were calculated and the results are shown in Table 5.9. The trends observed from the full-converged SOS results are reproduced with the caveat that the nonlinearity for molecule **11** is somewhat overestimated. This could be a result of an overestimated value for the first excited state transition moment which appears as  $\sim 15$  D in the calculations whereas the experimentally determined value is  $\sim 12$  D (see Table 4.1). However, the real issue is that the nonlinearity for **12** is underestimated even further. To resolve this issue, we chose to look at the dominant transition dipole moments which contribute to this transition. The relevant dipole moments for these calculations (as determined quantum-chemically) are given in Table 5.10. Clearly, the dominant peaks in the SOS spectra ( $\sim 4.3$  eV) in Figure 5.16 for molecules **11** and **12** correspond to the two-photon allowed  $S_0 \rightarrow S_{13}$  and  $S_0 \rightarrow S_4$  transitions, respectively. However, each molecule shows a weaker two-photon allowed state at a lower energy ( $\sim 3.7$  eV). This could certainly provide some validation to the

longer wavelength 2PA activity which is present in the experimentally determined nonlinear spectra. Unfortunately, the calculated values using these transitions in the expression for the T term would yield values of  $\delta$  (~100 GM) which would not accurately predict those seen in the experiment. Nonetheless, it does give some credence to these observations. Finally, although the  $S_0 \rightarrow S_4$  transition has been attributed to the peak two-photon absorptivity seen in the SOS spectra for molecule **12**, Table 5.10 clearly shows that there is an equally strong two-photon transition which lays only 0.04 eV away from this transition. The value for the upper level transition moment used in the calculation of  $\delta_{ESM}^{\max}$  in Table 5.9 was 11.57 D, the value associated with  $\mu_{14}$ . However, if one assumes that these two closely-spaced states each contribute to the two-photon activity seen at the peak of the experimental spectra, the calculated value of  $\delta_{ESM}^{\max}$  becomes considerably more reasonable, i.e. 7600 GM. This is perhaps too crude an estimate, but it does reflect the trends observed experimentally. In conclusion, based on the large values of  $\delta_{\text{exp}}^{\max}$  measured for these longer conjugated systems as well as their enhanced values of effective nonlinearities, further conjugation utilizing these styryl bridges should certainly be attempted. In addition, these molecules seem to present the added advantage of exhibiting substantial two-photon activity at longer wavelengths, a factor which is always crucial in applications employing 2PA.



Table 5.10: Select quantum-chemically calculated transition energies and dipole moments for molecules **11** and **12**. These terms are used in the calculations for  $\delta_{ESM}^{\max}$  which are given in Table 5.9.

Molecule 11				Molecule 12			
Transition Energy (eV)		Transition Dipole Moment (debye)		Transition Energy (eV)		Transition Dipole Moment (debye)	
E <sub>01</sub>	3.35	$\mu_{01}$	14.88	E <sub>01</sub>	3.41	$\mu_{01}$	16.51
E <sub>02</sub>	3.64	$\mu_{12}$	6.44	E <sub>02</sub>	3.73	$\mu_{12}$	3.35
E <sub>0,13</sub>	4.30	$\mu_{1,13}$	15.86	E <sub>04</sub>	4.23	$\mu_{14}$	11.57
				E <sub>05</sub>	4.27	$\mu_{15}$	10.60

#### 5.4.2 Vinyl-Fluorene Extension

In this Section, a new avenue will be explored for conjugation extension in dipolar type compounds: vinyl-fluorene extension (vinyl group or double bond followed by a repeated fluorene unit). Molecules **13**, **14** and **15** represent modifications to the dipolar systems studied in Section 5.2 with this vinyl-fluorene unit preceding the electron withdrawing terminal group. Molecules **13** and **14** have benzothiazole and nitro groups attached to this bridge, respectively, while **15** appends an additional styryl group prior to its terminal benzothiazole unit. The 2PA spectra for these compounds in hexane are shown in Figure 5.17. All of these spectra were acquired using the WLC pump-probe technique with a pump wavelength of 750 nm. Noting the locations for the first maxima of the nonlinear spectra given by  $\lambda_{\text{exp}}^{\max}$  in Table 5.11, we can see that these peaks correlate quite well with the  $S_0 \rightarrow S_1$  transitions identified by the maxima of the linear absorption spectra shown in Table 4.1. In fact, the slight red-shifting of the linear

spectrum for compound **14** (nitro end-group) with respect to the two other systems is also reproduced in the nonlinear spectra. As discussed previously, these trends are typical of dipolar systems. Unfortunately, unlike the styryl-extended dipolar systems in the previous Section, no definitive peaks could be identified for what would normally be considered the  $S_0 \rightarrow S_2$  transition at  $\sim 300$  nm. Furthermore, due to the nature of the nondegenerate measurement used to acquire these spectra, these values into the upper lying excited state have been artificially enhanced (see Chapter 6). For this reason, analysis of this higher lying two-photon state will not be undertaken.

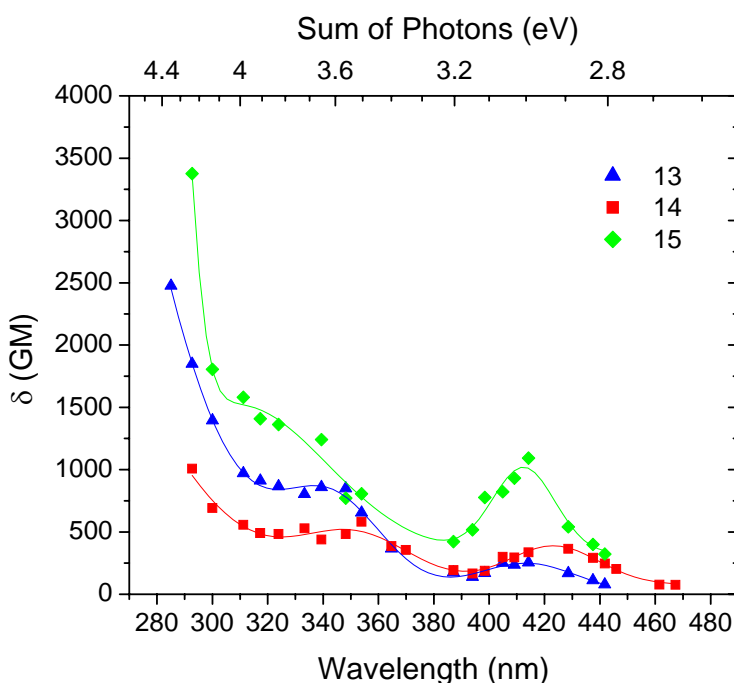


Figure 5.17: Experimentally determined 2PA spectra for molecules **13**, **14** and **15** in hexane.

Interestingly, each molecule's spectrum shows a somewhat pronounced peak at an intermediate energy ( $\sim 3.65$  eV) between the  $S_1$  and what would typically be considered the  $S_2$  state. In fact, along these lines, the functions which showed the optimal fitting to the

experimental data points were actually three-peaked Gaussians. An intermediate two-photon allowed state, like this, would be reminiscent of the longer conjugated symmetrically end-capped systems studied in the previous Section. Unfortunately, without the aid of supplemental quantum-chemical data (which was unavailable at the time of analysis), this assertion is difficult to support.

Table 5.11: Location and magnitude of the peaks of the 2PA spectra into the  $S_1$  state for molecules **13**, **14** and **15** as determined experimentally (Figure 5.17).  $\lambda$  is given in nm and  $\delta$  in GM units. In addition, the contribution of  $\delta$  per double bond is given. Data for molecules **3** and **9** are shown for a reference.

Molecule	$S_0 \rightarrow S_1$		
	$\lambda_{\text{exp}}^{\text{max}}$	$\delta_{\text{exp}}^{\text{max}}$	$\delta_{\text{exp}}^{\text{max}}/N$
<b>3</b>	387	71.2	23.7
<b>9</b>	385	183.0	33.3
<b>13</b>	414	254.5	36.4
<b>14</b>	429	365.1	52.2
<b>15</b>	414	1093.3	115.1

In addition to the values of  $\lambda_{\text{exp}}^{\text{max}}$  mentioned above, Table 5.11 summarizes the peak 2PA cross-sections  $\delta_{\text{exp}}^{\text{max}}$  for the  $S_0 \rightarrow S_1$  transition as well as their effective cross-sections  $\delta^{\text{max}}/N$ . Data for molecules **3** and **9** are shown as a reference. Once again, there exists a definitive enhancement in the nonlinearity for these longer conjugated dipolar molecules when compared to the shorter model compound **3**. An initial comparison can be made between molecules **3**, **9** and **13** since they possess identical withdrawing moieties. The peak 2PA cross-sections clearly increase as the overall conjugation length of the molecule increases: **13** possesses a longer

backbone than **9**, which itself is longer than the model compound **3**. While the increase in the nonlinearity due to the styryl extension was attributed to an augmented value for  $\Delta\mu_{01}$  in **9** (see the previous Section), inspection of the experimentally determined values for the first transition moment  $\mu_{01}$  (given in Table 4.1) reveals that this factor probably plays the largest role in the enhancement for molecule **13**: molecule **13** shows a value of over 13 D while the two other compounds are  $\sim 8$  D. This argument is supported by the quadratic dependence of  $\mu_{01}$  in the expression for the dipolar term associated with these transitions (see Section 2.3). Nonetheless, when taking into account the number of conjugating double bonds involved (3 for molecule **3**, 5.5 for molecule **9**, and 7 for **10**), the contributed nonlinearity per double bond remains relatively constant for all three molecules. This indicates that while the peak nonlinearity is large in this vinyl-fluorene derivative, conjugation extension in this manner is not necessarily more efficient.

The replacing of the benzothiazole group in **13** with a stronger accepting nitro group in **14** leads to an enhanced value for  $\delta_{\text{exp}}^{\text{max}}$  by nearly 1.5 times. This is in contradiction with the findings in Section 5.2.1 for the shorter dipolar molecules which showed that appending this stronger acceptor group actually decreased the nonlinearity. Given the discrepancy between the values of  $\mu_{01}$  for these two molecules (**13** shows a value over twice as large as that of **14**), the enhancement in the nonlinearity for **14** must assuredly be a result of a much larger value for  $\Delta\mu_{01}$  compared to **13**. One could therefore argue that, when revisiting the dipolar curve in the BOA versus  $\gamma$  plot (Figure 5.3), the optimum value of ground-state modulation for this extended molecule has been shifted with respect to the shorter conjugated systems and thus occurs when the stronger withdrawing group is present. Again, this claim could be supported given thorough quantum-chemical analysis of these systems. Finally, molecule **15** with its additional styryl group compares quite favorably to molecule **13** which possesses a shorter conjugated backbone.

It shows a peak cross-section of over four times that of **13** and a 15 times enhancement compared to the model compound **3**. While a larger value of  $\mu_{01}$  certainly plays a role in this enhancement with respect to **3**, these values of the first transition moment for **13** and **15** are nearly identical. Therefore, this enhancement must result from a larger value of  $\Delta\mu_{01}$ . Moreover, if one compares molecules **3** and **9** one determines the enhancement factor due to styryl extension: 2.5 times. Comparing **3** and **13** gives the vinyl-fluorene enhancement factor: 3.5 times. Yet, the factor of over 15 times enhancement when comparing **3** to **15** is greater than the product of these two factors ( $2.5 \times 3.5 = 8.75$ ). Obviously, the use of the two conjugation avenues in series provides some type of cooperative enhancement of the nonlinearity. This is evidenced in the large value of  $\delta^{\max}/N$  which is directly linked to two-photon efficiency of the molecule. In conclusion, this analysis shows that as conjugation length is increased along the main backbone, independent of the conjugation route taken, the peak nonlinearity into  $S_1$  intensifies. However, there is no strong evidence that vinyl-fluorene extension is favored over styryl extension in terms of two-photon efficiency. On the other hand, use of these structures in conjunction with one another offers a large increase in terms of contributed nonlinearity per double bond. Future work should certainly involve the use of these two avenues to synthesize longer chain molecules in order to determine a true relationship between conjugation length and nonlinearity. Two-photon activity into higher lying states might also promise enhanced nonlinearities.

### 5.4.3 Amino-Fluorene Extension

The molecular systems discussed in this Section involve a series of symmetrical diphenylaminofluorene-based chromophores. These elongated systems are based on the model

D- $\pi$ -D compound number **5**. Molecules **16** and **17** are oligomer and polymer versions of this molecule, respectively, where repeated fluorene chromophore units linked via phenylamine groups have been incorporated between the diphenylamine end-groups. This repeat unit can be seen in the chemical structure for **17** in Figure 4.3. The 2PA spectra for these compounds in hexane are shown in Figure 5.18. The nonlinear spectrum for molecule **5** is given as a reference. The spectra for all of these molecules were acquired using the 2PF technique. In addition, the linear absorption spectrum for **17** is also plotted. Molecule **16**'s linear spectrum is nearly identical to that of **17** and has therefore been omitted. This brings up the important point that upon full review of the linear photophysical properties of these compounds [77,78], it was concluded that these properties were nearly independent of the number of fluorenyl units in a molecule. This suggested a weak interaction between chromophores, with minimal perturbation of their electronic levels. This is not surprising given the fact that the phenylamine linking group should be quite effective in preventing conjugation of the entire molecular chain. Therefore, technically, this series of molecules does not represent a true extension of the conjugation length of the molecule. Nevertheless, given that poly(fluorene)-based materials are of particular interest due to their thermal and chemical stability, along with desirable photoluminescence and electroluminescence properties, this series is still of interest.

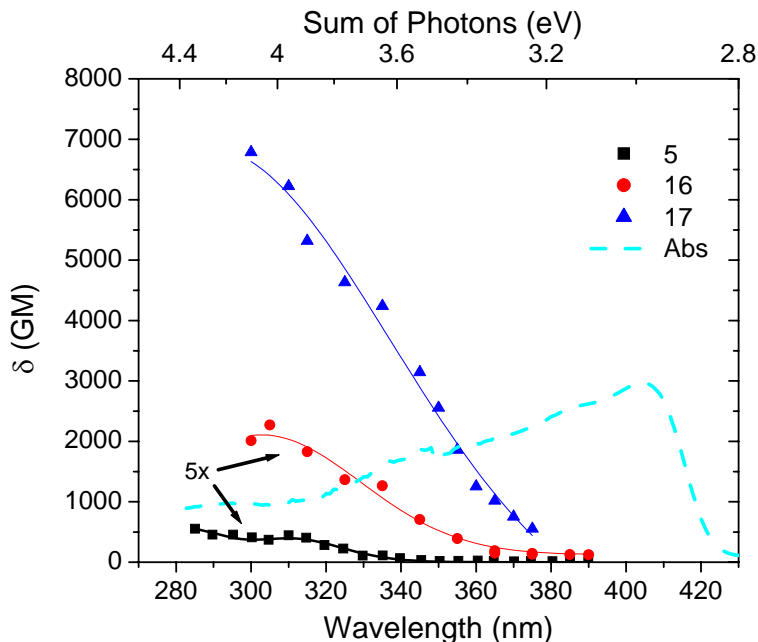


Figure 5.18: Experimentally determined 2PA spectra for molecules **5**, **16** and **17** in hexane. The linear absorption spectrum for **17** is also shown. The nonlinear spectra for **5** and **16** have been magnified for ease of viewing.

The locations of the maxima of the nonlinear spectra are given by  $\lambda_{\text{exp}}^{\text{max}}$  in Table 5.12. These positions seem to indicate that the observed 2PA correlates with the  $S_0 \rightarrow S_2$  transitions in these molecules. This observation was confirmed through analysis of their steady-state anisotropy spectra. As always, Table 5.12 summarizes the peak 2PA cross-sections  $\delta_{\text{exp}}^{\text{max}}$  and their corresponding effective cross-sections  $\delta^{\text{max}}/N$  for this transition as well. As expected, the peak 2PA increases with the number of repeated chromophore units in the molecule culminating with a substantial peak cross-section of nearly 7,000 GM for the polymeric system. The contributed nonlinearity per double bond also seems to increase as well, although at a much slower rate (since each fluorene chromophore gives a value of  $N=3$ , molecules **5**, **16**, and **17** have values of 3, 9, and 48, respectively). Given the non-conjugated nature of these molecular

backbones, one would expect the effective nonlinearity to remain constant, independent of the number of repeat units. Although this does not strictly seem to be the case, one can immediately see the difference when looking at the value of  $\delta^{\text{max}}/N$  for molecule **11**. This molecule (also a symmetric D- $\pi$ -D system) is much shorter in length than either **16** or **17** and yet possesses an effective nonlinearity of nearly 270 (see Table 5.9). This is a result of the conjugated nature of its backbone. A recent study by Najechalski *et al.* [103] reported the characterization of the 2PA spectrum of a poly(fluorene) molecule with 60 repeat units. Given that the fluorene chromophores in this study were linked directly at the 7 position of the molecules (see Figure 4.1), the authors claim that the entire system is effectively conjugated. In fact, they present evidence that, up to N=12 repeat units (due to the saturation effect mentioned at the outset of Section 5.4), the value of  $\delta^{\text{max}}$  increases quadratically with N. Although these results should be taken with caution since the authors used nanosecond excitation which can be known to induce excited-state absorption and thereby artificially magnify the measured value of  $\delta$ , the observations are consistent with a true conjugated system. In conclusion, the peak nonlinearity for a series of diphenylaminofluorene-based chromophores shows definitive increase with the number of repeat units in the molecule. And, while there is not a significant gain in the effective nonlinearity, the peak value of 2PA in the longest chain molecule is quite substantial.



Table 5.12: Location and magnitude of the peaks of the 2PA spectra into the  $S_1$  state for molecules **16** and **17** as determined experimentally (Figure 5.18).  $\lambda$  is given in nm and  $\delta$  in GM units. In addition, the contribution of  $\delta$  per double bond is given. Data for molecule **5** is shown for a reference.

Molecule	$S_0 \rightarrow S_2$		
	$\lambda_{\text{exp}}^{\text{max}}$	$\delta_{\text{exp}}^{\text{max}}$	$\delta_{\text{exp}}^{\text{max}} / N$
<b>5</b>	310	89.1	29.7
<b>16</b>	305	454.3	50.5
<b>17</b>	300	6786.0	141.4

## 5.5 Multi-branched Molecules

The molecules which we have investigated up until now have possessed linear type architectures. In these quasi one-dimensional systems, the charge transfer that occurs following excitation takes place along the linear conjugated backbone of the molecule. In this Section, we investigate the consequences that moving to a two-dimensional type geometry has on the two-photon absorbing capability of two molecules. This is made possible by the ability to functionalize the fluorene chromophore on its 4 position (see Figure 4.1). The two compounds under investigation are compounds **18** and **19** which bear a strong resemblance to the structure of **11** (which itself is an analog of molecule **5**) that has di-substituted styryl groups preceding its terminal groups. Molecule **18** is identical to **11** with the distinction of an additional diphenylamine end-capped styryl bridge protruding from position 4. Compound **19** moves to a more dendrimeric topology by appending three separate sub-structures (i.e., compound **11**) to its base; this is done via a vinyl group from positions 2, 4 and 7.

The 2PA spectra for these two compounds in cyclohexane are shown in Figure 5.19. These spectra were acquired using the 2PF technique. The nonlinear absorption spectra for molecules **5** and **11** are given for reference. In addition, the linear absorption spectrum for **18** is also plotted. The linear spectra for **11** and **19** are quite similar to this and therefore will not be shown.

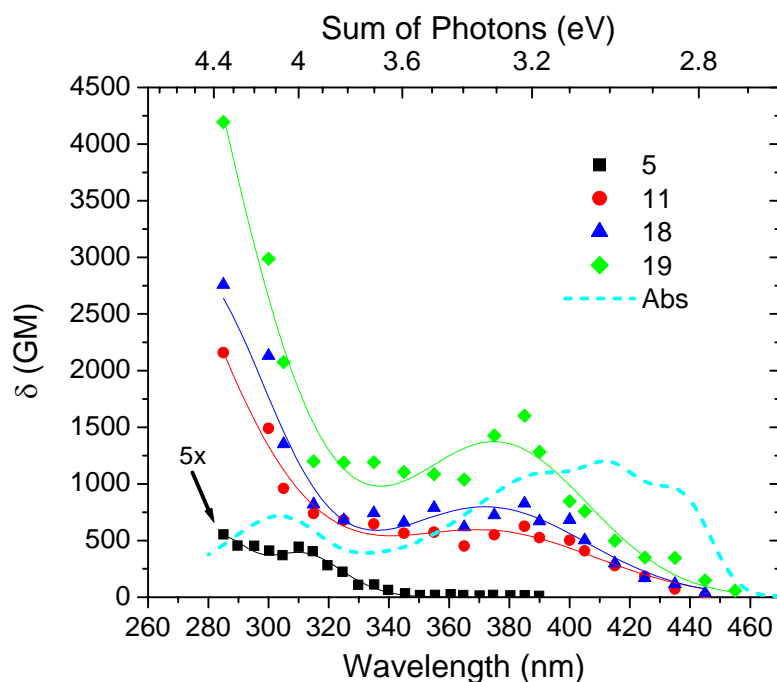


Figure 5.19: Experimentally determined 2PA spectra for molecules **11**, **18** and **19** in cyclohexane while **5** is in hexane. The linear absorption spectrum for **18** is also shown. The nonlinear spectrum for **5** has been magnified for ease of viewing.

The contours of the spectra for **18** and **19** behave rather similarly to **11** as one might expect. The dominant 2PA in these molecules seems to be accessing higher lying two-photon active states. Since the peaks of these transitions can not be clearly identified,  $\lambda_{\text{exp}}^{\text{max}}$  will be identified by the highest energy data point. These values, as well as their corresponding peak 2PA cross-sections

$\delta_{\text{exp}}^{\text{max}}$ , are given as the  $S_0 \rightarrow S_2$  data in Table 5.13. As the branched structures grow in complexity so does the nonlinearity. The effect of appending the styryl diphenylamine in **18** produces a roughly 30 percent increase in the peak 2PA cross-section compared to **11**. The ground to first excited state transition moments determined experimentally account for this enhancement rather well (12.24 D for **11** and 14.54 D for **18**). Given this strong correlation and assuming that use of the T term from the essential states analysis is valid, one can assume that there is negligible contribution to this enhancement from the higher lying transition moment  $\mu_{12}$ . This would imply that moving to a higher dimensionality does not necessarily increase the efficiency of charge transfer in the excited state. Moving to molecule **19**, we notice similar results. First of all, the peak molar absorptivity for this molecule (see Table 4.1) is roughly three times that of **11** which, given the nature of the three appended branches, is not surprising. This gives a value of  $\mu_{01}$  almost exactly twice that of **11**, which should imply (given the quadratic nature of this term in the essential states analysis) a four-fold increase in nonlinearity. However, the peak nonlinearity only shows a roughly, two-fold enhancement suggesting that perhaps this is a result of a sacrifice in the strength of  $\mu_{12}$  for this higher-dimensionality system. Nonetheless, similar results have been observed for a series of triphenylbenzene dendritic chromophores [104]. In this study, the second generation dendrimer (three units), while showing a three-fold increase in peak molar absorptivity compared to the first generation analogue (one unit), showed only a two-fold increase in its peak 2PA cross-section.

Table 5.13: Location and magnitude of the peaks of the 2PA spectra into the  $S_2$  and  $S_1$  states for molecules **11**, **18** and **19** as determined experimentally (Figure 5.19).  $\lambda$  is given in nm and  $\delta$  in GM units. Data for molecule **5** is shown for a reference.

Molecule	$S_0 \rightarrow S_2$		$S_0 \rightarrow S_1^*$	
	$\lambda_{\text{exp}}^{\text{max}}$	$\delta_{\text{exp}}^{\text{max}}$	$\lambda_{\text{exp}}^{\text{max}}$	$\delta_{\text{exp}}^{\text{max}}$
<b>5</b>	310	89.1	385	17.5
<b>11</b>	285	2158.0	385	625.9
<b>18</b>	285	2759.0	385	827.7
<b>19</b>	285	4194.0	385	1603.0

It is interesting to note that as the role of dimensionality increases, there seems to be a growing contribution in the two-photon activity around 385 nm (or 3.2 eV). This is quantified in Table 5.13 where the 2PA cross-sections corresponding to this wavelength are tabulated for all four of the molecules studied in Figure 5.19. Observing the linear absorption spectrum, this wavelength seems to correspond to the first vibrational overtone of the  $S_0 \rightarrow S_1$  transition (indicated by the shoulder in the curve). In fact, it has been shown that vibronic coupling can be quite strong in multi-branched structures [105]. Indeed, one sees that in the short conjugated system **5**, with well defined symmetry along its backbone, there is negligible 2PA at this wavelength as expected for a two-photon forbidden state. However, as the molecular structure departs from this linear one-dimensional system, this high level of symmetry breaks down and well-defined parity no longer exists for the electronic wavefunctions. Therefore, one and two-photon absorption should be allowed equally into all transitions. This would certainly account for the fact that the two-photon activity into  $S_1$  increases as the molecules depart from this well-defined symmetry. In fact, the dendrimer type molecule **19** shows a significant nonlinearity into

this state,  $\sim 1600$  GM. This could provide a plausible explanation for the lack of enhancement noticed for this molecule into the  $S_2$  state as the oscillator strengths in the molecular system are most likely redistributed. Finally, we should note that this significant two-photon character for longer wavelengths was noted previously for molecule **11** and was attributed to an additional two-photon allowed state with the aid of quantum-chemical calculations. However, given the results presented here, there is a possibility that this increased two-photon activity is a result of increased dimensionality as well. This could be due to conformational changes or intramolecular torsion in the molecule which is not uncommon in molecules that possess styryl chains [94]. This would explain the identical trend which was observed in molecule **12**, another longer styryl conjugated system. In conclusion, although the molecules with increased dimensionality do not necessarily exhibit greater charge transfer which would lead to more effective nonlinearities, they still hold two distinct benefits: an increase in the overall magnitude of two-photon activity as well as an increased spectral band of useable nonlinearity.

## **5.6 Resonance Enhancement**

Until now, in the context of the essential states model we have concentrated on the effects the magnitudes of transition dipole moments have on the strength of 2PA. Other than a brief mention in Section 5.4.1, the other governing element in this analysis, the detuning energy, has been largely ignored. As discussed in Section 2.4.2, the detuning energy plays a crucial role in the T-type term of the essential states analysis (see Equation 2.14) and is basically the energy difference between that of an incident photon and the first excited state. When investigating degenerate 2PA into the peak of the first two-photon allowed state, this expression becomes

$$\frac{(\hbar\omega_{e'g}/2)^2}{(\hbar\omega_{eg} - \hbar\omega_{e'g}/2)^2} \quad 5.4$$

where  $\hbar\omega_{eg}$  is the energy of the first excited state and  $\hbar\omega_{e'g}$  is the energy of the two-photon excited state. Given that 2PA is being analyzed into the peak of the two-photon allowed transition, the incident photon energy has the relation  $\hbar\omega \approx \hbar\omega_{e'g}/2$  and the effective detuning is given by  $\hbar\omega_{eg} - \hbar\omega_{e'g}/2$ . Therefore, the means to exploit this term is found in the ability to reduce or red-shift  $\hbar\omega_{eg}$  such that it approaches  $\hbar\omega_{e'g}/2$ ; as a result of this, Equation 5.4 becomes resonantly enhanced. Work devoted to exploiting this condition for the purpose of maximizing a molecule's 2PA properties has been promising and yet limited in its scope. Pati [106] used conformational changes in a group of dipolar compounds to effectively alter the detuning energy to reach this resonance enhancement. Kogej [23] and Zojer [22] explored the possibilities of this enhancement in dipolar and quadrupolar systems, respectively, by altering the ground-state polarization, which in turn gave rise to a smaller detuning energy. Each of the previous groups utilized quantum chemical analysis for their studies. In contrast, Drobizhev [107] and Kamada [108] showed experimental evidence of this enhancement process in substituted porphyrin systems and symmetric substituted diacetylenes, respectively.

This condition of resonance enhancement has been ignored in this study of fluorene derivatives, so far, due to the resiliency of their electronic energy positions as their chemical structures are altered. Specifically, the energy of the  $S_0 \rightarrow S_1$  transition remains quite steadfast, rarely varying by more than 20 nm (see Table 4.1) and certainly showing no substantial red-shift. In an attempt to exploit this resonance condition, molecule **20** was synthesized. This derivative is a methylated salt, a direct analog of the third molecule in this series. Therefore, the route we have chosen is similar to that employed by Kogej [23], where the detuning energy is reduced in

dipolar systems. Consequently, the enhancement should benefit the second excited state in a non-centrosymmetric system in a context similar to that discussed for the styryl extended dipolar compounds in Section 5.4.1. The linear absorption spectrum for **20** in THF is presented in Figure 5.20 along with the linear spectrum for **3** in hexane as a reference. The use of the slightly polar solvent THF was a necessity due to solvency issues.

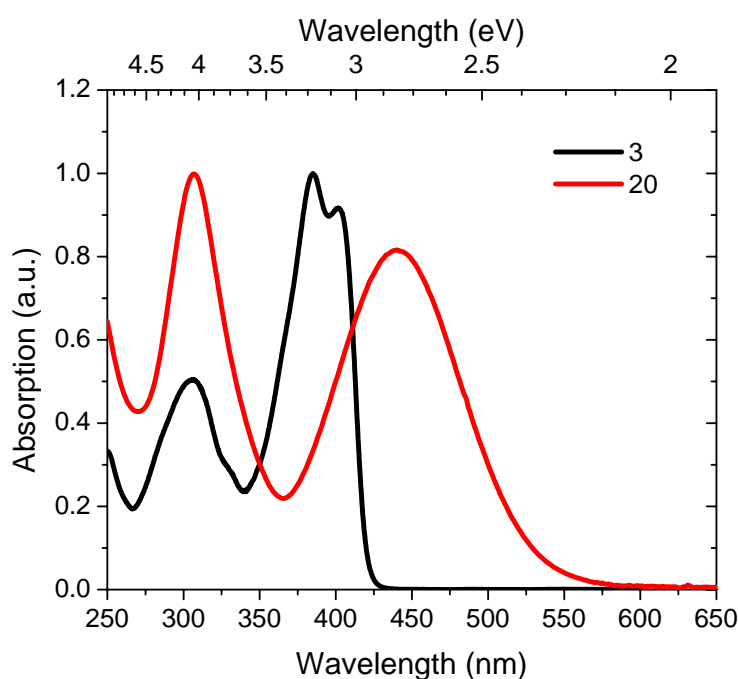


Figure 5.20: Linear absorption spectra for molecules **3** and **20**. Molecule **3** is dissolved in hexane and **20** in THF.

Judging by the values of  $\lambda_{abs}^{max}$  given for these two compounds in Table 4.1, one can see that over a 50 nm shift in the  $S_0 \rightarrow S_1$  transition was achieved via methylation of compound **3** (the peaks are 385 and 440 nm for molecules **3** and **20**, respectively). Also, quite fortuitously perhaps, the peak positions of the  $S_0 \rightarrow S_2$  transitions for the two molecules are identical (307 nm), implying

that the differences in detuning energies between the two systems will be given strictly by the disparity in their  $S_0 \rightarrow S_1$  transition energies.

The 2PA spectra for the two molecules are shown in Figure 5.21. The spectrum for **3** was acquired via the 2PF method (Figure 5.4). Since molecule **20** exhibited negligible fluorescence, the WLC pump-probe method was employed to acquire the nonlinear spectrum. Two separate experiments were performed to acquire quasi-degenerate 2PA spectra for excitation into the two separate bands: for excitation into the  $S_1$  band a pump wavelength of 750 nm was used, whereas for  $S_0 \rightarrow S_2$  transition a 600 nm pump wavelength was employed. These two measurements allow for direct comparison with the true degenerate 2PA data plotted for molecule **3**.

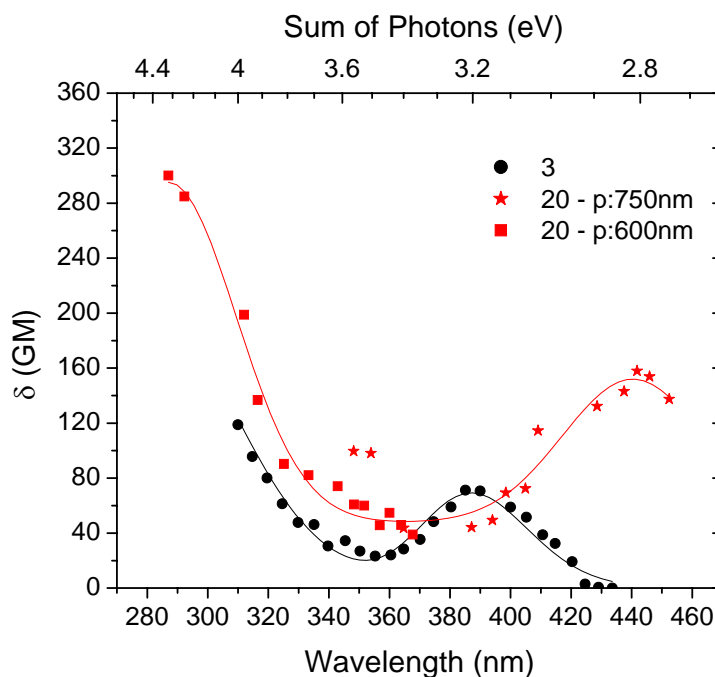


Figure 5.21: Experimentally determined 2PA spectra for molecule **3** in hexane and **20** in THF. The nonlinear spectrum for **3** was acquired using the 2PF method. For **20** the WLC pump-probe technique was employed using two different pump wavelengths to provide excitation into both bands,  $S_1$  (p: 750 nm) and  $S_2$  (p: 600 nm).



Noting the locations for the first maxima of the nonlinear absorption spectra given by  $\lambda_{\text{exp}}^{\text{max}}$  in Table 5.14, one notes that the peaks correlate quite well with the  $S_0 \rightarrow S_1$  transitions as identified by the maxima of the linear absorption spectra shown in Table 4.1. This is, of course, quite typical for dipolar compounds. In addition, Table 5.14 summarizes the peak 2PA cross-sections  $\delta_{\text{exp}}^{\text{max}}$  for this transition as well. Molecule **20** shows nearly a two-fold increase for the nonlinearity into this state compared to **3** despite showing similar values for the transition dipole moments ( $\mu_{01}$ ) associated with these states (see Table 4.1). Therefore, this is most likely due to an enhancement in the change in state dipole moments ( $\Delta\mu_{01}$ ) for **20**. Furthermore, one should note that the data taken with the two different pump wavelengths agree rather well in the region of overlap between their two respective spectra (i.e.,  $\sim 360$  nm). This gives confidence in their final results. The two data points laying at  $\sim 350$  nm, as acquired by the 750 nm pump geometry, show enhancement compared to the other curve (p: 600 nm) which is not unexpected given the nondegenerate nature of the excitation in this region.

Table 5.14: Location and magnitude of the peaks of the 2PA spectra into the first two excited states for molecules **3** and **20** as determined experimentally (Figure 5.21).  $\lambda$  is given in nm and  $\delta$  in GM units.

Molecule	$S_0 \rightarrow S_1$		$S_0 \rightarrow S_2$	
	$\lambda_{\text{exp}}^{\text{max}}$	$\delta_{\text{exp}}^{\text{max}}$	$\lambda_{\text{exp}}$	$\delta_{\text{exp}}$
<b>3</b>	387	71.2	314	95.6
<b>20</b>	442	158.0	312	198.9

Nevertheless, we are mainly concerned with how 2PA into the  $S_0 \rightarrow S_2$  transition is affected by the decreased detuning energy. By the peaks in the linear absorption spectra, this transition was previously identified to lie at 307 nm for both molecules. Figure 5.21 shows clear evidence of two-photon excitation into this  $S_2$  state. Given that neither nonlinear spectrum shows distinct peaks into this state, the wavelength chosen for comparison corresponds to the shortest wavelength data value available for molecule **3**. This is reflected in Table 5.14 where the values for  $\lambda_{\text{exp}}$  along with the associated values for  $\delta_{\text{exp}}$  are given. It should be noted that although data for molecule **3** dissolved in THF was also available for comparison (see Figure 5.7), the plot shows no data acquired for 2PA into the higher lying excited state and therefore it would not be applicable in this context. Given the negligible enhancement shown between molecule **3** in Hexane and THF, we believe using the data from the former solvent is justified. Returning to Table 5.14, there is a 2.1 times enhancement in the nonlinearity for **20** compared to **3**. To determine whether this enhancement is justified by the decreased detuning energy, the terms associated with Equation 5.4 are shown in Table 5.15. The values of  $\hbar\omega_{eg}$  and  $\hbar\omega_{e'g}/2$  were determined directly from the linear absorption spectra. One immediately sees that the ratio between the final detuning terms shows an enhancement of 2.25 times for molecule **20** in good agreement with the experimental results quoted above. This lends credence to the possibility that resonance enhancement, through the red-shifting of the linear absorption spectrum for **20**, indeed occurs. However, it is important to note the other factors which may play a role in this enhancement of the nonlinearity into  $S_2$ . Although the transition dipole moments associated with the first excited state ( $\mu_{01}$ ) between the two molecules are nearly identical, without the benefits of quantum-chemical analysis we cannot comment on the relative magnitudes of their higher lying transition moments ( $\mu_{12}$ ). Since these values certainly play a role in the possible

enhancement in this state, it is difficult to determine the precise impact of resonance enhancement. Nonetheless, there is an unmistakable decrease in the detuning energy for **20** which must assuredly play a role in the enhancement. At this point, one should note that, since it is the peak positions of the transitions which are entered into the expression for the detuning term (Equation 5.4), any residual linear absorption red-shifted beyond this peak position will only serve to weaken the effect of resonance enhancement. Therefore, in order to effectively exploit this condition in the future, molecules whose absorption bands exhibit sharp features on their low-energy sides should be sought. Similar conclusions for dipolar stilbene derivatives were found by Kogej [23].

Table 5.15: The appropriate terms for Equation 5.4 for molecules **3** and **20** as determined from their linear absorption spectra in Figure 5.20.

<b>Molecule</b>	$\hbar\omega_{e'g}/2$	$\hbar\omega_{eg}$	$\frac{(\hbar\omega_{e'g}/2)^2}{(\hbar\omega_{eg} - \hbar\omega_{e'g}/2)^2}$
<b>3</b>	2.02	3.22	2.83
<b>20</b>	2.02	2.82	6.37

## CHAPTER 6: INTERMEDIATE STATE RESONANCE ENHANCEMENT

The previous Chapter detailed the chemical structure – NLO property relationships for the series of fluorene molecules investigated in this dissertation. For the sake of consistency, all of the nonlinear spectra reported were essentially degenerate in nature. For the cases where the nondegenerate WLC pump-probe technique was employed, the pump photon energy was chosen such that it coincided with the peak of the D-2PA spectrum (Section 3.3.1). This produced a spectrum that was quasi-*degenerate* and which showed negligible discrepancies with the D-2PA spectrum. However, in this Chapter, the true nondegenerate capability of this technique will be used to enhance the two-photon absorption observed in certain molecules by exploiting the condition of resonance enhancement. This is in direct contrast to the previous Section where the electronic properties of the molecule had to be tuned to observe this enhancement whereas, here, the nature of the process used to generate 2PA itself is responsible for the observed improvement.

In order to properly elucidate this phenomenon, it is helpful to return to the arguments laid out in Section 2.4.2 regarding the detuning energy. In particular, we will be concerned with the case where one of the incident photons approaches a resonance with the lowest one-photon allowed state, a condition which will henceforth be referred to as intermediate state resonance enhancement (ISRE). In this previous Section, the focus was placed on degenerate 2PA (D-2PA), a process in which the sample simultaneously absorbs two photons of identical or degenerate energies. Since D-2PA into the two-photon allowed excited state  $|e'\rangle$  of the molecule

was studied ( $E_{ge} \approx 2\hbar\omega$ ), resonance enhancement was achieved if the energy of the molecule's lowest lying one-photon allowed state  $|e\rangle$  approached half the energy of the two-photon state (i.e.  $E_{ge} \rightarrow E_{ge}/2$ ). Therefore, in order to investigate the effect of this resonance condition, several molecules with slightly different chemical structures (and hence slightly different energy levels) would have to be studied. It is difficult to ascertain the value of enhancement of 2PA specifically due to resonance in these cases since altering a molecule's structure to satisfy the above condition will inevitably alter its other optical properties (e.g., state and transition dipole moments). This is precisely the problem which was addressed at the end of Section 5.6 and is a problem in any experimental study of ISRE in organics (see, for example, References 107 and 108). If, instead of altering the position of the first excited state (i.e.,  $E_{ge} \rightarrow \hbar\omega$  for  $\omega$  held constant), the photon energy is adjusted to approach resonance (i.e.,  $\hbar\omega \rightarrow E_{ge}$  for  $E_{ge}$  held constant), the effect of resonance enhancement on 2PA could be studied directly.

In this Chapter, the process of nondegenerate 2PA (ND-2PA) is employed which permits one to vary the energies of the individual photons,  $\hbar\omega_1$  and  $\hbar\omega_2$ , while keeping the two-photon energy,  $\hbar(\omega_1 + \omega_2)$ , constant. This allows one to vary the detuning from the intermediate state while accessing the same final states. In this way, quantitative study of the effect of ISRE in a single molecule can be determined. Through the direct investigation of ISRE afforded by this route, greater insight into the nature of resonance enhancement can be gained. Furthermore, evidence of significant enhancement suggests promising applications using ND-2PA. We note here that the majority of following content found in this Chapter is primarily taken from Reference 109. The first Section of this Chapter is devoted to the degenerate and nondegenerate 2PA spectra acquired for two of the fluorene molecules involved in this study: molecules **3** and **5**. In addition, the theoretically determined spectra from the fully-converged SOS analysis are

shown for comparison. Lastly, Section 6.2 develops the essential states model for ND-2PA and uses the results to provide intuitive insight into the process of ISRE for ND-2PA.

## **6.1 Two-Photon Absorption Spectra**

Molecules **3** and **5** were chosen for this study since they represent model compounds for many of the derivatives studied in this dissertation. As such, a significant amount of the conclusions drawn from their results should be applicable towards these other systems. Furthermore, these systems show distinct structural differences given that **3** is an asymmetric D- $\pi$ -A molecule whereas **5** is a symmetric D- $\pi$ -D molecule. This fact imparts great flexibility in the study of ISRE by ND-2PA since **5** permits study of nonlinear absorption into its first two-photon allowed state only whereas **3** permits investigation of 2PA into both of its lowest electronic states by virtue of their mixed parity.

### **6.1.1 Experimentally Determined Spectra**

Schematic representations of the 2PA spectroscopy experiments carried out on molecules **3** and **5** are shown in Figures 6.1 and 6.2, respectively. The former illustrates 2PA into the first excited state of the D- $\pi$ -A molecule whereas the latter denotes 2PA into the first two-photon allowed state of the D- $\pi$ -D molecule.

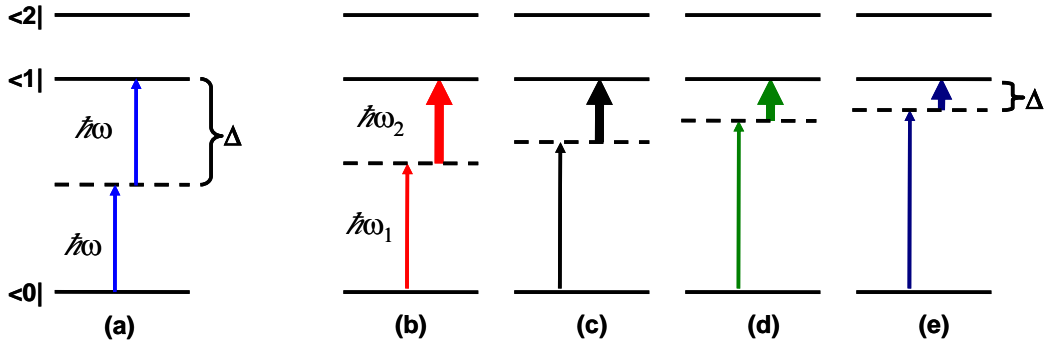


Figure 6.1: Schematic representation of experiments performed for 2PA into the first excited state of molecule **3**. Figure (a) shows the D-2PA measurement (2PF) whereas figures (b)-(e) show ND-2PA (WLC); in the latter cases,  $\hbar\omega_1$  represents the probe photons and  $\hbar\omega_2$  the pump photons. The exact photon energies for each experiment are given in Table 6.1.

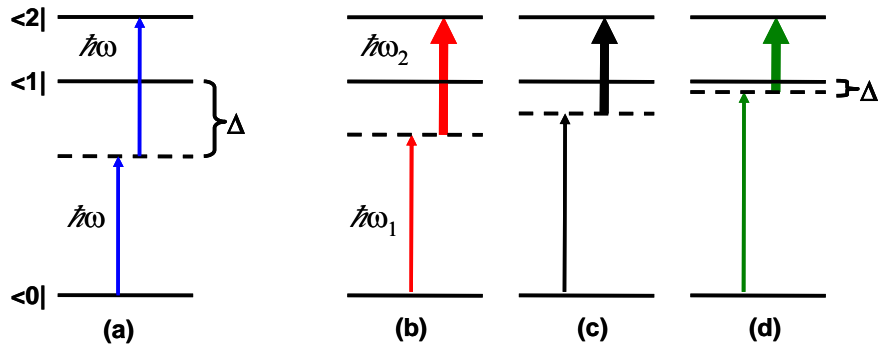


Figure 6.2: Schematic representation of experiments performed for 2PA into the first excited state of molecule **5**. Figure (a) shows the D-2PA measurement (2PF) whereas figures (b)-(d) show ND-2PA (WLC); in the latter cases,  $\hbar\omega_1$  represents the probe photons and  $\hbar\omega_2$  the pump photons. The exact photon energies for each experiment are given in Table 6.2.

Figures 6.1a and 6.2a schematically describe the degenerate 2PA (D-2PA) experiments, which were carried out by the 2PF method. The remaining Figures (6.1b-e and 6.2b-d) denote nondegenerate 2PA (ND-2PA), as studied in the WLC pump-probe experiment. For the nondegenerate case, index 1 represents the probe photons and 2, the pump photons. The arrows denoting the pump photon are shown in bold.  $\Delta$  represents the detuning energy between the first excited state and the energy of the higher energy photon (the probe photon in ND-2PA). The

values of the photon energies are given in Tables 6.1 and 6.2. Although the probe is actually composed of a broad continuum of energies, for the sake of simplicity it is represented here as the energy necessary to reach the peak of the 2PA spectrum. The sum of the incident photons is resonant with the final state which can be verified in these Tables concurrent with the knowledge that the experimentally determined state energies are  $E_{2PA}=3.22$  eV for molecule **3** and  $E_{2PA} \approx 4.00$  eV for molecule **5**.

Table 6.1: D-2PA and ND-2PA spectral data for molecule **3**. The photon energies ( $\hbar\omega_1$ ,  $\hbar\omega_2$  in eV) for the experiments schematically represented in Figure 6.1 are given. Also given are the peak 2PA cross-sections in GM units of the experimental ( $\delta_{\text{exp}}$ ) and Sum-Over-States calculated ( $\delta_{\text{SOS}}$ ) 2PA spectra taken in Figure 6.3 as well as their associated resonance enhancements ( $ISRE_{\text{exp}}$ ,  $ISRE_{\text{SOS}}$ ).

	Experimental				Sum-Over-States			
	$\hbar\omega_1$	$\hbar\omega_2$	$\delta_{\text{exp}}^{\text{max}}$	$ISRE_{\text{exp}}$	$\hbar\omega_1$	$\hbar\omega_2$	$\delta_{\text{SOS}}^{\text{max}}$	$ISRE_{\text{SOS}}$
(a)	1.61	1.61	72	1.00	1.72	1.72	65	1.00
(b)	1.84	1.38	133	1.85	2.06	1.38	84	1.29
(c)	2.19	1.03	168	2.33	2.41	1.03	124	1.91
(d)	2.39	0.83	190	2.64	2.61	0.83	169	2.60
(e)	2.53	0.69	239	3.32	2.75	0.69	216	3.32



Table 6.2: D-2PA and ND-2PA spectral data for molecule **5**. The photon energies ( $\hbar\omega_1$ ,  $\hbar\omega_2$  in eV) for the experiments schematically represented in Figure 6.2 are given. Also given are the peak 2PA cross-sections in GM units of the experimental ( $\delta_{\text{exp}}$ ) and Sum-Over-States calculated ( $\delta_{\text{SOS}}$ ) 2PA spectra taken in Figure 6.4 as well as their associated resonance enhancements ( $\text{ISRE}_{\text{exp}}$ ,  $\text{ISRE}_{\text{SOS}}$ ).

Experimental				Sum-Over-States				
	$\hbar\omega_1$	$\hbar\omega_2$	$\delta_{\text{exp}}^{\text{max}}$	$ISRE_{\text{exp}}$	$\hbar\omega_1$	$\hbar\omega_2$	$\delta_{SOS}^{\text{max}}$	$ISRE_{SOS}$
(a)	2.00	2.00	89	1.00	2.03	2.03	100	1.00
(b)	2.35	1.65	169	1.90	2.41	1.65	132	1.32
(c)	2.62	1.38	253	2.84	2.68	1.38	185	1.85
(d)	3.02	1.03	427	4.80	3.03	1.03	391	3.91

The two-photon absorption spectra for molecules **3** and **5** in hexane are shown in Figures 6.3a and 6.4a, respectively. The symbols represent the 2PA cross-sections acquired from the 2PF experiment (i.e. D-2PA) and the WLC pump-probe experiment. The corresponding pump energies for the WLC measurements are listed in the inset. The solid lines are, as usual, two-peaked Gaussian functions which are fitted to the experimental data. First, from Figure 6.3a we note the typical behavior associated with an asymmetric molecule: the peak positions of the 2PA spectra correlate quite well with the position of the first excited state for molecule **3**. This is illustrated by the location of the peak of the linear absorption spectrum given in Table 4.1 ( $E_{01}=3.22$  eV). 2PA into higher lying excited states is also evident. For the second molecule, Figure 6.4a shows peak positions of the 2PA spectra which denote the position of the first two-photon allowed state,  $E_{2\text{PA}}=4.00\text{eV}$ .

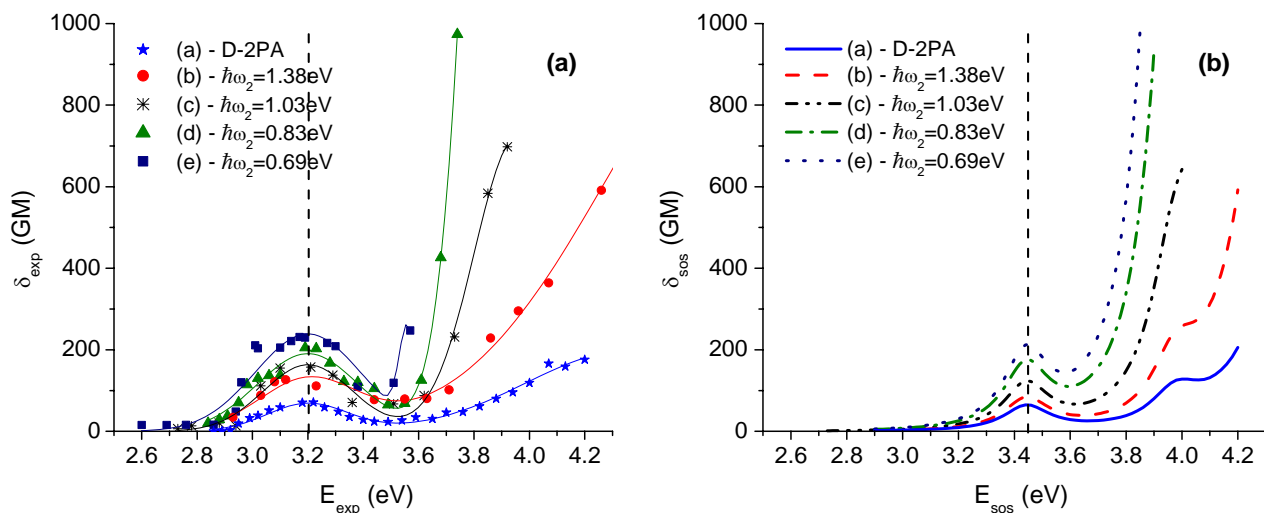


Figure 6.3: D-2PA and ND-2PA spectra of molecule **3** in hexane. Figure 6.3a shows the 2PA spectra for the experiments schematically represented in Figure 6.1. Figure 6.3b shows the Sum-Over-States calculated 2PA spectra. The vertical dashed lines in both figures represent the position of the peak 2PA cross-sections which are given in Table 6.1.

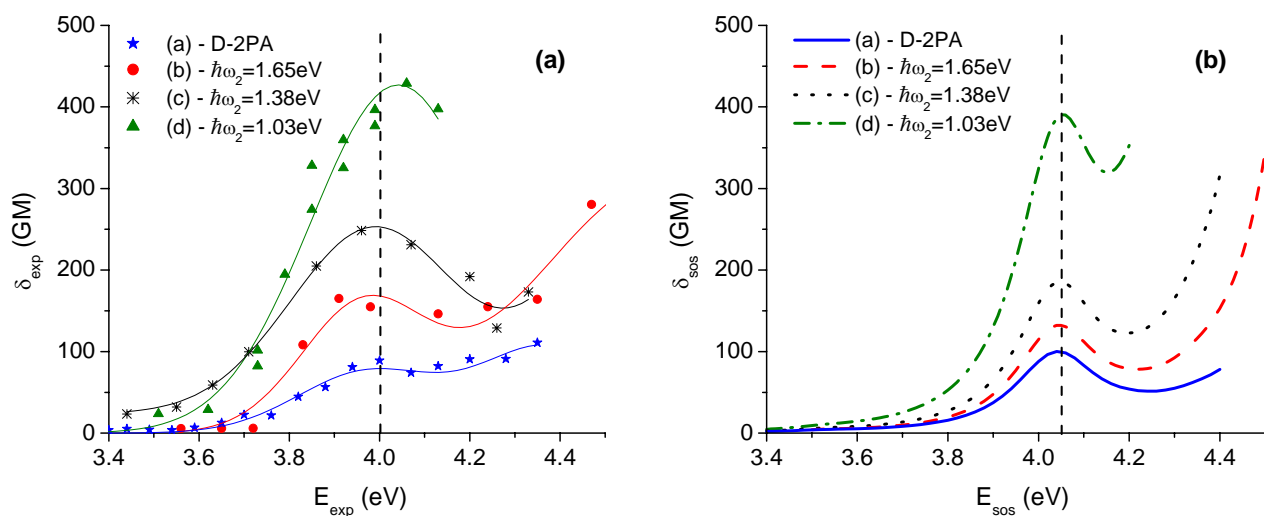


Figure 6.4: D-2PA and ND-2PA spectra of molecule **5** in hexane. Figure 6.4a shows the 2PA spectra for the experiments schematically represented in Figure 6.2. Figure 6.4b shows the Sum-Over-States calculated 2PA spectra. The vertical dashed lines in both figures represent the position of the peak 2PA cross-sections which are given in Table 6.2.

Secondly, both Figures illustrate directly the effect of intermediate state resonance enhancement. As noted in Figures 6.1 and 6.2, a decrease in the pump photon energy causes a reduction in the detuning energy between the probe photon energy and the first excited state (i.e., the intermediate state). This decreased detuning energy leads to resonant enhancement of the 2PA spectra as evidenced in Figures 6.3a and 6.4a. In order to determine the magnitude of this resonance enhancement each peak cross-section (given in Tables 6.1 and 6.2) was normalized to the value acquired from the D-2PA measurement because the degenerate measurement represents the largest possible detuning energy. The values of the ISRE are shown in Tables 6.1 and 6.2. At the two-photon resonance, the data show over a three-fold increase in  $\delta$  for molecule **3** and nearly a five-fold increase for molecule **5**. It is important to realize here that while enhancement into higher lying states (as is the case for **5**) has been observed in molecules when using D-2PA (see Section 5.6), enhancement into the first excited singlet state (as in **3**) is manifestly a consequence nondegenerate excitation. This phenomenon of enhanced two-photon transitions in molecules with permanent dipole moments was predicted theoretically by Scharf and Band [110] in 1988. In addition, we would also like to note that 2PA into higher level excited states of molecule **3** (shown for  $E_{\text{exp}} > 3.22$  eV) also exhibits resonance enhancement. For a pump photon energy of 0.83 eV (indicated by curve (d) in Figure 6.3a), the nondegenerate data show more than 20 times enhancement relative to the degenerate data at a value of 3.75 eV for the sum of the two-photon energies. In this case, the probe photon energy is approximately 2.9 eV; based on the linear absorption spectrum for molecule **3** (Figure 4.5), this corresponds to a detuning energy of only 0.1 eV relative to the first vibronic feature of the  $S_0 \rightarrow S_1$  transition. In this case, this vibronic feature determines the position of the intermediate state which affects resonance enhancement. Linear absorption of the WLC probe beam prevents the measurement

of the ND-2PA spectrum for even higher sums of photon energies. This is reflected in the truncation of the ND-2PA spectra at higher values of  $E_{\text{exp}}$  in the Figures.

Therefore, the results presented above show that ND-2PA exhibits unambiguous enhancement compared to degenerate excitation. We believe this to be the first experimental observation of resonant enhancement of nondegenerate 2PA in organic molecules. However, we note that Baltramiejunas [111] investigated the enhancement of ND-2PA due to deep local levels as intermediate states in ZnO and ZnSe semiconductor crystals.

### 6.1.2 Theoretically Determined Spectra

The degenerate and nondegenerate 2PA spectra for molecules **3** and **5** were calculated by combining the Sum-Over-States perturbation theory expression for  $\gamma$  (Equation 2.7) along with the expression for  $\delta$  given by Equation 2.5. This methodology is identical to that outlined in Section 3.5. However, it is an opportune time to explain why, specifically, the SOS expression for  $\gamma$  derived by Orr and Ward [32] was chosen. These authors chose to expressly include resonance cases in their formulation of  $\gamma$ . While in many instances it is sufficient to relax these conditions (i.e., making the assumption that  $\Omega = \Omega^*$  in Equation 2.7), this is not the case when dealing with ISRE. The grounds for this statement are based on the fact that when one is dealing with ISRE one moves toward a condition of double resonance, that is, resonance not only with the final excited state but with the intermediate state as well. For these cases, resonance issues become crucial and must be taken into account.

The calculated 2PA spectra for the two compounds are given in Figures 6.3b and 6.4b. The pump energies were identical to those used in the experiments described above and are listed

in Tables 6.1 and 6.2. For both molecules, the calculated SOS spectra describe very well the effect of resonance enhancement. Furthermore, the magnitudes of the degenerate and nondegenerate 2PA cross-sections (both for the lowest two-photon allowed state and higher lying states) agree well with the experimental data. As a result, the values for the intermediate state resonance enhancement associated with these values of  $\delta$  are fully consistent with the experimental results (see Tables 6.1 and 6.2). We note for completeness that for molecule **3** the spectral position of the calculated 2PA maximum is shifted with respect to experiment:  $E_{2PA}'=3.44$  eV versus  $E_{2PA}=3.22$  eV (where the prime denotes the theoretical value). This is a result of the aforementioned overestimation of the position of the first excited state (by 0.22eV) in the quantum-chemical calculations; a similar discrepancy occurs for molecule **5** ( $E_{01}'=3.53$  eV versus  $E_{01}=3.3$ eV). The difference in  $E_{01}$  values between the theoretical and experimental results manifests itself in the values presented for the probe photon energies  $\hbar\omega_1$  shown in Table 6.1.

## **6.2 Essential States Model for Nondegenerate Two-Photon Absorption**

Given that the full Sum-Over-States expression for  $\gamma$  (including contributions from the first 300 excited states) provides an effective description of the ISRE phenomenon it is useful to try and find approximations to the full SOS treatment, that would allow for a more simple picture and a greater insight into the nature of ISRE. Following the same approach for the degenerate 2PA case presented in Section 2.3, the D and T terms can also be derived for the nondegenerate case and can be written as:

$$\text{Im } \gamma(-\omega_1; \omega_1, -\omega_2, \omega_2) \approx \text{Im} \left[ \begin{array}{l} \frac{\mu_{ge}^2 \Delta \mu_{ge}^2}{(\Omega_{ge} - \hbar \omega_1 - \hbar \omega_2)} \left\{ \frac{1}{(\Omega_{ge} - \hbar \omega_2)(\Omega_{ge} - \hbar \omega_1)} + \frac{1}{(\Omega_{ge} - \hbar \omega_2)(\Omega_{ge} - \hbar \omega_2)} \right. \\ \left. + \frac{1}{(\Omega_{ge}^* - \hbar \omega_1)(\Omega_{ge} - \hbar \omega_1)} + \frac{1}{(\Omega_{ge}^* - \hbar \omega_1)(\Omega_{ge} - \hbar \omega_2)} \right\} \quad D \\ + \sum_{e'} \frac{\mu_{ge}^2 \mu_{ee'}^2}{(\Omega_{ge'} - \hbar \omega_1 - \hbar \omega_2)} \left\{ \frac{1}{(\Omega_{ge} - \hbar \omega_2)(\Omega_{ge} - \hbar \omega_1)} + \frac{1}{(\Omega_{ge} - \hbar \omega_2)(\Omega_{ge} - \hbar \omega_2)} \right. \\ \left. + \frac{1}{(\Omega_{ge}^* - \hbar \omega_1)(\Omega_{ge} - \hbar \omega_1)} + \frac{1}{(\Omega_{ge}^* - \hbar \omega_1)(\Omega_{ge} - \hbar \omega_2)} \right\} \quad T \end{array} \right] \quad 6.1$$

where  $\mu_{ge}$  is the transition dipole moment between the ground state  $|g\rangle$  and  $|e\rangle$ ,  $\mu_{ee'}$  is the transition moment between  $|e\rangle$  and  $|e'\rangle$ , and  $\Delta \mu_{ge}$  is the difference between the permanent dipole moments in states  $|g\rangle$  and  $|e\rangle$ .  $\Omega_{ge} = E_{ge} - i\Gamma_{ge}$  and  $\Omega_{ge'} = E_{ge'} - i\Gamma_{ge'}$ , where  $E_{ge}$  and  $E_{ge'}$  are the transition energies from the ground state to the relevant excited states and  $\Gamma$  is the damping term associated with these states (set to a constant value of 0.1 eV as mentioned above). It should be noted that Equation 6.1 exactly reproduces the essential states expression for D-2PA given by Equation 2.8 when  $\hbar\omega_1 = \hbar\omega_2 = \hbar\omega$ .

For the case of a resonance into a particular excited state ( $\hbar\omega_1 + \hbar\omega_2 = E_{ge}$  in the case of 2PA into the one-photon allowed state  $|e\rangle$  and  $\hbar\omega_1 + \hbar\omega_2 = E_{ge'}$  for excitation into  $|e'\rangle$ ) and when the damping is much smaller than the photon energies, one obtains from Equations 6.1 and 2.5 (the expression for  $\delta$ ):

$$\delta_{D,|e\rangle} \approx K \frac{\mu_{ge}^2 \Delta \mu_{ge}^2}{\Gamma_{ge}} \left( \frac{1}{\hbar\omega_1} + \frac{1}{\hbar\omega_2} \right)^2 \quad 6.2$$

for the D-term describing ND-2PA into  $|e\rangle$  and

$$\delta_{T,|e'\rangle} \approx K \frac{\mu_{ge}^2 \Delta \mu_{ge}^2}{\Gamma_{ge}} \left( \frac{1}{E_{eg} - \hbar\omega_1} + \frac{1}{E_{eg} - \hbar\omega_2} \right)^2 \quad 6.3$$

for the T-term describing ND-2PA into  $|e'\rangle$ .  $K$  is a common factor (see also Equation 2.5) and is given by:

$$K = \frac{3L_1^2 L_2^2}{5n_1 n_2 c^2 \epsilon_0 \hbar} \frac{\hbar\omega_2 (\hbar\omega_1)^2}{(\hbar\omega_1 + \hbar\omega_2)}. \quad 6.4$$

The  $\delta_D$  is associated with noncentrosymmetric systems and can be used to describe the 2PA spectra of molecule **3** while  $\delta_T$  should provide a proper qualitative description of molecule **5**.

To study the reliability of the essential-state models in the description of resonance enhancement, we have compared the values for  $\delta$  and ISRE obtained from the converged SOS approach (see Tables 6.1 and 6.2) to those obtained from Equations 6.2 and 6.3. The relevant transition energies and dipole moments (as obtained from the quantum-chemical calculations described in Section 3.5) are given in Table 6.3; for molecule **3**, only the properties of the one-photon state are given while for molecule **5** the energy and transition dipole to the dominant 2PA active state in the spectral region of the 2PA maximum are also given.

Table 6.3: Select quantum-chemically calculated transition energies (in eV) and dipole moments (in debye) for molecules **3** and **5**. These terms are used in the calculations for  $\delta_D$  and  $\delta_T$  which are given in Table 6.4.

Molecule <b>3</b>		Molecule <b>5</b>	
$E_{ge}$	3.44	$E_{ge}$	3.53
$\mu_{ge}$	10.31	$\mu_{ge}$	8.78
$\Delta\mu_{ge}$	7.78	$E_{ge'}$	4.05
		$\mu_{ee'}$	5.80

The comparison between the converged SOS results and the essential-state results is shown in Table 6.4. For both molecules, the ISRE is well reproduced by the essential-state models. However, the magnitude of the ISRE is somewhat underestimated, especially for molecule **3**. This is actually largely due to an overestimation of the degenerate 2PA cross-section by the essential states model. It turns out from a detailed analysis of the different channels contributing to the fully-converged results that higher-lying one-photon allowed intermediate states result in mixed contributions which reduce  $\delta$  (indeed, for the molecules investigated here, the linear absorption spectra in Figures 5.4 and 5.5 show that there are additional strongly one-photon allowed states around 4 eV). When the probe wavelength is tuned close to the first linear absorption, the  $\delta_D$  (Equation 6.2) contribution to the overall 2PA into  $|e\rangle$  is much more strongly enhanced than the channels involving these higher-lying excited states. Therefore, the relative contribution of those channels decreases in the case of ISRE. This explains why the relative error in  $\delta_D$  decreases for larger probe energies and the overall ISRE is smaller than for the converged results. These deviations are much smaller in molecule **5**, since there the coupling via the higher-lying one-photon allowed states is weaker.



Thus, the essential states models provide a qualitative (and in the case of molecule **5** also quantitative) description of ISRE, which allows a simple analysis of ISRE in terms of Equation 6.2 and 6.3. One finds a resonance enhancement for  $\delta_D$  when either  $\hbar\omega_1$  or  $\hbar\omega_2$  approaches zero, which for 2PA into  $|e\rangle$  requires  $\hbar\omega_2 \rightarrow E_{ge}$  or  $\hbar\omega_1 \rightarrow E_{ge}$ . This is fully consistent with the experimental finding that the ND-2PA cross-section strongly increases when the energy of the probe photon approaches the one-photon resonance. The resonances in  $\delta_T$  also occur, when  $\hbar\omega_2 \rightarrow E_{ge}$  or  $\hbar\omega_1 \rightarrow E_{ge}$ , rationalizing the increase in the cross-section when the probe energy in the experiments approaches the energy of the intermediate one-photon state.

In conclusion, by using ND-2PA to control the photon energies involved in the 2PA process, a quantitative study of the effect of intermediate state resonance enhancement (ISRE) in a single molecule was performed. This produced over a five times enhancement in the value of the peak 2PA cross-section for the symmetric molecule (**5**) when compared to degenerate 2PA. The asymmetric molecule (**3**) exhibited over a three-fold enhancement at its peak with higher-lying excited states revealing over a 20 times enhancement of the nonlinearity. Given the potential to generate well over an order of magnitude enhancement of the nonlinearity, this could provide great impetus for the development of applications which exploit ND-2PA. Finally, a simplified three-level model for ND-2PA was also developed and provides good insight into the mechanism of ISRE.

Table 6.4: Degenerate and nondegenerate 2PA cross-sections in GM units and ISRE for molecule **3** and molecule **5** as obtained from the essential-state models given in Equations 6.2 and 6.3, respectively.  $\hbar\omega_1$  and  $\hbar\omega_2$  are given in eV.

Molecule 3				Molecule 5			
$\hbar\omega_1$	$\hbar\omega_2$	$\delta_D$	$ISRE_D$	$\hbar\omega_1$	$\hbar\omega_2$	$\delta_T$	$ISRE_T$
1.72	1.72	135	1.00	2.03	2.03	99	1.00
2.06	1.38	168	1.25	2.41	1.65	130	1.31
2.41	1.03	225	1.67	2.68	1.38	179	1.80
2.61	0.83	279	2.07	3.03	1.03	365	3.66
2.75	0.69	335	2.49				

## CHAPTER 7: CONCLUSION

### 7.1 Synopsis

In this dissertation the relationships between chemical structure and the two-photon absorbing properties of a series of fluorene derivatives were studied. The systematic alteration of these molecules gave rise to a myriad of structural design changes which affected the nonlinearity. These included the effects of structural symmetry, solvent polarity, strengths of electron active end-groups, various avenues of conjugation extension, and higher dimensionality. In order to ensure that the measured two-photon absorptivities of these molecules were reliable and consequently so were the structure-property relations, three completely independent nonlinear spectroscopic techniques were employed. The strong agreement which was eventually demonstrated between these two techniques and the well-known Z-Scan method gave us confidence in our experimental results.

To provide plausible explanations for these experimentally observed trends, the conceptually simple essential states model was employed. Since it predicted an intimate relationship between nonlinear optical response and the linear optical properties of the system, the full linear spectroscopic analysis of these derivatives was undertaken. Quantum-chemical methods were employed to obtain other critical molecular properties that might impact the nonlinearity. The correlation between the optical properties of these molecules and their

structural modifications lead to the following conclusions concerning their two-photon absorbing capabilities:

- **Symmetry:** Symmetrically substituted fluorene derivatives exhibit negligible 2PA into the first excited state ( $S_1$ ) but strong absorption into the first two-photon allowed state, reminiscent of true centrosymmetric systems. Asymmetric derivatives clearly indicate that significant 2PA is possible into any excited state. Since these trends follow for nearly all the derivatives studied here, spectral locations of 2PA can be predicted via linear absorption spectra.
- **Dipolar Systems:** The study of the dipolar molecules **1-4** reveal that the optimum terminal group which maximizes  $\delta$  into  $S_1$  does *not* correspond to the molecule which possesses the strongest ground-state dipole moment but rather belongs to molecule **3** with its benzothiazole terminal group. This is attributed to its optimal charge transfer character which maximizes the product of its change in state (or permanent) dipole moments and its transition dipole moment.
- **Solvism:** Dipolar fluorenyl systems such as molecules **3** and **9** undoubtedly benefit from a more polar environment. Molecule **3** shows a monotonic increase in  $\delta$  into  $S_1$  as the polar character of the solvent is raised concluding with a three-fold enhancement observed in the most polar solvent studied, acetone. These effects are even more pronounced in the longer dipolar system **9**. This enhancement is a result of the greater charge transfer produced upon excitation, i.e., an increased value of  $\Delta\mu_{01}$ . In addition, molecule **9** shows that 2PA into the second excited state ( $S_2$ ) also benefits from a more polar environment.
- **Symmetric Systems:** Given the symmetric molecules **5** and **6**, the acceptor substituted system **6** clearly outperforms the donor end-capped derivative **5**. From quantum-chemical calculations, this can be attributed to an enhanced value of  $\mu_{12}$ . This is justified by the fact that electron withdrawing groups are more likely to induce center-to-periphery charge transfer. No benefit in the nonlinearity is observed when going to stronger acceptor groups in A- $\pi$ -A systems, in fact, the magnitude suffered considerably.
- **Styryl Extension - Dipolar:** For extension via a styryl bridge in dipolar systems (such as in **9** or **10**), the peak cross-section into  $S_1$  shows a 2.5 times improvement compared to the shorter conjugated system (**3**) while (at least in **9**) the values into  $S_2$  show over 4 times enhancement in the nonlinearity. The enhancement in the nonlinearity for **9** is a result of an augmented value for  $\Delta\mu_{01}$  when dealing with 2PA into  $S_1$  and larger values of  $\mu_{12}$  for excitation into  $S_2$ . Given the better efficiency of 2PA into  $S_2$ , it is expected that the dependence of  $\mu_{12}$  on styryl conjugation length is favored over  $\Delta\mu_{01}$ .
- **Styryl Extension - Symmetric:** Styryl extension in symmetric systems show perhaps the most promise of all the derivatives. Again, the A- $\pi$ -A (**12**) system outperforms its D- $\pi$ -D

(**11**) counterpart. However, each molecule shows substantial 2PA into the first two-photon allowed state with **11** exhibiting nearly a 24 times enhancement compared to its shorter counterpart (**5**) going from 90 to 2160 GM. Molecule **12** also showed considerable improvement increasing the peak nonlinearity from 470 to 6300 GM, a 13-fold increase. In addition to showing one of the largest peak nonlinearities, **12** also presented the added advantage of exhibiting substantial two-photon activity at longer wavelengths as well. In fact, the nonlinearity in this region rivals some of the most efficient dipolar compounds in this study.

- **Vinyl-Fluorene Extension:** Molecules **13-15** prove that as conjugation length is increased along the main backbone, independent of the conjugation route taken, the peak nonlinearity into  $S_1$  intensifies. However, there is no strong evidence that vinyl-fluorene extension (**13** and **14**) is favored over styryl extension (**9**) in terms of 2PA (both show roughly three times enhancement compared to the model compound **3**). However, the use of the two conjugation avenues in series (**15**) gives promise of some type of cooperative enhancement of the nonlinearity showing a 15 times improvement in  $\delta$  over **3**.
- **Amino-Fluorene Extension:** The peak nonlinearity into  $S_2$  for this series of diphenylaminofluorene-based chromophores (**16** and **17**) shows a definitive increase with the number of repeat units in the molecule. However, there is not a significant gain in the effective nonlinearity as molecular length increases which is not surprising given the system is *not* conjugated along its backbone. Nonetheless, the peak value of 2PA in the longest chain molecule is one of the highest measured ( $\sim 7000$  GM) for these derivatives.
- **Multi-Branched Systems:** These molecules with increased dimensionality (**18** and **19**) do not necessarily exhibit greater charge transfer which would lead to more effective nonlinearities. Nonetheless, they still hold two distinct benefits: an increase in the overall magnitude of two-photon activity as well as an increased spectral band of useable nonlinearity ( $>1000$  GM over entire spectral band).
- **Resonance Enhancement:** The red-shifting of the linear absorption peak by  $>50$  nm in **20** compared to **3** suggests a two-fold increase in the nonlinearity due to the decrease in the detuning energy. Although this is experimentally observed, it is difficult to discount other factors which may have impacted the enhancement.
- **ISRE:** The use of ND-2PA showed that enhancement of 2PA due to resonance enhancement could be observed in both symmetric and asymmetric systems. In fact, in the asymmetric system well over an order of magnitude enhancement in the nonlinearity, when compared to D-2PA, is generated.

## 7.2 Future Work

From the conclusions listed above, a few avenues of promising potential research were revealed:

- 1) Molecules **3** and **5** are used extensively throughout this study as model compounds for the more structurally complex derivatives. Given the comprehensive linear and nonlinear characterization (both D-2PA and ND-2PA) performed on these molecules as well as the successful quantum-chemical analysis reported, these molecules should serve as ideal candidates for standards in both one and two-photon absorption studies. Knowledge of their solvism traits as well as their photochemical stability only serves to enhance this possibility.
- 2) Given the success in enhancing the nonlinearity that was observed when dipolar systems are placed in more polar environments, similar experiments should test the feasibility of this approach in symmetric systems. Given that molecule **9** shows that 2PA into  $S_2$  benefits from a more polar environment, this may very well portend enhancement in symmetric systems as well where  $\mu_{ee'}$  is a crucial term governing 2PA. Molecules that possess considerable values of  $\mu_{ee'}$ , such as **11** and **12**, would be ideal candidates for this study.
- 3) Future work should certainly involve attempts at synthesizing molecules with quadrupolar geometries given that many groups have observed substantial benefits to 2PA when employing these architectures. Given the success of the A- $\pi$ -A archetypes (i.e., molecules **6** and **12**), they are perhaps the most ideal starting points. Appending a donor substituent somewhere along the central  $\pi$ -conjugated backbone may serve in maximizing the nonlinearity by assisting the already substantial charge transfer in the excited state. This could be accomplished using strategies along the lines of those employed in the synthesis of derivatives **18** and **19** which were functionalized on position 4 of the fluorene chromophore. If this proves synthetically difficult, one of the alkane chains appended on position 9 could be sacrificed for the appended donating moiety.
- 4) Given the tremendous enhancement of the nonlinearity noted in compounds whose conjugation length has been augmented by styryl extension, future synthetic schemes should certainly involve further extension in this manner. This could include an additional styryl unit before the withdrawing end-group in a dipolar compound (e.g., **9**) or possibly interleaving a styryl bridge before the diphenylamine donating group. Given the cooperative enhancement found in molecule **15**, a styryl bridge diametrically opposed to the initial one may result in significant improvements in two-photon efficiency. Finally, in the symmetric systems which show the most promise (particularly the A- $\pi$ -A system **12**), appending additional styryl units to the chain may not only increase the peak nonlinearity, it may also provide greater nonlinearity throughout the entire band. And for any one of these molecules, further extension might provide clear evidence as to the

functional dependence of the dipole moments (and consequently the nonlinearity) on this type of conjugation extension. This could be quantified by investigating the trends of the effective nonlinearity ( $\delta^{\text{max}}/N$ ) as conjugation length is increased.

## **APPENDIX A: DERIVATION OF THE NONDEGENERATE TWO- PHOTON ABSORPTION CROSS-SECTION**



This derivation follows the one given in Reference 112 in the Section entitled “Nonlinear Dissipative Processes”. However, the single-beam photon flux approach studied there has been appropriately modified for a two-beam interaction.

An appropriate starting point for this analysis is the total energy exchanged per unit time and volume between two distinguishable light beams and a molecular ensemble:

$$\frac{dW}{dt} = \langle E \bullet \dot{P} \rangle \quad \text{A. 1}$$

where  $W$  is the total energy,  $E$  is one of the incident electric fields, and  $\dot{P}$  is the time derivative of the induced nonlinear polarization. The brackets imply a time average over many optical field cycles. For monochromatic waves with amplitudes  $E_1$  and  $P$  and an electric field frequency  $\omega_1$ , the time average is:

$$\frac{dW}{dt} = \frac{1}{2} \omega_1 \text{Im}(E_1^* \bullet P) . \quad \text{A. 2}$$

Here, the subscript 1 will refer to the probe beam in our two-beam interaction. The nonlinear polarization associated with a nondegenerate interaction (parallel polarizations, unequal frequencies) is:

$$P = \frac{3\varepsilon_o}{4} \chi^{(3)}(-\omega_1; \omega_1, -\omega_2, \omega_2) |E_2|^2 E_1 \quad \text{A. 3}$$

where subscript 2 refers to the pump beam. Substituting Equation A.3 into A.4 gives

$$\frac{dW}{dt} = \frac{3\omega_1 \varepsilon_o}{8} \text{Im}(\chi^{(3)}(-\omega_1; \omega_1, -\omega_2, \omega_2)) |E_2|^2 |E_1|^2 \quad \text{A. 4}$$

and using the definition  $I = \frac{1}{2} \varepsilon_o c n |E|^2$  in Equation A.4 generates

$$\frac{dW}{dt} = \frac{3\omega_1 I_1 I_2 \text{Im}(\chi^{(3)}(-\omega_1; \omega_1, -\omega_2, \omega_2))}{2\varepsilon_o c^2 n_1 n_2}. \quad \text{A. 5}$$

Using the definition for the nondegenerate 2PA cross-section given by the rate equation description (in direct analogy with Equation 2.4), we have

$$\frac{dn_p}{dt} = \delta_{ND} N F_1 F_2 \quad \text{A. 6}$$

where  $dn_p/dt$  is the total number of photons absorbed by the molecular ensemble per unit time and volume,  $N$  is the density of absorbing molecules, and  $F = I / \hbar\omega$  is the photon flux for each

individual beam. Using the fact that  $dW = dn_p (\frac{\hbar\omega_1 + \hbar\omega_2}{2})$  we can divide Equation A.5 by

Equation A.6 and set it equal to  $(\frac{\hbar\omega_1 + \hbar\omega_2}{2})$  to solve for  $\delta$ :

$$\delta_{ND} = \left( \frac{1}{N F_1 F_2} \right) \frac{3\omega_1 I_1 I_2 \text{Im}(\chi^{(3)}(-\omega_1; \omega_1, -\omega_2, \omega_2))}{\hbar(\omega_1 + \omega_2) \varepsilon_o c^2 n_1 n_2} \quad \text{A. 7}$$

or equivalently by using  $F = I / \hbar\omega$  :

$$\delta_{ND} = \frac{3\hbar\omega_1^2 \omega_2 \text{Im}(\chi^{(3)}(-\omega_1; \omega_1, -\omega_2, \omega_2))}{N(\omega_1 + \omega_2) \varepsilon_o c^2 n_1 n_2}. \quad \text{A. 8}$$

Finally, from Reference 26 we can relate the microscopic polarizability  $\gamma$  to its macroscopic counterpart, the third-order susceptibility  $\chi^{(3)}$ :

$$\chi^{(3)}(-\omega_1; \omega_1, -\omega_2, \omega_2) = L_1^2 L_2^2 N \gamma(-\omega_1; \omega_1, -\omega_2, \omega_2) \quad \text{A. 9}$$

where  $L$  is the local field factor at each frequency. Subbing A.9 into A.8 we have:

$$\delta_{ND} = L_1^2 L_2^2 \frac{3\hbar\omega_1^2\omega_2 \operatorname{Im}(\gamma(-\omega_1; \omega_1, -\omega_2, \omega_2))}{(\omega_1 + \omega_2)\varepsilon_o c^2 n_1 n_2} \quad \text{A. 10}$$

This equation for the nondegenerate 2PA cross-section reduces to the well-known expression for degenerate 2PA (see for example References 22 and 23) when  $L_1 = L_2$ ,  $n_1 = n_2$ , and  $\omega_1 = \omega_2$ .

We can also relate  $\delta_{ND}$  to the nondegenerate two-photon absorption coefficient  $\beta_{ND}$ . From Reference 113 we have the following definition:

$$\beta_{ND} = \frac{3\pi}{\varepsilon_o c n_1 n_2 \lambda_1} \operatorname{Im}(\chi^{(3)}(-\omega_1; \omega_1, -\omega_2, \omega_2)). \quad \text{A. 11}$$

Substituting this into Equation A.10 leaves us with an alternative definition for  $\delta_{ND}$ :

$$\delta_{ND} = \frac{\hbar\beta_{ND}}{N} \left( \frac{2\omega_1\omega_2}{\omega_1 + \omega_2} \right) = \frac{\hbar\beta_{ND}}{N} \left( \frac{2c}{\lambda_1 + \lambda_2} \right). \quad \text{A. 12}$$

Once again, this equation reduces to the well-known expression for the degenerate  $\delta$  in terms of the degenerate  $\beta$  (see Reference 113) when  $\omega_1 = \omega_2$ .

## **APPENDIX B: DERIVATION OF THE INTENSITY OF THE COLLECTED TWO-PHOTON FLUORESCENCE SIGNAL**

The following analysis for the time-averaged photon flux measured by the 2PF experiment described in Section 3.2.1 is described fully in Reference 16. Noting that the number of photons absorbed per unit time  $N_{\text{abs}}$  for a 2PA process is proportional to the 2PA cross-section,  $\delta$ , and the square of the incident irradiance  $I$ , one can write:

$$N_{\text{abs}}(t) = \int_V dV \delta C(r, t) I^2(r, t) \cdot \quad \text{B. 1}$$

Here, the dye concentration  $C$  as well as the irradiance are functions of both time and space and so  $N_{\text{abs}}$  must be integrated over the entire illuminated sample volume  $V$ . Assuming negligible photobleaching and saturation,  $C(r, t)$  can be made a constant. Furthermore, separating the temporal and spatial components of the excitation irradiance we have:

$$N_{\text{abs}}(t) = C \delta I_o^2(t) \int_V dV S^2(r) \quad \text{B. 2}$$

where  $S(r)$  and  $I(t)$  are the spatial and temporal distributions of the incident irradiance, respectively.

Assuming that 2PF is the only subsequent process to the excitation process, the number of fluorescence photons collected per unit time, denoted by  $F(t)$ , is given by:

$$F(t) = \frac{1}{2} \Phi \eta N_{\text{abs}} \quad \text{B. 3}$$

where  $\Phi$  is the overall collection efficiency of the spectrofluorimeter,  $\eta$  is the fluorescence quantum yield of the sample and the factor of  $1/2$  refers to the fact that two photons are absorbed for every one fluorescing photon. Since, in practice, only the time-average photon flux is measured we write:

$$\langle F(t) \rangle = \frac{1}{2} g \Phi \eta C \delta \langle I_o(t) \rangle^2 \int_V dV S^2(r) \quad \text{B. 4}$$

where  $g = \frac{\langle I_0^2(t) \rangle}{\langle I_0(t) \rangle^2}$  is the second-order temporal coherence of the excitation light.

Finally, assuming that the irradiance in the focal volume is formed from an aperture diffraction limited focus (see Section 3.2.1), we can rewrite Equation B.4 as the following:

$$\langle F(t) \rangle = \frac{1}{2} g \Phi \eta C \delta \left( \frac{\pi(\text{N.A.})^2}{\lambda^2} \right)^2 \langle P(t) \rangle^2 \int_V dV S^2(r, z) \quad \text{B. 5}$$

where N.A. is the numerical aperture of the focusing lens,  $\lambda$  is the wavelength of the excitation source and  $P(t)$  is the incident laser power. The relationship between  $P$  and  $I_0$  follows from energy conservation:

$$I_0(t) = \frac{\pi(\text{N.A.})^2}{\lambda^2} P(t). \quad \text{B. 6}$$

Although the assumption of an aperture diffraction limited focus is not strictly valid for our experimental apparatus, the spatial dependence of the irradiance turns out to be inconsequential in the calculation of  $\delta$  (see Section 3.2.3).

**APPENDIX C: CHEMICAL NOMENCLATURE FOR FLUORENE  
DERIVATIVES**

The following proper chemical names can be correlated to their appropriate chemical structures shown in Figure 4.3.

1. (9,9-didecyl-7-nitro-fluoren-2-yl)diphenylamine
2. 9,9-didecyl-7-diphenylamino-fluorene-2-carbonitrile
3. (7-benzothiazol-2-yl-9,9-didecyl-fluoren-2-yl)diphenylamine
4. 1-[9,9-didecyl-7-(di-p-tolyl-amino)-fluoren-2-yl]ethanone
5. 9,9-didecyl-2,7-bis-(N,N-diphenylamino)fluorene
6. 9,9-didecyl-2,7-bis-(N,N-benzothiazoyl)fluorene
7. 9,9-didecyl-fluorene-2,7-dicarbonitrile
8. 9,9-didecyl-7-nitro-fluorene-2-carbonitrile
9. {7-[2-(4-benzothiazol-2-yl-phenyl)vinyl]9,9-didecyl-fluoren-2-yl}diphenylamine
10. {4-[2-(7-diphenylamino-9,9-diethylfluoren-2-yl)vinyl]phenyl}phosphonic acid diethyl ester
11. 4,4'-[[9, 9-bis(ethyl)-9H-fluorene-2, 7-diyl]di-2,1-ethenediyl]bis (N, N-diphenyl)benzeneamine
12. 2,7-bis-[4-(9,9-didecyl-fluoren-2-yl)-vinyl]-phenyl-benzothiazole
13. {7-[2-(7-benzothiazol-2-yl-9,9-didecyl-fluoren-2-yl)vinyl]9,9-didecyl-fluoren-2-yl}diphenylamine
14. {7-[2-(9,9-didecyl-7-nitro-fluoren-2-yl)vinyl]9,9-didecyl-fluoren-2-yl}diphenylamine
15. [7-(2-{7-[2-(4-benzothiazol-2-yl-phenyl)-vinyl]9,9-didecyl-fluoren-2-yl}vinyl)-9,9-didecyl-fluoren-2-yl]diphenylamine



16. 9,9-didecyl-*N,N*-bis(9,9-didecyl-7-*N,N*-diphenylamino fluorene-2-yl)-*N,N*-diphenyl-  
fluorene-2,7-diamine
17. poly(9,9-didecyl-2,7-diphenylamino fluorene)
18. 4, 4', 4''-[[9, 9-bis(ethyl)-9H-fluorene-2, 4, 7-triyl]tri-2,1-ethenediyl]tris (*N,N*-  
diphenyl)benzeneamine
19. dendrimer dye
20. 2-(9,9-didecyl-7-diphenylamino-fluorene-2-yl)-3-methyl-benzothiazolium,  
trifluoromethanesulfonate

## LIST OF REFERENCES

- 
- [1] M. Göppert-Mayer, “Elementary actions with two quantum leaps”, *Ann. Physik*, Vol. 9, 273 (1931).
- [2] R. R. Birge and B. M. Pierce, “Semiclassical time-dependent theory of two-photon spectroscopy. The effect of dephasing in the virtual level on the two-photon excitation spectrum of isotachysterol”, *Int. J. Quan. Chem.*, Vol. 29, 639 (1986); A. M. Bonch-Bruевич and V. A. Khodovoi, “Multiphoton processes”, *Soviet Physics USPEKHI-USSR*, Vol. 85, 1 (1965).
- [3] W. Kaiser, C. G. B. Garrett, “Two-photon excitation in  $\text{CaF}_2:\text{Eu}^{2+}$ ”, *Phys. Rev. Lett.*, Vol. 7, 229 (1961).
- [4] P. A. Franken, A. E. Hill, C. W. Peters, and G. Weinreich, “Generation of optical harmonics”, *Phys. Rev. Lett.*, Vol. 7, 118 (1961).
- [5] J. J. Hopfield, J. M. Worlock, and K. Park, “Two-quantum absorption spectrum of KI”, *Phys. Rev. Lett.*, Vol. 11, 414 (1963).
- [6] J. L. Bredas, “Computational design of novel materials with enhanced two-photon absorption properties”, *Presentation*, (2003).
- [7] S. L. Jacques, S. A. Prahl, “Absorption spectra for biological tissues”, *Oregon Graduate Institute*, <http://omlc.ogi.edu/classroom/ece532/class3/muaspectra.html> (1998).
- [8] W. Denk, J. H. Strickler, and W. W. Webb, “Two-photon laser scanning fluorescence microscopy”, *Science*, Vol. 248, 73 (1990); R. H. Köhler, J. Cao, W. R. Zipfel, W. W.

- 
- Webb, and M. R. Hansen, "Exchange of protein molecules through connections between higher plant plastids", *Science*, Vol. 276, 2039 (1997); F. Bestvater, E. Spiess, G. Stobrawa, M. Hacker, T. Feurer, T. Porwol, U. Berchner-Pfannschmidt, C. Wotzlaw, H. Acker, "Two-photon fluorescence absorption and emission spectra of dyes relevant for cell imaging", *J. Microscopy*, Vol. 208, 108 (2002); M. J. Miller, S. H. Wei, I. Parker, and M. D. Cahalan, "Two-photon imaging of lymphocyte motility and antigen response in intact lymph node", *Science*, Vol. 296, 1869 (2002).
- [9] L. W. Tutt and T. F. Boggess, "A review of optical limiting mechanisms and devices using organics, fullerenes, semiconductors and other materials", *Prog. Quan. Elec.*, Vol. 17, 299 (1993); A. A. Said, C. Wamsely, D. J. Hagan, E. W. Van Stryland, B. A. Reinhardt, P. Roderer and A. G. Dillard, "Third- and fifth-order optical nonlinearities in organic materials", *Chem. Phys. Lett.*, Vol. 228, 646 (1994); J. D. Bhawalkar, G. S. He and P. N. Prasad, "Nonlinear multiphoton processes in organic and polymeric materials", *Rep. Prog. Phys.*, Vol. 59, 1041 (1996); J. E. Ehrlich, X. L. Wu, Ys. L. Lee, Z. Y. Hu, H. Rockel, S. R. Marder and J. W. Perry, "Two-photon absorption and broadband optical limiting with bis-donor stilbenes", *Opt. Lett.*, Vol. 22, 1843 (1997).
- [10] D. A. Parthenopoulos and P.M. Rentzepis, "3-dimensional optical storage memory", *Science*, Vol. 245, 843 (1989); D. A. Parthenopoulos, P. M. Rentzepis, "Two-photon volume information storage in doped polymer systems", *J. Appl. Phys.*, Vol. 68, 5814 (1990); J. H. Strickler and W. W. Webb, "3-dimensional optical data storage in refractive media by 2-photon point excitation", *Opt. Lett.*, Vol. 16, 1780 (1991); B. H. Cumpston, S. P. Ananthavel, S. Barlow *et al.*, "Two-photon polymerization initiators for three-dimensional optical data storage and microfabrication", *Nature*, Vol. 398, 51 (1999); S. Kawata, H.-B.

- 
- Sun, T. Tanaka and K. Takada, "Finer features for functional microdevices - Micromachines can be created with higher resolution using two-photon absorption", *Nature*, Vol. 412, 697 (2001); W. H. Zhou, S. M. Kuebler, K. L. Braun, T. Y. Yu, J. K. Cammack, C. K. Ober, J. W. Perry, and S. R. Marder, "An efficient two-photon-generated photoacid applied to positive-tone 3D microfabrication", *Science*, Vol. 296, 1106 (2002).
- [11] D. L. Pettit, S. S. H. Wang, K. R. Gee, and G. J. Augustine, "Chemical two-photon uncaging: a novel approach to mapping glutamate receptors", *Neuron*, Vol. 19, 465 (1997); E. A. Wachter, W. P. Partridge, W. G. Fisher, H. C. Dees, and M. G. Petersen, "Simultaneous two-photon excitation of photodynamic therapy agents", *Proc. SPIE*, Vol. 3269, 68 (1998).
- [12] E. B. Brown, J. B. Shear, S. R. Adams, R. Y. Tsien, W. W. Webb, "Photolysis of caged calcium in femtoliter volumes using two-photon excitation", *Biophys. J.*, Vol. 76, 489 (1999); C. Soeller, M. D. Jacobs, P. J. Donaldson, M. B. Cannell, K. T. Jones, G. C. R. Ellis-Davies, "Application of two-photon flash photolysis to reveal intercellular communication and intracellular  $\text{Ca}^{2+}$  movements", *J. Biomed. Opt.*, Vol. 8, 418 (2003); S. S.-H. Wang, L. Khiroug, G. J. Augustine, "Quantification of spread of cerebellar long-term depression with chemical two-photon uncaging of glutamate", *Proc. Natl. Acad. Sci. USA*, Vol. 97, 8635 (2000).
- [13] S. R. Marder, J. W. Perry, J. L. Bredas, D. McCord-Maughon, M. E. Dickinson, S. E. Fraser, D. Beljonne, and T. Kogej, in *Conjugated Oligomers, Polymers, and Dendrimers: From Polyacetylene to DNA*, Proceedings of the Fourth Francqui Colloquium, J. L. Bredas, Ed., De Boeck Universite, Paris, pp. 395-424 (1998).
- [14] G. I. Stegeman, "Material figures of merit and implications to all-optical waveguide switching", *Proc. SPIE*, Vol. 1852, 75 (1993).

- 
- [15] C. Sauteret, J.-P. Hermann, R. Frey, F. Pradere, J. Ducuing, R. H. Baughman and R. R. Chance, "Optical nonlinearities in one-dimensional conjugated polymer crystals", *Phys. Rev. Lett.*, Vol. 36, 956 (1976).
- [16] C. Xu, W. W. Webb, "Measurement of two-photon excitation cross sections of molecular fluorophores with data from 690 to 1050 nm", *J. Opt. Soc. Am. B*, Vol. 13, 481 (1996).
- [17] F. Meyers, S. R. Marder, and J. W. Perry, in *Chemistry of Advance Materials*, L. V. Interrante, M. J. Hampden, Eds., Wiley-Interscience, New York, 207-269 (1998).
- [18] P. N. Butcher and D. Cotter, *The Elements of Nonlinear Optics*, Cambridge University Press, Cambridge, U.K. (1990).
- [19] A. D. Buckingham, "Permanent and induced molecular moments and long-range intermolecular forces", *Adv. Chem. Phys.*, Vol. 12, 107 (1967).
- [20] B. Dick, R. M. Hochstrasser and H. P. Trommsdorff, *Nonlinear Optical Properties of Organic Molecules and Crystals*, Academic Press, Orlando, 503-504 (1987).
- [21] J. Burris, T. J. McGee, and T. J. McIlrath, "A two-photon absorption cross section measurement in nitric oxide", *Chem. Phys. Lett.*, Vol. 101, 588 (1983); E. M. Elveth and W. L. Peticolas, "Two-photon capture cross sections of pyrene and benzpyrene from SCF-MO calculations", *J. Chem. Phys.*, Vol. 41, 1400 (1964).
- [22] E. Zojer, D. Beljonne, T. Kogej, H. Vogel, S. R. Marder, J. W. Perry and J. L. Bredas, "Tuning the two-photon absorption response of quadrupolar organic molecules", *J. Chem. Phys.*, Vol. 116, 3646 (2002).
- [23] T. Kogej, D. Beljonne, F. Meyers, J. W. Perry, S. R. Marder and J. L. Bredas, "Mechanisms for enhancement of two-photon absorption in donor-acceptor conjugated chromophores", *Chem. Phys. Lett.*, Vol. 298, 1 (1998).

- 
- [24] P. R. Monson and W. M. McClain, "Polarization dependence of the two-photon absorption of tumbling molecules with application to liquid 1-chloronaphthalene and benzene", *J. Chem. Phys.*, Vol. 53, 29 (1970).
- [25] P. Pacher, "Two-photon absorption in organic molecules", *Diploma Thesis*, Graz University of Technology (2003).
- [26] R. W. Boyd, *Nonlinear Optics*, Academic Press, San Diego, 154 (1992).
- [27] B. M. Pierce, in *Molecular and Biomolecular Electronics*, R. R. Birge, Ed., American Chemical Society, Washington D.C., 207-269 (1998).
- [28] S. P. Karna and A. T. Yeates, in *Nonlinear Optical Materials: Theory and Modeling*, S. P. Karna and A. T. Yeates, Eds., American Chemical Society, Washington D.C., 1-22 (1996).
- [29] J. L. Bredas, in *Organic Materials for Photonics*, G. Zerbi, Ed., Elsevier Science Publishers, 127-153 (1993).
- [30] S. Mukamel, H. X. Wang, "Nonlinear optical-response of conjugated polymers – electron-hole anharmonic-oscillator picture", *Phys. Rev. Lett.*, Vol. 69, 65 (1992); A. Takahashi, S. Mukamel, "Anharmonic-oscillator modeling of nonlinear susceptibilities and its application to conjugated polymers", *J. Chem. Phys.*, Vol. 100, 2366 (1994); M. Cha, "Third-order nonlinear optical spectroscopy of organic materials", *PhD Dissertation*, University of Central Florida (1994).
- [31] J. A. Armstrong, N. Bloembergen, J. Ducuing, and P. S. Perhan, "Interactions between light waves in a nonlinear dielectric", *Phys. Rev.*, Vol. 127, 1918 (1962); P. K. Franken and J. F. Ward, "Optical harmonics and nonlinear phenomena", *Rev. Mod. Phys.*, Vol. 35, 23 (1963).

- 
- [32] B. J. Orr and J. F. Ward, "Perturbation theory of the non-linear optical polarization of an isolated system", *Mol. Phys.*, Vol. 20, 513 (1971).
- [33] W. L. Peticolas, "Multiphoton spectroscopy", *Ann. Rev. Phys. Chem.*, Vol. 18, 233 (1967).
- [34] S. Mazumdar, D. Duo and S. N. Dixit, "A four-level 'essential states' model of third order optical nonlinearity in  $\pi$ -conjugated polymers", *Synth. Met.*, Vol. 55, 3881 (1993); S. Mazumdar and F. Guo, "Observation of three resonances in the third harmonic generation spectrum of conjugated polymers: evidence for the four-level essential states model", *J. Chem. Phys.*, Vol. 100, 1665 (1994).
- [35] C. W. Dirk, L. Cheng, M. G. Kuzyk, "A simplified three-level model describing the molecular third-order nonlinear optical susceptibility", *Int. J. Quan. Chem.*, Vol. 43, 27 (1992).
- [36] R. R. Birge and B. M. Pierce, "A theoretical analysis of the two-photon properties of linear polyenes and the visual chromophores", *J. Chem. Phys.*, Vol. 70, 165 (1979).
- [37] M. Rumi, J. E. Ehrlich, A. A. Heikal, J. W. Perry, S. Barlow, Z. Hu, D. McCord-Maughon, T. C. Parker, H. Roedel, S. Thayumanavan, S. R. Marder, D. Beljonne, J.-L. Bredas, "Structure-Property Relationships for Two-Photon Absorbing Chromophores: Bis-Donor Diphenylpolyene and Bis(styryl)benzene Derivatives", *J. Am. Chem. Soc.*, Vol. 122, 9500, (2000).
- [38] E. Zojer, D. Beljonne, P. Pacher, and J. L. Bredas, "Two-photon absorption in quadrupolar  $\pi$ -conjugated molecules: Influence of the nature of the conjugated bridge and the donor-acceptor separation", *Chemistry: A European Journal*, In Print (2004).

- 
- [39] P. Cronstand, Y. Luo, H. Agren, "Generalized few-state models for two-photon absorption of conjugated molecules", *Chem. Phys. Lett.*, Vol. 352, 262 (2002).
- [40] K. D. Belfield, M. V. Bondar, O. V. Przhonska, K. J. Schafer, W. Mourad, "Spectral properties of several fluorene derivatives with potential as two-photon fluorescent dyes", *J. Luminescence*, Vol. 97, 141 (2002).
- [41] K. D. Belfield, M. V. Bondar, O. V. Przhonska, and K. J. Schafer, "Steady-state spectroscopic and fluorescence lifetime measurements of new two-photon absorbing fluorene derivatives", *J. Fluorescence*, Vol. 12, 449 (2002).
- [42] R. R. Birge, in *Ultrasensitive Laser Spectroscopy*, D. S. Kliger, Ed., Academic Press, New York, 109-174 (1983); R. S. Mulliken, "Intensities of electronic transitions in molecular spectra. I. Introduction", *J. Chem. Phys.*, Vol. 7, 14 (1939).
- [43] J. R. Lakowicz, *Principles of Fluorescence Microscopy*, Kluwer Academic, New York (1999).
- [44] M. Fischer, J. Georges, "Fluorescence quantum yield of rhodamine 6G in ethanol as a function of concentration using thermal lens spectrometry", *Chem. Phys. Lett.*, Vol. 260, 115 (1996).
- [45] K. D. Belfield, S. Andrasik, K. J. Schafer, O. Yavuz, J. M. Hales and E. W. Van Stryland, "Maleic anhydride-modified polymers for two-photon upconverted fluorescence", *Polym. Prepr.*, Vol. 84, 732 (2001).
- [46] M. C. Yappert, J. D. Ingle Jr., "Correction of Polychromatic Luminescence Signals for Inner Filter Effects", *Appl. Spec.*, Vol. 43, 759 (1989).



- 
- [47] S. M. Kennedy, F. E. Lytle, “p-Bis(o-methylstyryl)benzene as a power-squared sensor for two-photon absorption measurements between 537 and 694 nm”, *Analyt. Chem.*, Vol. 58, 2643 (1986).
- [48] R. R. Alfano, *The Supercontinuum Laser Source*, Springer-Verlag, New York (1989).
- [49] R. L. Fork, C. V. Shank, C. Hirlimann, R. Yen, W. J. Tomlinson, “Femtosecond white-light continuum pulses”, *Opt. Lett.*, Vol. 8, 1 (1983).
- [50] A. Brodeur, F. A. Ilkov, S. L. Chin, “Beam filamentation and the white light continuum divergence”, *Opt. Comm.*, Vol. 129, 193 (1996).
- [51] N. P. Ernsting, M. Kaschke, “A reliable pump-probe, broadband spectrometer for subpicosecond transient absorption”, *Rev. Sci. Instrum.*, Vol. 62, 600 (1991).
- [52] V. I. Klimov, D. W. McBranch, “Femtosecond high-sensitivity, chirp-free transient absorption spectroscopy using kHz lasers”, *Opt. Lett.*, Vol. 23, 277 (1998).
- [53] S. Yamaguchi, H. Hamaguchi, “Convenient method of measuring the chirp structure of femtosecond white-light continuum pulses”, *Appl. Spectroscopy*, Vol. 49, 1513 (1995).
- [54] R. A. Negres, J. M. Hales, A. Kobaykov, D. J. Hagan, E. W. Van Stryland, “Two-Photon spectroscopy and analysis using a white-light continuum probe”, *Opt. Lett.*, Vol. 27, 270 (2002).
- [55] R. A. Negres, J. M. Hales, A. Kobaykov, D. J. Hagan and E. W. Van Stryland, “Experiment and analysis of two-photon absorption spectroscopy using a white-light continuum probe”, *IEEE J. Quan. Elec.*, Vol. 38, 1205 (2002).
- [56] R. A. Negres, “Ultrafast nonlinear spectrometer for materials characterization”, *PhD Dissertation*, University of Central Florida (2001).

- 
- [57] P. B. Corkum, C. Rolland, T. Srinivasan-Rao, "Supercontinuum generation in gases", *Phys. Rev. Lett.*, Vol. 57, 2268 (1986); P. B. Corkum, C. Rolland, "Femtosecond continua produced in gases", *IEEE J. Quan. Elec.*, Vol. 25, 2634 (1989).
- [58] A. Brodeur, S. L. Chin, "Bandgap dependence of the ultrafast white-light continuum", *Phys. Rev. Lett.*, Vol. 80, 4406 (1998).
- [59] N. P. Ernsting, S. A. Kovalenko, T. Senyushkina, J. Saam, and V. Farztdinov, "Wave-packet-assisted decomposition of femtosecond transient ultraviolet-visible absorption spectra: application to excited-state intramolecular proton transfer in solution", *J. Phys. Chem.*, Vol. 105, 3443 (2001).
- [60] M. Lorenc, M. Ziolk, R. Naskrecki, J. Karolczak, J. Kubicki, A. Maciejewski, "Artifacts in femtosecond transient absorption spectroscopy", *Appl. Phys. B.*, Vol. 74, 19 (2002).
- [61] K. Ekvall, P. V. D. Meulen, C. Dhollande, L.E. Berg, S. Pommeret, R. Naskrecki, J.C. Mialocq, "Cross phase modulation artifact in liquid phase transient absorption spectroscopy", *J. Appl. Phys.*, Vol. 87, 2340 (2000).
- [62] Mansoor Sheik-Bahae, Ali A. Said, Tai-Huei Wei, David J. Hagan, E. W. Van Stryland, "Sensitive measurement of optical nonlinearities using a single beam", *IEEE J. Quan. Elec.*, Vol. 26, 760 (1990).
- [63] E. W. Van Stryland and M. Sheik-Bahae, in *Characterization Techniques and Tabulations for Organic Nonlinear Optical Materials*, Mark Kuzyk and Carl Dirk, Eds., Marcel Dekker, New York, 655-692 (1998).
- [64] M. J. S. Dewar, E. G. Zoebisch, E. F. Healy and J. J. P. Steward, "Development and use of quantum mechanical molecular models. 76. AM1: a new general purpose quantum mechanical molecular model", *J. Am. Chem. Soc.*, Vol. 107, 3902 (1985).

- 
- [65] J. A. Pople, D. L. Beveridge and P. A. Dobosh, "Approximate self-consistent molecular-orbital theory. V. Intermediate neglect of differential overlap", *J. Chem. Phys.*, Vol. 47, 20026 (1967); J. Ridley and M. Zerner, "Intermediate neglect of differential overlap (INDO) technique for spectroscopy. Pyrrole and the azines", *Theoret. Chim. Acta*, Vol. 32, 111 (1973).
- [66] R. J. Buenker and S. D. Peyerimhoff, "Individualized configuration selection in CI calculations with subsequent energy extrapolation", *Theoret. Chim. Acta*, Vol. 35, 33 (1974).
- [67] N. Mataga and K. Nishimoto, "Electronic structure and spectra of nitrogen heterocycles", *Z. Phys. Chem.*, Vol. 13, 140 (1957).
- [68] K. Ohno, "The Pariser-Parr-Pople method", *Theor. Chem. Acta*, Vol. 2, 219 (1964); G. Klopman, "A semiempirical treatment of molecular structures. II. Molecular terms and application to diatomic molecules", *J. Am. Chem. Soc.*, Vol. 86, 4550 (1964).
- [69] K. D. Belfield, M. V. Bondar, O. V. Przhonska, K. J. Schafer, "One- and two-photon photostability of 9,9-didecyl-2,7-bis(N,N-diphenylamino)fluorene", *Photochem. & Photobio. Sci.*, Vol. 3, 128 (2004).
- [70] A. R. Morales, "Synthesis and characterization of new fluorene derivatives for emerging electro-optic applications", *PhD Dissertation*, Benemerita Universidad Autonoma de Puebla (2004).
- [71] K. D. Belfield, K. J. Schafer, W. Mourad, and B. A. Reinhardt, "Synthesis of new two-photon absorbing fluorene derivatives via Cu-mediated Ullmann condensations", *J. Org. Chem.*, Vol. 65, 4475 (2000).

- 
- [72] K. D. Belfield, A. R. Morales, B.-S. Kang, J. M. Hales, D. J. Hagan, E. W. Van Stryland, V. M. Chapela, and J. Percino, "Synthesis, characterization and optical properties of new two-photon absorbing fluorene derivatives", *Chem. Mat.*, Submitted (2004).
- [73] K. D. Belfield, S. Yao, A. R. Morales, J. M. Hales, D. J. Hagan, E. W. Van Stryland, V. M. Chapela, and J. Percino, "Synthesis and characterization of novel rigid two-photon absorbing polymers", *Poly. Adv. Tech.*, Submitted (2003).
- [74] K. D. Belfield, A. R. Morales, S. A. Andrasik, K. J. Schafer, O. Yavuz, V. M. Chapela, J. Percino, in *Functional Condensation Polymers*, C. E. Carraher, G. G. Swift, Eds., Kluwer, London, Chap. 11 (2002).
- [75] K. D. Belfield, D. J. Hagan, E. W. Van Stryland, K. J. Schafer, R. A. Negres, "New two-photon absorbing fluorene derivatives: synthesis and nonlinear optical characterization", *Org. Lett.*, Vol. 1, 1575 (1999).
- [76] K. D. Belfield, S. Yao, "Synthesis of two-photon absorbing branched chromophores through direct tribromomethylation of fluorene", *Angewandte Chemie*, Submitted (2004).
- [77] K. D. Belfield, M. V. Bondar, A. R. Morales, O. Yavuz, O. V. Przhonska, "A new blue light-emitting oligofluorene glass: Synthesis, characterization and photophysical properties", *J. Phys. Org. Chem.*, Vol. 16, 194 (2003).
- [78] K. D. Belfield, A. R. Morales, J. M. Hales, D. J. Hagan, E. W. Van Stryland, V. M. Chapela, and J. Percino, "Linear and two-photon photophysical properties of a series of symmetrical diphenylaminofluorenes", *Chem. Mat.*, Submitted (2003).
- [79] Unpublished results.

- 
- [80] K. D. Belfield, M. V. Bondar, J. M. Hales, A. R. Morales, O. V. Przhonska, K. J. Schafer, D. J. Hagan, and E. W. Van Stryland, "One- and two-photon fluorescence anisotropy of fluorene derivatives", *J. Phys. Chem.*, Submitted, (2004).
- [81] B. E. Kohler, "A simple model for linear polyene electronic structure", *J. Chem. Phys.*, Vol. 93, 5838 (1990).
- [82] J. D. Bhawalkar, G. S. He, C.-K. Park, C. F. Zhao, G. Ruland and P. N. Prasad, "Efficient, two-photon pumped green upconverted cavity lasing in a new dye", *Opt. Comm.*, Vol. 124, 33 (1996); G. S. He, L. Yuan, N. Cheng, J. D. Bhawalkar, P. N. Prasad, L. L. Brott, S. J. Clarson and B. A. Reinhardt, "Nonlinear optical properties of a new chromophore", *J. Opt. Soc. Am. B*, Vol. 14, 1079 (1997); A. Abboto, L. Beverina, R. Bozio, S. Bradamante, C. Ferrante, G. A. Pagani and R. Signorini, "Push-pull organic chromophores for frequency-upconverted lasing", *Adv. Mat.*, Vol. 12, 1963 (2000); R. Zaleśny, W. Bartowiak, S. Styrz and J. Leszczynski, "Solvent effects on conformationally induced enhancement of the two-photon absorption cross section of a pyridinium-N-phenolate betaine dye. A quantum chemical study", *J. Phys. Chem. A*, Vol. 106, 4032 (2002); H. Lei, Z. L. Huang, H. Z. Wang, X. J. Tang, L. Z. Wu, G. Y. Zhou, D. Wang, Y. B. Tian, "Two-photon absorption spectra of new organic compounds", *Chem. Phys. Lett.*, Vol. 352, 240 (2002).
- [83] S. R. Marder, C. B. Gorman, F. Meyers, J. W. Perry, G. Bourhill, J. L. Bredas, B. M. Pierce, "A unified description of linear and nonlinear polarization in organic polymethine dyes", *Science*, Vol. 265, 632 (1994).
- [84] J. L. Oudar, "Optical nonlinearities of conjugated molecules. Stilbene derivatives and highly polar aromatic compounds", *J. Chem. Phys.*, Vol. 67, 446 (1977).

- 
- [85] A. F. Garito, J. R. Heflin, K. Y. Wong, O. Zamani-Kharmiri, in *Organic Materials for Non-linear Optics: Royal Society of Chemistry Special Publication*, No. 69, R. A. Hann and D. Bloor, Eds., Royal Society of Chemistry, London, 16-27 (1989).
- [86] L. G. S. Brooker, R. J. Sprague, "Color and constitution. IV. The absorption of Phenol Blue", *J. Am. Chem. Soc.*, Vol. 63, 3214 (1941).
- [87] S. R. Marder, C. B. Gorman, B. G. Tiemann, L.-T. Cheng, "Stronger acceptors can diminish nonlinear response in simple donor-acceptor polyenes", *J. Am. Chem. Soc.*, Vol. 115, 3006 (1993).
- [88] F. Meyers, S. R. Marder, B. M. Pierce, J. L. Bredas, "Electric field modulated nonlinear optical properties of donor-acceptor polyenes: Sum-Over-States investigation of the relationship between molecular polarizabilities and bond length alternation", *J. Am. Chem. Soc.*, Vol. 116, 10703 (1994).
- [89] S. R. Marder, D. N. Beratan, L.-T. Cheng, "Approaches for optimizing the first electronic hyperpolarizability of conjugated organic molecules", *Science*, Vol. 252, 103 (1991); S. R. Marder, J. W. Perry, G. Bourhill, C. B. Gorman, B. G. Tiemann, K. Mansour, "Relation between bond-length alternation and second electronic hyperpolarizability of conjugated organic molecules", *Science*, Vol. 261, 186 (1993); G. Bourhill, J. L. Bredas, L.-T. Cheng, S. R. Marder, F. Meyers, J. W. Perry, B. G. Tiemann, "Experimental demonstration of the dependences of the first hyperpolarizability of donor-acceptor-substituted polyenes on the ground-state polarization and bond length alternation", *J. Am. Chem. Soc.*, Vol. 116, 2619 (1994), S. R. Marder, W. E Torruellas, M. Blanchard-Desce, V. Ricci, G. I. Stegeman, S. Gilmour, J. L. Bredas, J. Li, G. U. Bublitz, S. G. Boxer, "Large molecular third-order optical nonlinearities in polarized carotenoids", *Science*, Vol. 276, 1233 (1997).

- 
- [90] I. D. L. Albert, T. J. Marks, M. A. Ratner, "Rational design of molecules with large hyperpolarizabilities. Electric field, solvent polarity, and bond length alternation effects on merocyanine dye linear and nonlinear optical properties", *J. Phys. Chem.*, Vol. 100, 9714 (1996).
- [91] Y. Luo, P. Norman, P. Macak, and H. Agren, "Solvent-induced two-photon absorption of a push-pull molecules", *J. Phys. Chem.*, Vol. 104, 4718 (2000).
- [92] M. Albota, D. Beljonne, J. L. Bredas, J. E. Ehrlich, J. Y. Fu, A. A. Heikal, S. E. Hess, T. Kogej, M. D. Levin, S. R. Marder, D. McCord-Maughon, J. W. Perry, H. Rockel, M. Rumi, G. Subramaniam, W. W. Webb, X. L. Wu, C. Xu, "Design of organic molecules with large two-photon absorption cross sections", *Science*, Vol. 281, 1653 (1998); O. Mongin, L. Porrès, L. Moreaux, J. Mertz and M. Blanchard-Desce, "Synthesis and photophysical properties of new conjugated fluorophores designed for two-photon-excited fluorescence", *Org. Lett.*, Vol. 4, 719 (2002); P. Cronstrand, Y. Luo and H. Ågren, "Generalized few-state models for two-photon absorption of conjugated molecules", *Chem. Phys. Lett.*, Vol. 352, 262 (2002); B. Strehmel, A. M. Sarker and H. Detert, "The influence of sigma and pi acceptors on two-photon absorption and solvatochromism of dipolar and quadrupolar unsaturated organic compounds", *Chem. Phys. Chem.*, Vol. 4, 249 (2003)
- [93] H. Kuhn, "A quantum-mechanical theory of light absorption of organic dyes and similar compounds", *J. Chem. Phys.*, Vol. 17, 1198 (1949).
- [94] S. J. K. Pond, M. Rumi, M. D. Levin, T. C. Parker, D. Beljonne, M. W. Day, J. L. Bredas, S. R. Marder, J. W. Perry, "One- and two-photon spectroscopy of donor-acceptor-donor distyrylbenzene derivatives: effect of cyano substitution and distortion from planarity", *J. Phys. Chem.*, Vol. 106, 11470 (2002).

- 
- [95] M. Zhao, M. Samoc, P. N. Prasad, B. A. Reinhardt, M. R. Unroe, M. Prazak, R. C. Evers, J. J. Kane, C. Jariwala, M. Sinsky, "Studies of third-order nonlinearities of model compounds containing benothiazole, benzimidazole, and benzoxazole units", *Chem. Mat.*, Vol. 2, 670 (1990).
- [96] M. G. Kuzyk, "Fundamental limits on two-photon absorption cross sections", *J. Chem. Phys.*, Vol. 119, 8327 (2003).
- [97] J. P. Hermann, J. Ducuing, "Third-order polarizabilities of long-chain molecules", *J. Appl. Phys.*, Vol. 45, 5100 (1974).
- [98] R. R. Tykwinski, U. Gubler, R. E. Martin, F. Diederich, C. Bosshard, P. Gunter, "Structure-property relationships in third-order nonlinear optical chromophores", *J. Phys. Chem.*, Vol. 102, 4451 (1998).
- [99] H. M. McConnell, "Intramolecular charge transfer in aromatic free radicals", *J. Chem. Phys.*, Vol. 35, 508 (1961).
- [100] U. Gubler, C. Bosshard, P. Gunter, M. Y. Balakina, J. Cornil, J. L. Bredas, R. E. Martin, F. Diederich, "Scaling law for second-order hyperpolarizability in poly(triacetylene) molecular wires", *Opt. Lett.*, Vol. 24, 1599 (1999).
- [101] W.-H. Lee, M. Cho, S.-J. Jeon, B. R. Cho, "Two-photon absorption and second hyperpolarizability of the linear quadrupolar molecule", *J. Phys. Chem.*, Vol. 104, 11033 (2000).
- [102] C. Puccetti, M. Blanchard-Desce, I. Ledoux, J.-M. Lehn, J. Zyss, "Chain-length dependence of the third-order polarizability of disubstituted polyenes. Effects of end groups and conjugation length", *J. Phys. Chem.*, Vol. 97, 9385 (1993).



- 
- [103] P. Najechalski, Y. Morel, O. Stephan, P. Baldeck, "Two-photon absorption spectrum of poly(fluorene)", *Chem. Phys. Lett.*, Vol. 343, 44 (2001).
- [104] O. Mongin, J. Brunel, L. Porres, M. Blanchard-Desce, "Synthesis and two-photon absorption of triphenylbenzene-cored dendritic chromophores", *Tetr. Lett.*, Vol. 44, 2813 (2003).
- [105] P. Macak, Y. Luo, P. Norman, H. Agren, "Electronic and vibronic contributions to two-photon absorption of molecules with multi-branched structures", *J. Chem. Phys.*, Vol. 113, 7055 (2000).
- [106] S. K. Pati, T. J. Marks and M. A. Ratner, "Conformationally tuned large two-photon absorption cross sections in simple molecular chromophores", *J. Am. Chem. Soc.*, Vol. 123, 7287 (2001).
- [107] M. Drobizhev, A. Karotki, M. Kruk and A. Rebane, "Resonance enhancement of two-photon absorption in porphyrins", *Chem. Phys. Lett.*, Vol. 355, 175 (2002).
- [108] K. Kamada, K. Ohta, I. Yoichiro and K. Kondo, "Two-photon absorption properties of symmetric substituted diacetylene: drastic enhancement of the cross section near the one-photon absorption peak", *Chem. Phys. Lett.*, Vol. 372, 386 (2003).
- [109] J. M. Hales, D. J. Hagan, E. W. Van Stryland, K. J. Schafer, A. M. Morales, K. D. Belfield, P. Pacher, O. Kwon, J. L. Bredas, "Resonant enhancement of two-photon absorption in substituted fluorene molecules", *J. Chem. Phys.*, Submitted (2004).
- [110] B. E. Scharf, Y. B. Band, "Enhanced two-photon transitions in molecules with permanent dipole moments", *Chem. Phys. Lett.*, Vol. 144, 165 (1988).

- 
- [111] R. Baltramiejunas, V. Gavryushin, G. Raciukaitis and V. Kubertavicius, “Deep local levels as virtual intermediate states of the two-photon absorption process in zinc oxide and zinc selenide”, *Fizika Tverdogo Tela*, Vol. 30, 1089 (1988).
- [112] B. Dick, R. M. Hochstrasser, H. P. Trommsdorff, in *Nonlinear Optical Properties of Organic Molecules and Crystals*, Vol. 2, D. S. Chemla and J. Zyss, Eds., Academic Press, Orlando, 169-170 (1987).
- [113] R. L. Sutherland, *Handbook of Nonlinear Optics*, Marcel Dekker, New York (1996).